Development of Mg-RE alloys for medical applications

Doctoral thesis
(Dissertation)

to be awarded the degree of
Doctor of Engineering (Dr. -Ing.)

submitted by

Lei Yang

from Liaoning / VR China

approved by the Faculty of Natural and Materials Science,

Clausthal University of Technology

Date of oral examination

04. 04. 2013

Chairperson of the Board of Examiners

Prof. Dr. B. Tonn

Chief Reviewer

apl. Prof. Dr. R. Schmid-Fetzer

Reviewer

Prof. Dr. K. U. Kainer

Name, Vorname
Yang, Lei

Datum:
13.05.2013

EIDESSTATTLICHE ERKLÄRUNG

Hiermit erkläre ich an Eides Statt, dass ich die bei der Fakultät für Natur- und Materialwissenschaften der Technischen Universität Clausthal eingereichte Dissertation selbständig und ohne unerlaubte Hilfe verfasst und die benutzten Hilfsmittel vollständig angegeben habe.

Unterschrift

Name, Vorname
Yang, Lei

Datum:
13. 05. 2013

EIDESSTATTLICHE ERKLÄRUNG

Hiermit erkläre ich an Eides Statt, dass die eingereichte Dissertation weder in Teilen noch in Ihrer Gesamtheit einer anderen Hochschule zur Begutachtung vorliegt oder vorgelegen hat und dass ich bisher noch keinen Promotionsversuch unternommen habe.

Unterschrift

Acknowledgement

This thesis work would not have been finished without the contribution of the following people that I would like to acknowledge.

I sincerely want to thank my supervisor Prof. Dr. K.U. Kainer for his patience, guidance and support during my research work. My special thanks go to Prof. Rainer Schmid-Fetzer for his agreement to be the chief reviewer of this work and his valuable suggestions to complete this study.

My deep gratitude also goes to Dr. Norbert Hort, Dr. Frank Feyerabend, Dr. Yuanding Huang and Prof. Regine Willumeit for their enlightening guidance and fruitful discussions during this work.

Many thanks also to Dr. Carsten Blawert, Dr. Daniel Hoeche, Mr. Daniel Laipple, Dr. Jan Bohlen, Dr. Amirthalingam Srinivasan, Dr. Qiuming Peng and Dr. Chamini Mendis for their help in experiments and helpful discussions.

Many thanks to Gabriele Salamon, Willi Punessen, Günter Meister, Gert Wiese, and Sabine Schubert for their excellent technical help, and to all the staffs of WZP and WPS groups for their assistance, warmth and the friendly atmosphere they provided me during my stay.

Finally, I would like to thank my family for their encouragement and support, especially my wife, Xiuli Zhai.

Abstract

A number of recent researches have emphasised the possibilities of Mg alloys as a new class of degradable biomaterials for orthopaedic applications. The major drawback for many Mg alloys to be used as an implant material is that they do not undergo a controlled corrosion in physiological environment and maintain the mechanical integrity over a given length of time. Therefore, it is extremely important to develop novel Mg alloys with a combination of good mechanical properties, slow corrosion rate, uniform corrosion mode and acceptable biocompatibility. Mg-RE (RE = rare earth) alloys have a good combination of mechanical and corrosion properties and a wide investigation has been performed on RE-containing Mg alloys for medical applications, such as Mg-4Y-3RE (WE43) alloy [1, 2]. However, the previously developed Mg-RE alloys are for structure applications and they are not completely suitable for medical applications. To develop new Mg-RE alloys for medical applications, Dy and Gd are used as the main alloying elements in this work, as they are the best tolerated RE based on in vitro study [3].

Binary Mg-xDy (x=5, 10, 15, 20 wt.%) alloys and Mg-10wt.% RE-0.2Zr (RE=Dy+Gd) alloys are prepared by permanent mould direct chill casting method. Solution treatment and ageing treatment are carried out to optimize their microstructure and properties. Microstructure is investigated using X-ray diffraction (XRD), optical microscope (OM), scanning electron microscope (SEM) and transmission electron microscope (TEM); mechanical properties are tested in tension and compression; bio-corrosion behaviour is studied using weight loss method in cell culture medium; corrosion layer is examined carefully using OM, SEM, XRD and X-ray induced photoelectron spectroscopy (XPS), and its cytotoxicity is evaluated primarily using cell adhesion (SEM observation) and live/dead staining methods (fluorescence microscopy).

For binary Mg-Dy alloys, the results show that the microstructure is inhomogeneous and the grain size is coarse. The yield strength increases while the ductility decreases with the increased Dy content. Mg-10Dy alloy has the best combination of yield strength and ductility. However, its mechanical properties require further improvement. Mg-10Dy alloy shows low corrosion rate and uniform corrosion morphology after immersion in cell culture medium. The enrichment of Dy was

detected in the corrosion layer but it induced no cytotoxicity for osteoblasts. Therefore, Mg-10Dy alloy is considered to be the best candidate for further alloy development.

To further improve the mechanical properties of Mg-10Dy alloy and maintain the good corrosion properties, Mg-10wt.% RE-0.2Zr (RE=Dy+Gd) alloys are developed. The results show that corrosion morphology of all Mg-10wt.% RE-0.2Zr alloys is uniform. Their corrosion rate is similar (around 0.5 mm/y) in T4 and T6 condition, which is a little bit lower than that of Mg-10Dy alloy. The mechanical properties can be tailored. The tensile yield strength (TYS) can be varied between 99.8 and 211.6 MPa, and the compressive yield strength (CYS) can be varied between 96 and 241.2 MPa. The highest ultimate tensile strength (UTS) achieved is 353.9 MPa and the highest ultimate compressive strength (UCS) reaches to 423 MPa. The elongation to fraction is at a minimum value of around 7.8%, while it reaches to a maximum value at 24.1%. No cytotoxicity is observed from the primary test on osteoblasts.

For different applications depending on the mechanical properties needed, different alloy compositions and heat treatment technique can be selected. For an example, cardiovascular stents need very good ductility but high mechanical properties are not important. Thus, the Mg-10Dy-0.2Zr alloy, with a TYS of 104.6 MPa and elongation of 24.1% in T4 condition, can be used. Load bearing bone plates and screws need very high mechanical properties but need not have a very good ductility. Thus, the Mg-5Dy-5Gd-0.2Zr alloy, with the TYS of 188.3 MPa and elongation of 11.8% in T6 condition, can be used.

List of symbols and abbreviations

Ar	Argon gas
ASTM	American Society for Testing and Materials
AZ31	Mg-3Al-1Zn (wt.%)
AZ91	Mg-9Al-1Zn (wt.%)
LAE442	Mg-4Li-4Al-2RE (wt.%)
BrdU	Bromodeoxyuridine
BSE	Back scattered electrons
CCM	Cell culture medium
CO_2	Carbon Dioxide
CR	Corrosion rate
CYS	Compressive yield strength
DMEM	Dulbecco’s modified eagle medium
E	Young’s modulus
EDX	Energy dispersive X-rays spectroscopy
HA	Hydroxyapatite
HEPES	2-(4-(2-hydroxyethyl)-1-piperazinyl) ethanesulfonic acid
hcp	hexagonal close packed
LD50	Half lethal dose
LM	Light microscopy
MTT	(3-(4,5-dimethyl-2-thiazolyl)-2,5-diphenyl-2H-tetrazolium 72 bromide)
MagIC	Magnesium Innovation Centre
PBS	Phosphate buffered solution
m-SBF	Modified simulated body fluid
HBSS	Hank’s balanced salt solution
RE	Rare earth metals
SBF	Simulated body fluid
SEM	Scanning electron microscopy
t	exposure time in hours
T4	Solution treatment
T6	Ageing treatment
TEM	Transmission electron microscopy
TYS	Tensile yield strength
UTS	Ultimate tensile strength

V	Volt
XPS	X-ray induced photoelectron spectroscopy
XRD	X-Ray diffraction
W	weight loss of specimen in mg
WE43	Mg-4Y-3RE (wt.%)
XTT	(2,3-bis-(2-methoxy-4-nitro-5-sulfophenyl)-2H-tetrazolium-5-carboxanilide)

Table of contents

1 Introduction

There are four major types of materials used as load-bearing biomaterials: metals, ceramics, polymers and their composites [4]. Metallic materials continue to play an essential role as biomaterials in assisting with the repair or replacement of diseased or damaged bone tissue [5]. Metals are more suitable for load-bearing applications than ceramics or polymers due to the combination of high mechanical strength and fracture toughness. Thus, metals including stainless steels (316L), titanium alloys (Ti6Al4V) and cobalt-chromium-based alloys have found wide applications as biomaterials [6]. Current metallic biomaterials are essentially neutral in vivo, and remain as permanent fixtures. In case of plates, screws and pins used to secure serious fractures, the implants need to be removed by a second surgery after the tissue has healed sufficiently. Repeat surgery not only increases cost to the health care system, but also further morbidity to the patient [6]. Another limitation of current metallic biomaterials is the release of toxic metallic ions and/or particles through corrosion or wear processes, which is considered potentially harmful to the tissues of the human body [7-12].

An alternative to the above-mentioned materials is biocompatible and resorbable implants. Polymers were the first materials to be used in such materials commercially. However, polymers are limited by their low mechanical properties, which restricts their applications in load-bearing and tissue supporting applications, as the size of implant with sufficient mechanical properties may not satisfy the space requirement [6]. Recently, biodegradable metals have become one of the most revolutionary research topics in biomaterials field. Promising biodegradable metals are Mg-based and Fe-based metallic alloys [13]. Mg and its alloys are widely used as structure materials in lightweight applications in the transportation industry, due to their low weight, high specific strength and good machinability. These advantages and biodegradability of Mg based alloys have attracted wide interest as degradable biomaterials.

Mg and its alloys have a comparable Young’s modulus and a favourable compression and tensile strength in relation to the cortical bone compared with Ti alloys and stainless steels [14]. No secondary surgery would be necessary as Mg implant will be resorbable and disposed by the body [6]. Thus, the strain for the patient as well as the treatment expenses could be reduced significantly. Additionally, the adult human body contains about 30 g of Mg, most of which exists in muscle and bone. The homeostasis of Mg in human body can be maintained by the kidneys and intestine [6].

Mg and its alloys have been investigated as degradable implants since the end of the 19th century [15]. Most of the investigations found that Mg degraded too quickly to be used as implant [15]. With the improvement of casting technology of Mg in recent years, the corrosion rate of Mg and its alloys is largely reduced. Recent investigations with the Mg alloys Mg-3Al-1Zn (AZ31), Mg-9Al-1Zn (AZ91), WE43 and Mg-4Li-4Al-2RE (LAE442) showed all these alloys have a good biocompatibility *in vivo*. LAE442 alloy showed the least gas generation, followed by WE43 [1]. In addition to animal studies, the resorbable Mg-based stents (made of WE43 alloy) have been investigated in clinical cases. The clinical trials indicate it is necessary to modify the stent characteristics to prolong degradation time [16]. These alloys were intended for structure applications and not as medical implants. Some of the alloying elements contained in them are potentially harmful to human body such as Al. Therefore, the development of novel Mg alloys for medical applications is essential.

2 Literature review

2.1 Advantages of Mg and its alloys as implants

The commercial available metallic implants (titanium, CoCr, and stainless steel) for temporary use have disadvantages such as requirement of secondary surgery and release of toxic metal ions. In comparison, Mg and its alloys are more suited as a temporary biomaterial as they are biodegradable, biocompatible and have close mechanical properties to bone [6].

2.1.1 Degradable

Mg and its alloys are generally known to degrade in aqueous environments via an electro chemical reaction (corrosion), producing Mg hydroxide and hydrogen gas. The overall reaction of Mg in aqueous environments is:

$Mg + 2H_2O \rightarrow Mg(OH)_2 + H_2\uparrow$ Equation 1

In an environment enriched with chloride ions, Mg hydroxide converts into highly soluble Mg chloride [14]. Thus, Mg can degrade in the human body where chloride ions are abundant. Fig. 1 shows the remains of Mg alloys in bones of guinea pig after 18 weeks. The different degradation for different alloys can be seen clearly. The AZ91 alloy showed almost complete degradation while LAE442 alloy only showed minimal degradation.

Fig. 1: Three-dimensional reconstruction of remaining Mg alloy (red) segmented from the bone matrix (gray) by voxel growing method. (a) AZ91D, (b) LAE442; Bar =1.5 mm [2].

In general, an ideal biodegradable implant should be able to compromise its mechanical integrity during implantation with the recovering of tissues. The ideal compromise between mechanical integrity and degradation of a biodegradable stent is illustrated in Fig. 2. The degradation begins at a very slow rate to maintain optimal mechanical integrity of the stent during the arterial vessel remodelling process. The implant degrades with time and its strength diminishes gradually, while the tissue is regenerated or recovered. A period of 6–12 months is expected for the remodelling process to be completed. While the mechanical integrity decreases, the degradation progresses at a sufficient rate without causing an intolerable accumulation of degradation product around the implantation site. A total period of 12–24 months after implantation is considered to be a reasonable time for the complete degradation of the implant.

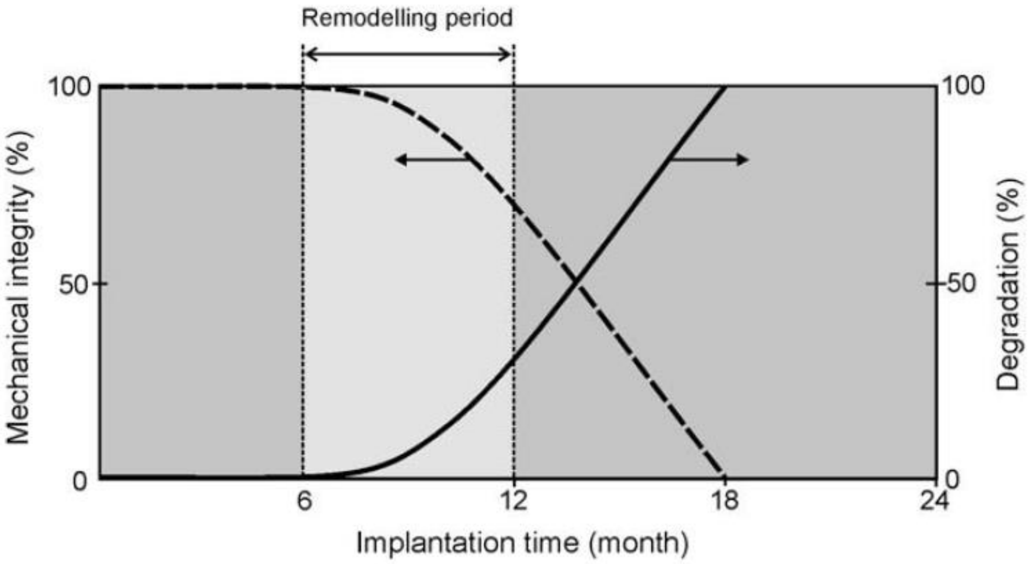

Fig. 2: Illustration of an ideal compromise between mechanical integrity and degradation of a biodegradable stent [13].

2.1.2 Good biocompatibility

Mg is abundant in the human body and an adult body contains about 30 g Mg, which exists mainly in muscles and bones [17]. The U.S. Food and Nutrition Board has recently re-established the recommended dietary allowance of Mg for adult males to be 420 mg/day and for adult females to be 320 mg/day, respectively [4]. Dietary Mg deficiency has been shown to be a factor for osteoporosis [18]. Mg is a co-factor in many enzymes, and it can stabilize the structures of DNA and RNA [19]. Therefore, the Mg corrosion product is likely to be physiologically beneficial rather than harmful. The level of Mg in the extracellular fluid ranges from 0.7 to 1.05 mmol/l, where homeostasis is maintained by the kidneys and intestine [6]. Serum Mg levels exceeding 1.05 mmol/l can lead to muscular paralysis, hypotension and respiratory distress [17]. Cardiac arrest occurs for severely high serum levels of 6–7 mmol/l, but the incidence of hyper-Mg is rare due to the efficient excretion of the element in the urine [17, 20]. Due to its functional roles in the bone tissue, Mg has stimulatory effects on the growth of new bone tissue [21-24]. Witte et al. [1] studied the bone response to Mg alloys compared with a degradable polymer (PLA96). The results indicated that the bone mass surrounding the Mg rods was enhanced compared with the polymer control group, Fig. 3.

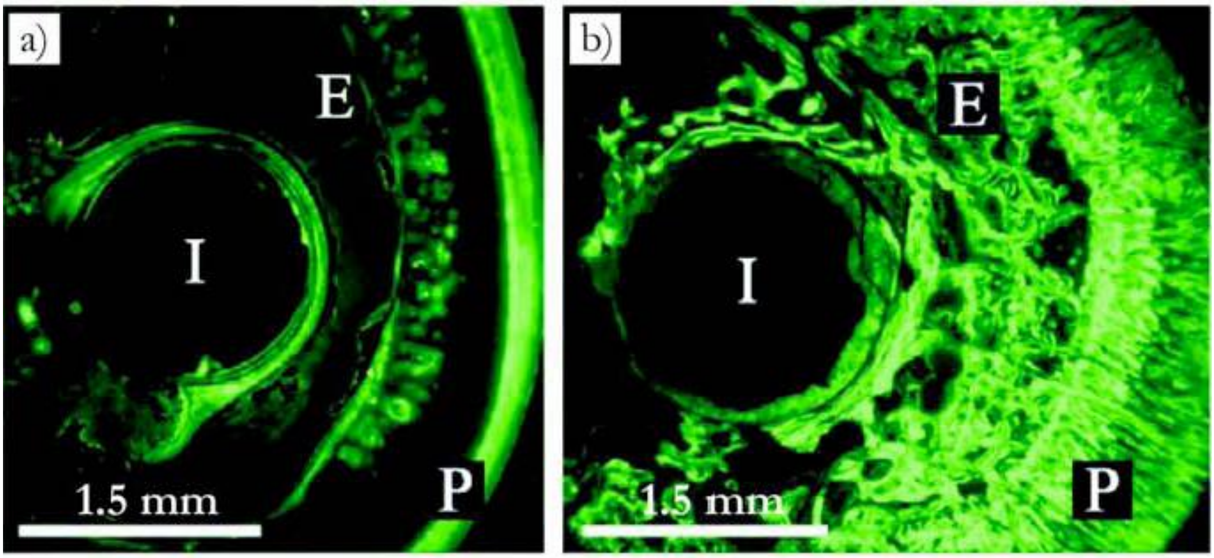

Fig. 3: Fluoroscopic images of cross-sections of a degradable polymer (a) and a Mg rod (b) performed 10mm below the trochanter major in a guinea pig femur. Both specimens were harvested 18 weeks postoperatively. *In vivo* staining of newly formed bone was done by calcein green. Bar=1.5mm; I=implant residual; P=periosteal bone formation; E = endosteal bone formation [1].

2.1.3 Young’s modulus and mechanical properties

The Young’s modulus of current metallic biomaterials is not well matched with that of the natural bone tissue. This can result in stress shielding effects and reduce stimulation of new bone growth and remodelling, which decreases implant stability [25]. The specific density of Mg and its alloys is approximately 1.7-2.0 g/cm^3, which is very similar to that of human cortical bone (1.75 g/cm^3) [4]. The Young’s modulus of Mg alloy is about 40–45 GPa, which is much close to that of human bone (5–23 GPa) compared with other metallic materials [14]. Thus the Mg alloys implants may minimize stress-shielding. The compressive yield strength of Mg is also close to that of natural bone compared with the other commonly used metallic implants [6].

Table 1 summarizes the mechanical properties of experimental Mg alloys, traditional biomaterials and some human tissues. Mg alloys have much closer Young's modulus to the cortical bone than the traditional Ti6Al4V alloy, better ductility than the synthetic HA, and higher strength than DL-PLA. The tensile strength and elongation of Mg alloys varies and may be turned to suit for different medical applications.

Table 1: Mechanical properties of different normal tissues and implant materials [14]. The range of values depends on composition, heat treatment and processing conditions.

Tissue/material	Compression strength (MPa)	Tensile strength (MPa)	E-mod. Tensile (GPa)	Density (g/cm^3)	Yield strength (MPa)	Elongation to fracture (%)
Cortical bone	164-240	35-283	5-23	1.8-2.0	---	1.07-2.1
Cancellous bone	---	1.5-38	0.01-1.6	1.0-1.4	---	---
Arterial wall	---	0.5-1.72	1	---	---	---
Titanium TiAl6V4)	---	830-1172	114	4.43	760-1103	10-15
Stainless steel	---	480-620	193	8	170-310	30-40
Synthetic HA	100-900	40-200	70-120	3.05-3.15	---	---
Bioactive glasses	---	40-60	35	---	---	---
DL-PLA	---	29-35	1.9-2.4	---	---	5-6
Mg alloys	90-350	140-460	40-45	1.7-1.9	40-430	2-25

2.2 Historical use of Mg as biomaterials and problems

Biodegradable Mg implants have a very long history, starting shortly after the discovery of Mg element in 1808. In 1878, a Mg wire ligature was successfully used to stop bleeding vessels in three occasions: once in a radial artery and twice in the operation for varicocele [15]. In 1900, Payr investigated tubular and thin-walled Mg cylinders as connectors for vessel anastomosis, using pig and dog animal models to study Mg vessel connectors [15]. Payr stated that only the intra-vascularly placed Mg tubes exhibited thrombotic blood clotting at the end of the tubes, which, however, never closed the remaining lumen; no thrombosis was observed with extra-vascularly placed Mg tubes [15]. Payr also successfully treated an extensive haemangioma cavernosum at the chin of a 14 year old girl with Mg arrows [15].

In 1906, Lambotte used Mg implants in a 17 year old child who had suffered from a complicated pseudarthrosis with severe malalignment of the distal third of the lower leg due to a 2 month old fracture of the lower leg [15]. He used an iron wire cerclage at the fibula and a Mg plate with six steel screws at the tibia to stabilize the fracture. The implant failed due to the electrochemical reaction between the Mg plate and the steel screws. After some animal experiments, Mg alloy was used to treat supracondylar fractures of children, as these fractures heal quickly. Lambotte and Verbrugge operated on 4 children (7–10 year old) in total with supracondylar humerus fractures, and all healed without complications (except the gas cavities). Good to total restoration of the joint function was observed and with no pain in the operated area. The gas cavities disappeared after several weeks and were not a major concern in clinical cases. Lambotte also used a Mg plate and screw fixation to treat humerus fracture for a child. Three weeks after the operation the metal plate had dissolved almost completely and the fracture line was no longer visible [15].

In 1944, 34 cases where Mg-Cd alloy was fashioned into plates and screws and used to secure various fractures has been reported [6]. Of the 34 cases, 9 were unsuccessful. These failures were attributed to infection, or difficulties arising with the mounting of a plaster cast, which presumably did not allow for treatment of gas cysts. In all patients, no increase in serum levels of Mg and distinct inflammatory reactions to the implant was observed. The material is reported to have stimulated the development of a hard callous at the fracture site. Hydrogen gas was given off during degradation of the implant while was easily treated by drawing off the gas with a subcutaneous needle. While the sizes of the implants used were not given, it was reported that the mechanical integrity of most implants were maintained for 6–8 weeks, with complete resorption occurring in 10–12 months. It was also reported that some implants only survived 3–5 weeks, and was attributed to increased acidity in the fracture environment. Similar results were reported by Znamenski in 1945, where Mg alloy containing 10 wt.% aluminum was used to treat gunshot wounds in two young men [6]. In both cases, fractures fused in 6 weeks, with the Mg plate no longer detectable after 6 weeks, and the pins no longer detected after 4 weeks [6].

These early examples show that Mg-based materials are non-toxic and may actually stimulate bone tissue healing. However, the degradation rate of pure Mg or simple alloys is too rapid to allow sufficient time for healing. It is desirable to have the implanted fixture to have mechanical integrity for at least 12 weeks [6]. In spite of some early successes with Mg-based implants, it is likely that Mg was abandoned due to the fast degradation rate and production of gas during the *in vivo* corrosion when the stainless steels became available [6].

2.3 Corrosion of Mg and its alloys

2.3.1 Techniques to measure corrosion rate

Generally, three methods are often used to measure the corrosion rate of Mg, which are electrochemical tests, weight loss and hydrogen evolution experiments. The corrosion rate of Mg evaluated from electrochemical test has pertained to conditions soon after specimen immersion and the corrosion rates measured are not steady state corrosion. Thus, to measure the corrosion rate in Mg alloys, the later two techniques are usually employed [26]. In the weight loss experiments, the degradation rates of the specimens are calculated using:

$$CR = \frac{8.76 \times 10^4 \times \Delta \mathrm{g}}{\mathrm{A} \cdot t \cdot \rho} \qquad \text{Equation 2}$$

Where CR refers to the corrosion rate in mm/year, Δg is the weight change in the sample in g, ρ is density of the alloy in $g \cdot cm^{-3}$, A is the exposure area in cm^2, and t represents the exposure time in h. Corrosion products are usually removed by immersion in chromic acid (200 g/l CrO_3) for around 20 min, which react with the corrosion products, but does not damage the Mg substrate.

A schematic illustration of the apparatus to measure the volume of hydrogen evolved during the experiments is illustrated in Fig. 4 [26]. The amount of dissolved Mg can be calculated from the volume of hydrogen generated from the reaction. This simple and inexpensive method has some limitations due to atmospheric pressure changes and possible hydrogen leakages from the experimental set-up [26].The stoichiometry of the redox equation which produces elemental hydrogen is not fully understood and thus the hydrogen gas volume can not be directly correlated to the production of Mg ions [27]. In addition to the methods mentioned above, microtomography (especially synchrotron-based microtomography) as a non-destructive method was introduced to obtain general corrosion rates by measuring the time-dependant change in the metallic volume of the remaining implant. This method was also applied to estimate corrosion rates from explanted samples [14].

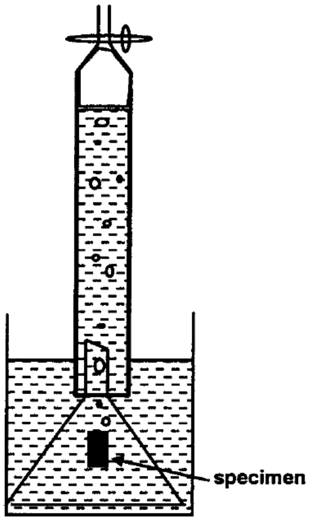

Fig. 4: Schematic illustration of the procedure to measure the corrosion rate by measuring the volume of hydrogen evolved [26].

2.3.2 Influence of impurities on corrosion

Corrosion of Mg is the extremely sensitive to impurities, such as Fe, Cu, and Ni. The amount of impurities depends on the alloy's composition and processing techniques. The corrosion rate is low when the amount of impurities is below a tolerance limit, but it increases substantially when the amount of impurities are higher than the tolerance limit. For instance, when iron content is higher than the tolerance limit in commercial pure Mg, the corrosion rate increases dramatically as shown in Fig. 5 [28].

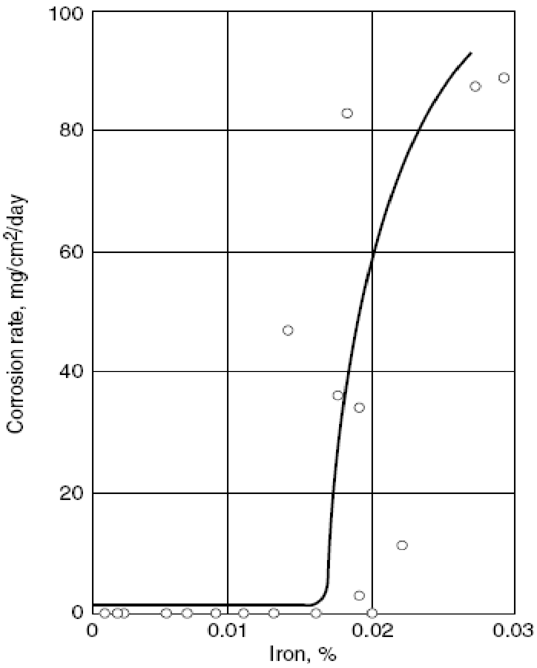

Fig. 5: effect of iron content on the corrosion rate of commercially pure Mg subjected to immersion in 3 % NaCl [28].

There are two hypotheses for the change in corrosion rate beyond tolerance limits of Fe, Ni, Cu and Co: (i) phase precipitation and (ii) surface deposition [29]. The phase precipitation hypothesis is that, above the tolerance limit, a second phase (rich in Fe, Ni, Cu or Co) is precipitated inside the Mg alloy and then this phase supports the cathodic reaction (hydrogen evolution) much more effectively than α-Mg does. The surface deposition hypothesis believe that there is deposition of metallic Fe, Ni, Cu or Co, by means of a reaction such as $Mg + Fe^{2+} = Fe + Mg^{2+}$, on the Mg alloy surface. And there is a sufficient concentration of ions of Fe^{2+}, Ni^{2+}, Cu^{2+} or Co^{2+} in the solution next to the surface of the Mg alloy because of the dissolution of impurity in the Mg. This surface deposition hypothesis is thus based on the ideas that (i) the probability of depositing surface metallic-impurity cathodes increases with impurity content and (ii) these surface metallic-impurity cathodes dominate the corrosion behaviour above a critical surface density. Both the phase precipitation and surface deposition hypotheses assume that effective hydrogen cathodes are produced above the tolerance limit and both assume that these cathodes have a composition rich in the impurity element. The essential difference is that the phase precipitation hypothesis relates to the precipitation of a second phase inside the Mg alloy whereas the surface deposition hypothesis relates to the deposition of cathodes on the Mg alloy surface. To date there has been no successful resolution regarding which hypothesis is more reasonable [29].

For biomedical applications, the amount of impurities has to be strictly controlled. Although for some elements, such as Fe, the impurity concentrations are lower than the physiological range in the body, a small amount of Fe can increase the corrosion rate dramatically. Elements such as Be should be avoided, which is highly toxic [14]. In general, the amount of impurities should be kept minimal to retain a low corrosion rate and good biocompatibility of Mg alloys.

2.3.3 Influence of second phases on corrosion

The standard corrosion potential of Mg is very low (-2.37 V). Mg is more active than all the engineering alloys, and consequently corrodes preferentially in any galvanic couple. Thus controlling galvanic corrosion is very important and attention needs to be paid to reducing galvanic corrosion in any application using Mg alloys [30]. Second phases have a pronounced effect on the corrosion of Mg alloys as the second phases can form a galvanic corrosion couple with Mg matrix. Fig. 6

schematically illustrates the galvanic corrosion in Mg-Al alloys between the $Mg_{17}Al_{12}$ β-phase and the matrix α-phase. The matrix α phase is typically anodic to the β phase and is preferentially corroded. The β phases are undermined due to the dissolution of α-Mg matrix. Both the primary and eutectic α can form a galvanic corrosion cell with the β phase, accelerating the corrosion rate. For example, AZ91 alloy has an appreciable amount of β phase ($Mg_{17}Al_{12}$) along the dendritic grain boundaries, which acts as cathodic site with respect to the matrix. One opinion is that $Mg_{17}Al_{12}$ is inert in chloride solutions compared with the surrounding Mg matrix and acts as a corrosion barrier if these $Mg_{17}Al_{12}$ phases form a continuous network [30]. However there was also a view that formation of $Mg_{17}Al_{12}$ is detrimental for the corrosion of Mg. The absence of the $Mg_{17}Al_{12}$ could enhance the corrosion resistance of the Al-rich Mg base alloys by eliminating the micro-galvanic effects. The Mg–Al based alloys were reported to corrode predominantly by galvanic reaction between the Mg matrix and $Mg_{17}Al_{12}$ phase [30]. The AZ91 Mg alloy has a large tendency towards pitting corrosion when exposed to simulated body fluid (SBF) and 0.9 wt.% NaCl solution. The formation of a micro-galvanic couple between the Mg matrix and $Mg_{17}Al_{12}$ phase leads to selective corrosion at the boundaries between the $Mg_{17}Al_{12}$ phase and Mg matrix [30].

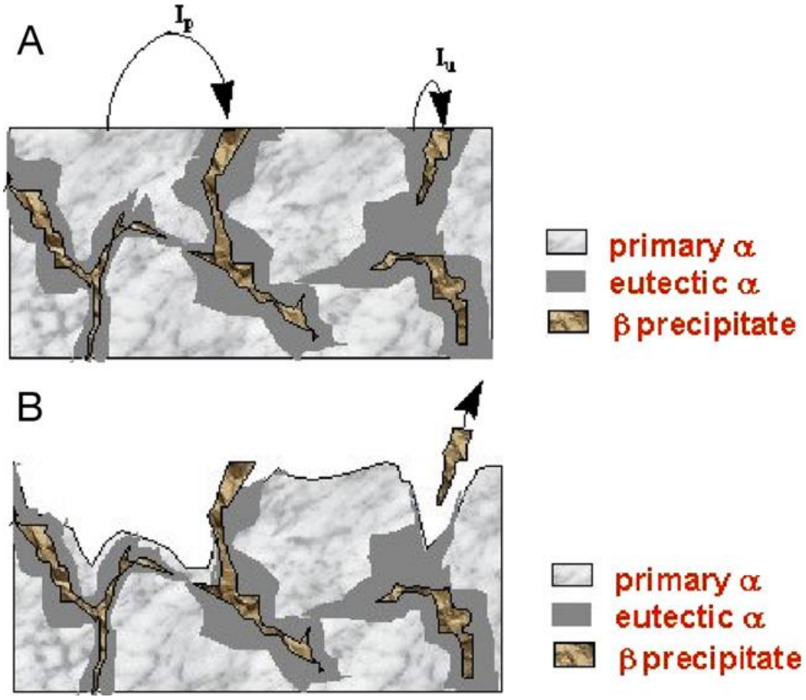

Fig. 6: Schematic representation of the galvanic corrosion for Mg-Al alloys between the $Mg_{17}Al_{12}$ β-phase and the matrix α-phase [30].

2.3.4 Influence of electrolyte and environment on corrosion

The choice of electrolyte has significant influence on the corrosion rate and corrosion mechanism of Mg. As listed in Table 2, various simulated physiological fluids such as 0.9 wt.% NaCl solution, simulated body fluid (SBF), phosphate buffer solution (PBS), and Dulbecco's modified eagle medium (DMEM) are commonly used [31-34]. Under the same conditions, the degradation rate of AZ91 alloy in different solutions varies significantly. The average degradation rate in SBF can be one order of magnitude higher than that in Hanks' solution [33]. This large difference stems mainly from the different compositions of the solutions.

Table 2: Compositions of commonly used in vitro electrolyte [35].

	0.9% NaCl	PBS	Hanks'	SBF	DMEM
Na^+ (mmol/L)	153	157	142	142	127.3
K^+ (mmol/L)		4.1	5.9	5.0	5.3
Ca^{2+} (mmol/L)		---	1.3	2.5	1.8
Mg^{2+} (mmol/L)		---	0.8	1.5	0.8
HCO_3^- (mmol/L)		---	4.2	4.2	44.1
Cl^- (mmol/L)	153	140	145	147	90.8
HPO_4^{2-} (mmol/L)		11.5	0.8	1	0.9
SO_4^{2-} (mmol/L)		---	0.8	0.5	0.8
Tris (g/L)		---	---	6.07	---
Protein (g/L)		---	---	---	---
Amino acids (g/L)		---	---	---	1.6
Glucose (mmol/L)		---	1	---	4.5
Hepes (g/L)		---	---	---	5.96

The physiological environment contains various aggressive components that can attack Mg alloys. Table 3 and Table 4 list the main inorganic and organic contents in the body plasma. The highest content is Cl^-, which aggressively attacks the implants. The hydrocarbonates are the most important buffers in body fluid. Xin et al. [36] studied the effects of these aggressive inorganic ions on the degradation behaviour of AZ91 alloy. The high concentration of chloride ions can transform the $Mg(OH)_2$ into more soluble $MgCl_2$. The breakdown of $Mg(OH)_2$ decreases the protection against corrosion, consequently promoting further dissolution of the substrate. Song and

Atrens [26] also suspect that chloride ions are involved in the intermediate step of Mg dissolution by accelerating the electrochemical reaction from Mg to Mg univalent ions.

Although the concentration of HPO_4^{2-} is quite low in the physiological environment, it effectively slows down the dissolution of Mg by forming compact and insoluble phosphate layer [36]. Unlike $Mg(OH)_2$, these phosphate layer can not be destroyed by chloride ions. The concentration of HCO_3^- is much higher than that of HPO_4^{2-}, and consumption of OH^- by HCO_3^- can drastically increase the degradation rate of Mg. A high concentration of HCO_3^- induces fast passivation on the surface due to quick formation of insoluble carbonates. A high concentration of HCO_3^- at the corrosion sites contributes to the formation of insoluble carbonates, and consequently corrosion at these sites is suppressed. Passivation can effectively retard the pitting corrosion in AZ91. SO_4^{2-} also attacks Mg, but it is not as severe as the chloride ions.

Table 3 Inorganic concentrations in body plasma (mmol/l) [35].

Inorganic ions	Na^+	K^+	Mg^{2+}	Ca^{2+}	HCO_3^-	Cl^-	HPO_4^{3-}	SO_4^{2-}
Concentration	142.0	5.0	2.5	1.5	27.0	103.0	1.0	0.5

Table 4 Concentrations of the main organic components in body plasma [35].

Organic components	Protein	Amino acids	Glucose
Concentration	63-80 g/l	Unknown	3.6-5.2 m mol/l

In addition to the inorganic ions, the organic components also play important role in determining the corrosion behaviour of Mg alloys. A number of studies investigated the corrosion of Mg alloys with different corrosion media with and without proteins [31, 37-40]. The compositions of the corrosive medium influenced the Mg corrosion behaviour, which is altered by the presence or absence of proteins. Proteins such as albumin are demonstrated to form a layer on the Mg alloys in *in vitro* experiments, which retard the corrosion [31, 38, 40]. Fig. 7 shows the hydrogen evolution volumes of Mg1.5Ca alloy as a function of immersion time in 0.9 wt.% NaCl solutions with different amount of proteins [41]. It is obvious that the corrosion rate is dramatically reduced with 1 g/l protein addition, which is slightly further reduced when the addition of protein increases to 10 g/l.

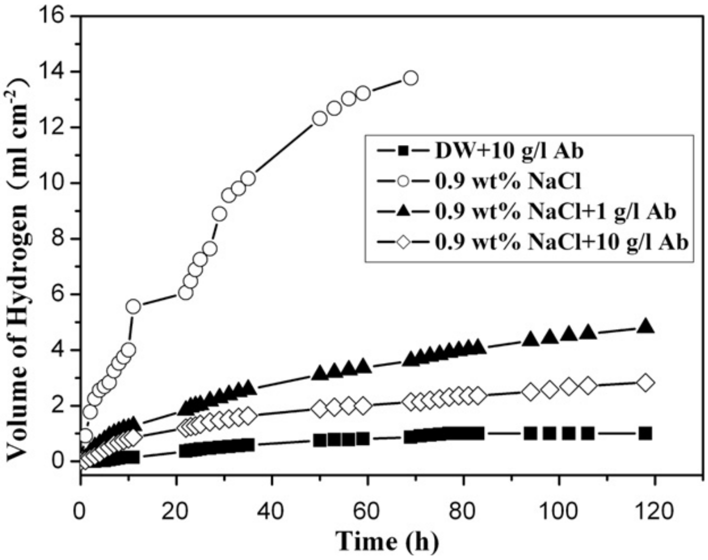

Fig. 7: Hydrogen evolution volumes of Mg-1.5Ca alloy as a function of immersion time in different electrolytes [41].

In measuring the degradation rate, it is important to consider the ratio of electrolyte volume to sample surface area, as this ratio may dramatically change the pH value in the vicinity of the samples. The degradation rate of a Mg-Zn-Mn alloy with a 6.7 (ml/cm) volume to surface ratio is 2 times higher than that of a sample with a ratio 0.67. However, there is no obvious variation when this ratio increases from 6.7 to 67 [32]. It is well known that the constant mass transportation process and continuous exchange of body fluids take place in the physiological environment. In order to mimic the circulation process in the human body, it is essential to design *in vitro* tests incorporating circulation and refreshment of electrolytes. Such a pseudo-physiological system was developed and has been used to evaluate the degradation of biomedical Mg alloys [42].

At present, it is difficult to compare the degradation rates of Mg alloys reported from different publications. One of the main reasons is the use of different electrolytes and different surface area/electrolyte volume ratios. It is important to standardize the test for more accurate and reliable evaluation of degradation rates, and also make it possible to compare the data from different sources [31, 35].

2.3.5 Corrosion products

Corrosion of Mg-based implants produces four reactants: a large amount of OH^-; a corrosion layer on the implant; dissolved Mg ions and other alloying elements; and hydrogen gas. Due to the strong buffering ability in the biological environment, a large amount of OH^- can be consumed and pH would not change abruptly. In general the release of OH^- is not a problem [35].

Viscosity, tissue components and structures like lipids, proteins and glycosaminoglycans influence the hydrogen diffusion coefficient in the body [43]. The diffusion coefficient of hydrogen increases exponentially with the increase in water fraction of tissues [44]. Thus, the local blood flow and the water content of the tissues surrounding the implant are the most important parameters in controlling the removal of H_2 from the implant site. They should be considered in designing biodegradable Mg alloys with an appropriate corrosion rate. Consequently, local hydrogen cavities would occur, if more hydrogen is produced than can be dissolved in the surrounding tissue. This means that Mg alloys have to have an appropriate corrosion rate *in vivo* in case of the formation of hydrogen cavities [14].

The dissolved Mg goes into either the body fluids or corrosion layer on the sample. *In vivo* study shows that the corrosion layer is composed of C, O, P, Mg, Ca and the alloying elements used [45, 46]. For *in vitro* investigations, the constituents in this corrosion layer vary with the solution type, corrosion environment as well as the alloy composition. In 0.9 wt.% NaCl solution, $Mg(OH)_2$ and MgO are the main constituents in the surface layer [26]. In solutions such as SBF, DMEM and Hanks' solution with HCO_3^- and HPO_4^{3-} ions, the insoluble phosphates and carbonates are usually present in the corrosion layer in addition to MgO and/or $Mg(OH)_2$ [32, 38, 47]. Due to the amorphous nature of these components, it is difficult to identify the exact nature of the corrosion layer [26, 47, 48]. However, some investigations have shown crystalline phosphates and carbonates in corrosion layer [32, 38, 48]. In PBS solution, the main corrosion products are Mg phosphates and $Mg(OH)_2$. The insoluble carbonates found on samples are possibly formed by reacting with the dissolved CO_2. Alloying elements may also be incorporated into the corrosion products [33, 49]. Aluminium oxide and hydroxide were identified the corrosion layer of AZ91 samples after exposure in m-SBF [47]. Furthermore, carbonates are one of the main components in the corrosion products, when the corrosion test is carried out under cell culture condition with 5 % CO_2 [38]. *In vitro* investigations in DMEM solution under cell culture conditions are close to *in vivo* conditions, but this still needs further improvement.

2.4 Evaluation of cytotoxicity

Evaluation of the biocompatibility is generally performed in two ways, namely by direct contact and indirect evaluation using extracted test solution. In direct contact experiments, cells are seeded on the samples directly and the initial surface states play a critical role in the establishment of cell–surface bonding. One of the problems using this method is the changes in the materials surface at the early stage. Rapid dissolution accompanied with evolution of hydrogen bubbles leads to a very dynamic surface. This can dramatically hinder cell attachment creating major difficulty in carrying out cell culture experiments. Thus, the control of the surface reaction is important for initial cell reaction [50]. For spreading and long-term survival of cells, surface chemistry and morphology are key factors [35].

The indirect immersion experiments are often performed. The samples are first exposed to a suitable solution for various durations and then the solution is extracted and used for cell cultures. The advised guide line for biomaterial testing is the European standard ISO 10993 [51]. Some limitations exist for the use of this standard for testing biodegradable or corroding biomaterials. One major obstacle is the preparation of extracts from Mg alloys. The extracted solution, regardless of which alloy is used, shows a high osmolarity and pH value and hence exposes the cells to an osmotic shock [52]. This result in the death of cells and classify all Mg alloys as cytotoxic by definition. For Mg research, it is reported that data produced by testing methods *in vitro* are not well correlated with *in vivo* data [2]. Therefore, a new *in vitro* test standard needs to be established for testing Mg alloys.

To investigate the cytotoxicity of biomedical Mg alloys, although tetrazolium salt-based assays, such as MTT (3-(4,5-dimethyl-2-thiazolyl)-2,5-diphenyl-2H-tetrazolium 72 bromide) and XTT (2,3-bis(2-methoxy-4-nitro-5-sulfophenyl)-5-73 ((phenylamino)carbonyl)-2H-tetrazolium hydroxide) assays, can be used, it has to be done with caution. The dissolved Mg in the extracted media can convert the tetrazolium salts to formazan, leading to a higher background thus falsifying the results of cell viability [53]. Another test, i.e. the BrdU (Bromodeoxyuridine) assay, is found to be unaffected by Mg ions. This test is probably more appropriate for the evaluation on the cytotoxicity of Mg-based materials [53]. Current evaluations of cytotoxicity of Mg alloys are still very preliminary and more systematic evaluations are needed from both scientific and technical standpoints.

2.5 Roles of alloying elements

Alloying elements play important role in developing Mg-based biomaterials. Alongside pure Mg, the alloying elements Al, Mn, Zn, Ca, Li, Zr, Y and RE are used in developing Mg implant materials [1, 2, 34, 46, 54-60]. These elements influence both the mechanical and physical properties of Mg. As long as the alloying elements remain in solid solution, they can be used for solid solution strengthening. Furthermore, most of these alloying elements can react with Mg or with each other to form intermetallic phases. These phases contribute to enhancement of the alloy strength by precipitation strengthening. Both solid solution strengthening and precipitation strengthening improve strength, but deteriorate the ductility. Almost every alloying element contributes to grain refinement to some extent, providing grain boundary strengthening. The grain size and its distribution are affected by the preparation process and by the alloying elements. Grain boundary strengthening improves both strength and ductility [14]. Compared to the matrix, a grain boundary is a distorted area with high imperfection and high internal energy, and corrosive attack in a pure material therefore normally begins at the grain boundary first [14].

Segregation of the alloying elements towards the grain boundary occurs depending on their types and properties and the chosen solidification route. Due to the segregation, the composition in the center of the grain is different from those close to the grain boundary. This influences the corrosion behaviour. Normally the matrix close to the grain boundary is more cathodic compared to the center of the grain. Since the grain boundary is a weak area that promotes early corrosive attacks, coarse grains are preferred. However, segregations are minimized in small grained Mg alloys and the corrosion behaviour appears to be more homogeneous [14].

The mechanical properties are usually the primary consideration when developing structure materials. In biomedical engineering, factors such as biocompatibility and the rate of degradation are crucial. Good biocompatibility is essential because the materials released from the implants to the body must not be toxic. This is especially important for degradable implants. The large amount of Mg and potentially harmful alloying elements released during degradation may lead to cytotoxicity, and the degree of toxicity highly depends on the dissolution rate and alloying elements [35].

2.5.1 Al

As an alloying element, Al provides both the solid solution and precipitate strengthening. The increase of the content of Al lowers the temperature of liquidus and solidus lines and enhances the castability of Mg alloys [14].

The typical concentration of Al in serum is 2.1–4.8 µg/L [61]. A high Al concentration is harmful to neurons and osteoblasts, and may result in dementia as well as Alzheimer’s disease [62]. It causes muscle fiber damage [63] and decreases viability of osteoblast [64]. Additionally, mild foreign body reactions were observed in an *in vivo* study on Mg-Al alloy implant [65]. Hence, the amount of Al in Mg alloys must be carefully controlled.

2.5.2 Mn

Mn does not affect the mechanical properties of Mg alloys significantly, but increases the yield strength slightly. The most important role of Mn lies in improving the corrosion resistance by converting iron and other metal elements into relatively harmless intermetallic compounds [4].

Mn is an essential trace element in human body, which plays an important role in metabolic cycle of e.g. lipids, amino acids and carbohydrates [14]. It influences the immune system, bone growth, blood clotting, cellular energy regulation and neurotransmitter synthesis [14]. It is also the scavenger of free radicals in the manganese superoxide dismutase [14]. The concentration of Mn should be <0.8 µg/L in blood serum [14]. The high concentrations may induce neurotoxicity [14]. The poisonous effect of Mn from Mg alloys on cell viability and proliferation has been observed [66].

2.5.3 Zn

Zn was found to be next to aluminium in strengthening effectiveness as an alloying element in Mg [67]. Adding Zn to Mg–Mn alloys improves both the tensile strength and the corrosion successfully [56, 68]. However, adding Zn with amount more than 2 wt.% leads to an embrittlement in Mg-Al alloys [14].

Zn is a trace element in human body and its normal level in blood serum is 12.4-17.4 µmol/l. It is essential for the immune system, and a co-factor for specific enzymes in bone and cartilage. However, high concentrations of Zn could result in neurotoxicity [14].

2.5.4 Ca

Calcium contributes to the solid solution and precipitate strengthening in Mg alloys. It also acts as a grain refining agent and contributes to grain boundary strengthening [69]. Larger amounts of Ca (>1 wt.%) can lead to hot tearing or sticking [14].

Ca is the most abundant mineral in the human body (1–1.1 kg), which is mainly stored in bone and teeth. Its normal serum level reaches 0.919–0.993 mg/l. It is tightly regulated by homeostasis of skeletal, renal and intestinal mechanism [70].

2.5.5 Li

Lithium is the only element that is able to change the lattice structure of Mg from hexagonal close-packed (h.c.p.) to body-centered cubic (b.c.c.) [14]. It can be used to enhance ductility and formability of Mg alloys, but unfortunately it does not enhance the strength [14]. It has been claimed that Li can improve the corrosion resistance of a Mg-Li-Al-RE alloy. The reason is that Li shifts the pH value of the solution to a pH > 11.5, which stabilizes the $Mg(OH)_2$ film on the alloy surface. However, the *in vivo* alkalization is a hazard to the human body.

The normal blood serum level of Li is only 2-4 ng/g [14]. Li is used in compound for the treatment of psychiatric disorders [14]. Overdosage could cause problems for kidney or lung dysfunctions and possible birth defects on children [14].

2.5.6 Zr

Zirconium is an effective grain refining agent in Al-free Mg alloys and can enhance the yield strength through Hall-Petch strengthening [14].

Zr exhibits low ionic cytotoxicity in vitro [71], excellent biocompatibility in vivo [72], no evidence of mutagenicity or carcinogenicity, good resistance to corrosion, and an osteocompatibility equal to or exceeding that of Ti [73, 74].

2.5.7 RE

RE are a set of seventeen elements in the periodic table, specifically the fifteen lanthanides plus scandium and yttrium [75]. In general, the RE can be divided into two groups: the first group RE, such as Y, Gd, Tb, Dy, Ho, Er, Tm, Yb, and Lu, has large solid solubility in Mg; while the second group (Nd, La, Ce, Pr, Sm, Eu) presents only limited solid solubility in Mg [14]. They are added to Mg alloys generally through using master alloys or pure RE metal.

RE elements are used to improve the mechanical and corrosion properties of Mg alloys. Some of the RE is kept in solid solution. Its addition provides both solution and precipitation strengthening. RE with limited solubility usually forms intermetallic phases at the dendritic and grain boundaries at the early stage of solidification. The existence of these RE-containing intermetallics can effectively pin the grain boundaries at elevated temperatures, and improve the high temperature creep resistance and increases the service temperature of Mg [14]. For example, yttrium has a high solid solubility in Mg. It is often incorporated into Mg alloys together with other RE elements to enhance the creep resistance at high temperatures. Y was also reported to benefit the corrosion resistance. Various RE-doped Mg alloys such as WE43, Mg–8Y, Mg–10Gd and LAE 442 are proposed as the implant materials [1, 34, 60, 76].

Recently, Feyerabend et al. [3] investigated the influence of RE on viability of human osteosarcoma cell line MG63, human umbilical cord perivascular cells and mouse macrophages, and the induction of apoptosis along with the expression of inflammatory factors (Table 5). The effects of the analyzed rare earth elements seem to be related to their ionic radii. Except Eu, the other RE with low solid solubility included in the study (Nd, La, Ce) shows a higher influence on the cell reaction than those RE with high solid solubility. Among the RE with high solid solubility (Y, Gd and Dy), Y exhibits effects on viability of macrophages and an accompanying influence on the inflammatory reaction. The cellular reaction to Gd and Dy was comparably low, with a slight advantage for Dy.

Table 5: Summarized features of the tested rare earth elements. Positive influences (+), intermediate influences (o), negative influences (–) and significant effects (– –) on the applied test systems are indicated (n/a : no results for the apoptosis test). Elements with high solid solubility are highlighted in grey [3].

Element	Viability	Inflammatory response		Apoptosis
		TNF-α	IL-1α	
La	– –	– –	–	+
Ce	– –	+	+	o
Gd	+	o	o	–
Nd	o	–	+	o
Pr	o	–	+	o
Eu	+	+	+	o
Dy	+	+	o	n/a
Y	+	–	–	n/a

The light RE, La, Ce and Pr, are known to be hepatotoxic as they cause fatty liver [77, 78]. Pr is the most toxic element leading to animal death in comparable concentrations used for Ce, probably due to the low clearing rate [77]. All these elements were shown to induce chromosome aberrations in *in vivo* mouse studies [79]. The *in vitro* study of Palmer [80], where pulmonary macrophages were exposed to La, Ce and Nd, showed similar results: Ce was highly cytotoxic (half lethal dose (LD50): 29 µM), followed by La (LD50: 52µM), whereas Nd showed only a slight reduction of viability. Eu was well tolerated in all analyzed cells and its LD50 measured in rats *in vivo* was reached at 550 mg/kg [81]. Eu is used as a fluorescent marker designed for the cellular uptake and was tested in different cell types for this purpose without inducing major alterations [82-84].

In a study on intraperitoneal administration of $GdCl_3$, the LD50 for rats was 550 mg/kg. The oral administration did not result in acute toxicity, however, the liver of male rats was affected [85]. $GdNO_3$ induces acute toxicity at a concentration of 300 mg/kg in mice and 230 mg/kg in rats [86, 87]. The toxicity can be drastically reduced by addition of chelating agents such as Ethylene Diamine Tetraacetic Acid (EDTA). Therefore Gd chelates as contrast agent for magnetic resonance imaging (MRI) were introduced in the 1980s. In the human body, chelated rare earths are rapidly excreted via urine, while unchelated ionic rare earths easily form colloid in blood. The colloid material is taken up by phagocytic cells of the liver and spleen.

RE elements also accumulate in the bones, but it is not clear what cells of the bone take up the most rare earths. The clearance of the bone is known to be very slow, but the general potential toxicity is described to be low [88]. Excess yttrium can change the gene expression of rats and impose adverse effects on DNA transcription factors [77, 89]. Dysprosium was tolerated best in the cytotoxicity tests *in vitro* [3]. LD50 in mice for $DyCl_3$ was determined to be 585 mg/kg [90]. Dy exhibits antimicrobial effects at a concentration of 300 µM [91]. Similar to Gd, Dy is also used as contrast medium for MRI [92]. The effects of Dy and Y *in vivo* are similar [77]. With increasing doses the distribution of the elements in spleen and lungs increases, while the concentration in kidneys and blood decreases. Toxicity due to Dy in the liver was not observed [77].

2.6 Design principles of Mg alloys for medical application

Biomaterials are an interdisciplinary field that deals with the interactions between material and biological tissues. Strength is not the only property that has to be considered. Ductility, corrosion behaviour under service conditions and biocompatibility also form an important part of the property profile, which is influenced by alloy composition and processing routs.

2.6.1 Mechanical properties

The strength of biodegradable implants reduces as a function of implant time due to the degradation. Thus, there is no benchmark for the strength of biodegradable implants since their strength is highly dependent on degradation rate after implantation. Moreover, the requirements are different for different applications. For instance, high ductility is preferred for vascular stents, while it is not essential for bone screws and plates. Therefore, the priority is to control the degradation rate and tune the mechanical properties according to the implant. The strength of metallic materials is primarily governed by the resistance that they offer to the movement of dislocations. Solutes, precipitates, and grain boundaries act as obstacles and inhibit the movement of dislocations. All these factors depend on the alloying elements, processing route and the following heat treatment. Therefore, the high solubility of alloying elements is desired, which gives more flexibility for the design and following treatment.

2.6.2 Corrosion

There are a number of factors that can affect corrosion behaviour of Mg alloys, such as alloying additions, microstructure, corrosion medium, corrosion environment, induced stresses, pH and porosity. Control of corrosion rate is one of the most important aspects in the design of biodegradable Mg alloys. It is very difficult to take all the factors into account in the beginning of the designing process.

However, careful control of the composition and microstructure plays the key role in determining the corrosion behaviour. The *in vivo* degradation mechanisms of Mg are mainly galvanic corrosion, pitting corrosion, uniform corrosion or combination of these mechanisms [4]. Electrochemical potential series and Pourbaix diagrams [93] can provide information about potential of pure metals. This is very helpful in understanding the galvanic corrosion between pure metals. However, it’s not very useful in predicting the micro-galvanic corrosion in as-cast alloys, which occurs due to differences in the potential of the intermetallic phases and the matrix. There is limited data on the potential of intermetallic phases. The data available in the literature show that majority of intermetalics in Mg alloys lead to micro-galvanic corrosion [26, 34, 45, 58]. Therefore, alloying elements with high solubility are preferable, as their intermetalics can be dissolved into Mg matrix through heat treatment.

2.6.3 Biocompatibility

Biocompatibility is the priority for implant materials. For Mg-based degradable implants, the material and degradation products need to be locally and systemically non-toxic, as well as non-carcinogenic. Furthermore, inflammation of surrounding tissues should be minimal. If corrosion is too fast, localized high levels of Mg ions could potentially cause toxicity in cells in close proximity due to osmolar imbalance. Inflammation of surrounding tissues can also be induced. Interestingly, investigation of Mg-based materials has generally shown favorable results for toxicity and inflammation of the tissue [6, 15]. However, further investigation to ensure a generalized, long-term lack of systemic toxicity and lack of carcinogenicity is necessary. Also, although no increase in serum levels of Mg are reported, super-physiological levels of Mg in the blood have associated risks [6] and therefore should be monitored.

The choice of alloying elements for biocompatibility is critical, as toxicity and carcinogenicity have been reported for alloying candidates such as zinc, aluminium, chromium, and cadmium [94-96]. It is necessary to consider potential immune stimulatory reactions, for example, in the case of patient sensitization to metals (metal allergy) such as nickel, cobalt and chromium [97]. Finally, during the aqueous oxidation of Mg, hydrogen gas is generated and potential consequences must be considered for a specific application. While no intervention has been reported for some applications, others articulate the practice of drawing off subcutaneous pockets of trapped gas with a needle [6].

2.7 Currently investigated Mg alloys for medical applications

Various Mg alloys were proposed for biomedical applications. Many *in vitro* and *in vivo* experiments have been performed to study their degradation rates and mechanisms [35].

2.7.1 Mg-Al system

In the Mg-Al-Zn system, the corrosion resistance in simulated body fluids (SBF) decreases with increase in Al content [98]. Both $Mg(OH)_2$ and Al_2O_3 were observed in the corrosion layer of Al-containing Mg alloys. $Mg(OH)_2$ is slightly soluble in water and can be transformed into soluble $MgCl_2$ by chloride ions. Unlike $Mg(OH)_2$, Al_2O_3 is insoluble in water and can not be destroyed by chloride ions. Thus the addition of Al enhances the corrosion resistance of Mg alloys. Al_2O_3 can also naturally form in as-polished samples and is more stable than MgO in chloride-containing solutions, which also contributes to the enhancement of corrosion resistance. However, a high Al concentration increases the content of $Mg_{17}Al_{12}$ phase, which increases the tendency for pitting corrosion [35]. Although many studies look at the application of AZ series alloys as implants [33, 39, 98] and the *in vivo* study shows no toxicity in short term [1], Al is not suggested to be as alloying element due to its potential toxicity in the long run [14]. The current developments in Mg alloys for implants focus on the Al free Mg alloys.

2.7.2 Mg-Ca system

Li et al. [45] explored the effect of Ca on the mechanical and corrosion properties of binary Mg-xCa (x=1~3 wt.%) alloys. The ultimate tensile strength and elongation of the as-cast Mg-1Ca alloy are 71.4 MPa and 1.87 %, respectively. They are improved to 166.7 MPa and 3 % after hot rolling, and to 239 MPa and 10.6 % after hot extrusion. During the *in vivo* implantation, the pins of Mg-1 wt.% Ca alloy gradually degraded within 90 days and showed a corrosion rate of 1.27 mm/y. Erdmann et al. [99] studied the *in vivo* degradation and biomechanical properties of Mg-0.8Ca alloy screws and found that the holding power of the screws reduced largely after 6 weeks implantation. Krause et al. [100] investigated the initial mechanical strength and the degradation behaviour with the associated changes in mechanical properties of Mg-0.8Ca, LAE442 and WE43 alloys for osteosynthesis implants. It is found that Mg-0.8Ca implants showed the least initial strength and the highest loss in volume after 6 months, and concluded that its use as load bearing degradable implant material seems to be limited.

2.7.3 Mg-Zn system

Mg-6 wt.% Zn alloy exhibits the tensile strength approximately 279.5 MPa and elongation 18.8 % after solid solution treatment and hot working [101]. The rods of this alloy were implanted into the femoral shaft of rabbits, and they gradually absorbed *in vivo* at a degradation rate of 2.32 mm/y with newly formed bone surrounding the implant. The Zn content of Mg-xZn-1Mn alloys is optimized to 1 wt.% based on their mechanical and corrosion properties [56]. The extruded Mg-1Zn-1Mn alloy, with a tensile strength of 280 MPa and an elongation of 22 %, was implanted into the femora of rat. Post-operation examination after 18 weeks showed around 54% of the implant was left [102]. The Mg-Zn alloys show good potential for medical applications.

2.7.4 RE-containing system

Witte et al. [1, 2, 60] investigated the *in vivo* degradation and corrosion properties of LAE442 and WE43 alloys. The implanted rods completely degrade in 18 weeks and showed good biocompatibility. Heublein et al. [103] had reported that the degradation of AE21 alloy in coronary artery was considered to be linear and drew the conclusion that the vascular implants consisting of Mg alloys are possibly a realistic alternative to permanent implants. These results indicate that the Mg alloys containing RE (non-toxic) are one of the potential biomaterials.

The Mg-RE alloy was the only Mg-based alloy used in clinical cases recently. In the first clinical treatment reported by Peeters et al. [104], 20 patients were treated with absorbable Mg stents (3.0-mm-diameter, 15-mm-length, containing Mg>90 % and RE) for suboptimal angioplasty. The picture of the implanted stent is shown in Fig. 8. In this case, no major or minor amputation was necessary in any of the patients, yielding a limb salvage rate of 100 %. In a 6-month randomized study on 60 patients (74 lesions), the stents degraded too rapidly, resulting in the occurrence of restenosis within 6 months [13]. The Mg alloy stent was also used to sustain perfusion of a long segment recoarctation in a newborn [13]. Owing to a rapid degradation process, the stented vessel returned into its previous course and a second stent was implanted. Despite the two stents were used in the newborn, pathological Mg levels in serum were not detected [13]. A multi-centre and non-randomized prospective study was recently performed by Erbel et al. [16]. The stents achieved an immediate angiographic response similar to that of other metallic stents and they safely degrade after 4 months. However, the stents still show some limitations. The restenosis rate is higher than that of other bare metal stents such as stainless steel and titanium. Therefore the study suggested a necessary modification to the stents so that a prolonged degradation time can be achieved.

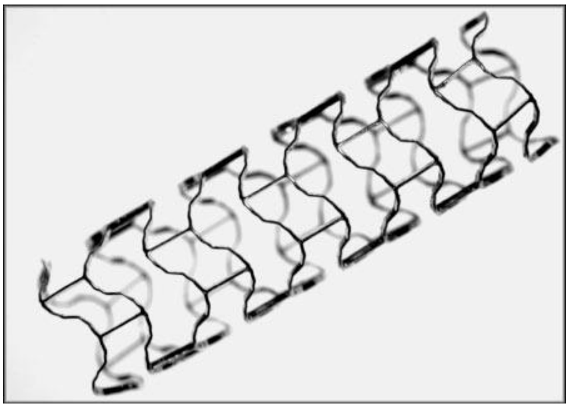

Fig. 8: Bioabsorbable Mg stent in fully developed state (BIOTRONIK, Berlin, Germany) [104].

These clinical studies further confirm the possibility of Mg alloys as implants, while indicate that there is a need for further refinements in Mg alloys.

2.8 Background of Mg-Dy and Mg-Gd based systems

A number of studies were conducted on Mg-Dy and Mg-Gd based alloys due to combination of good mechanical and corrosion properties [105-110]. These focus on their use as structure material especially at elevated temperature. There are very few investigations on these alloy systems as degradable implants. Recently, Hort et al. reported the potential of Mg-Gd alloys as biodegradable materials [34].

2.8.1 Mg-Dy based system

The Mg rich side of binary Mg-Dy phase diagram is shown in Fig. 9. The maximum solubility of Dy in Mg is very high, reaching 25.34wt.% at eutectic temperature. Rokhlin [105] reported that the mechanical properties of extruded binary Mg-(5~25wt.%)Dy alloys at 20°C and 250 °C (Table 6). The mechanical properties of Mg-Dy alloys can be adjusted widely by changing the Dy content. At room temperature, the ranges of TYS and elongation are 115-370 MPa and 1-21%, respectively. At 250 °C the elongation increases significantly, but the TYS reduces slightly. For example, the elongation of Mg-10Dy alloy is increased from 20 % to 29 %, but its TYS is only reduced from 132 MPa to 120 MPa. Therefore, these alloys are strongly suggested for the use at elevated temperature.

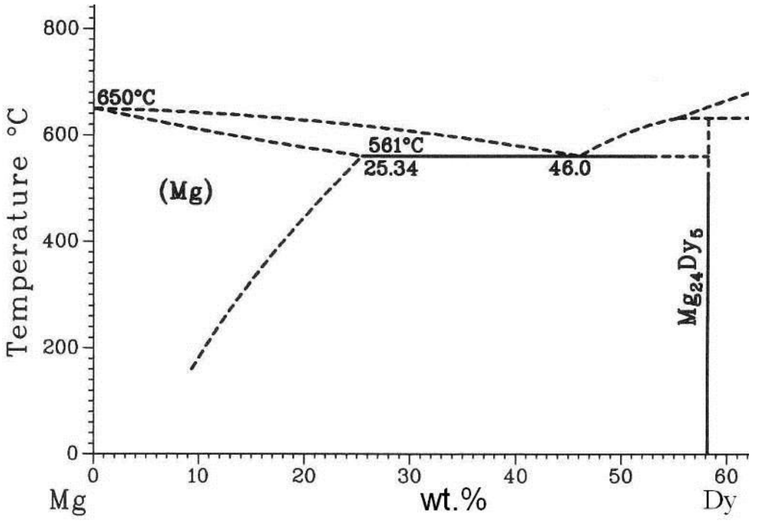

Fig. 9: Mg rich side of binary Mg-Dy phase diagram [111].

Table 6: Mechanical properties of extruded binary Mg-Dy alloys at 20 °C and 250 °C [105].

Alloys	TYS (MPa)		UTS (MPa)		Elongation (%)	
	20 °C	250 °C	20 °C	250 °C	20 °C	250 °C
Mg-5Dy	115	80	180	150	21	30
Mg-10Dy	132	120	203	180	20	29
Mg-15Dy	181	170	249	305	15	27
Mg-20Dy	330	300	393	340	3	13
Mg-25Dy	370	380	402	430	1	5

2.8.2 Mg-Gd based system

Gd is also an alloying element which can effectively improve mechanical properties of Mg alloys [112], and is much cheaper than Dy. As a result, almost all of works concentrate on the development of Mg-Gd system alloys instead of Mg-Dy system. Fig. 10 shows the Mg rich side of binary Mg-Gd phase diagram. The maximum solubility of Gd in Mg is 23.49 wt.% at eutectic temperature. Rokhlin [105] reported the mechanical properties of extruded binary Mg-(2-20wt.%)Gd alloys at 20 °C and 250 °C (Table 7). Similar results to binary Mg-Dy alloys were obtained at 20 °C. The mechanical properties are dependent on Gd content.

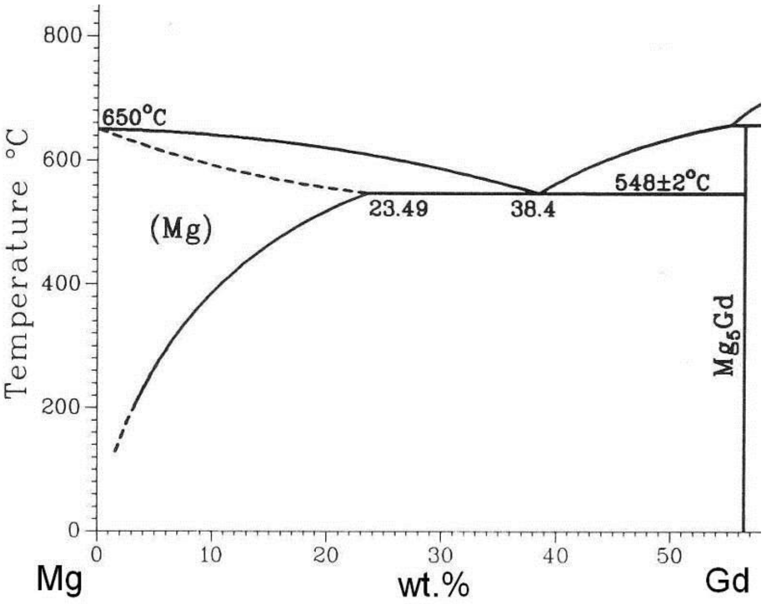

Fig. 10: Mg rich side of binary Mg-Gd phase diagram [111]

Table 7: Mechanical properties of extruded binary Mg-Gd alloys at room temperature [105].

Alloys	TYS (MPa)		UTS (MPa)		Elongation (%)	
	20 °C	250 °C	20 °C	250 °C	20 °C	250 °C
Mg-2Gd	70	40	140	90	9	35
Mg-5Gd	75	60	150	15	18	28
Mg-10Gd	170	110	230	170	12	23
Mg-15Gd	210	130	250	200	4	21
Mg-20Gd	315	220	320	280	0.2	18

Recently, Hort et al. [34] studied high purity cast Mg–2Gd, Mg–5Gd, Mg–10Gd, Mg–15Gd alloys for medical applications. The alloys were in the as-cast condition (F), solutionized 24 h at 525 °C and water quenched (T4), and solutionized and aged for 6 h at 250 °C (T6). All alloys contained the second phase Mg_5Gd at grain boundaries in the as-cast state. After T4 treatments, most of these particles dissolved although some remained. The T6 treatment led to precipitation of fine nano-sized particles in all alloys except for Mg–2Gd. TEM diffraction investigations show theses particles are the meta-stable β′ and β″. The β′ phase is homogeneously distributed throughout the matrix whereas β″ was only found in limited areas. Mechanical properties of these alloys are shown in Table 8. By adjusting the concentration of Gd and the heat treatments, tensile yield stress can be adjusted between 33 and 200 MPa, and ultimate tensile strength between 79 and 250 MPa.

Table 8: mechanical properties of binary Mg-Gd alloys at room temperature [34].

conditions	Alloys	TYS (MPa)	UTS (MPa)	Elongation (%)
F	Mg-2Gd	38	104	6.4
	Mg-5Gd	55	128	6.6
	Mg-10Gd	84	131	2.5
	Mg-15Gd	128	175	0.9
T4	Mg-2Gd	33	87	4.9
	Mg-5Gd	45	98	6.0
	Mg-10Gd	69	112	3.2
	Mg-15Gd	118	189	2.4
T6	Mg-2Gd	41	101	5.7
	Mg-5Gd	43	78	4.3
	Mg-10Gd	85	132	2.2
	Mg-15Gd	201	250	0.7

The corrosion rate of these alloys was measured by immersion in 1 % NaCl at room temperature (Fig. 11). The corrosion rate decreases with increasing Gd content up to 10 % for the alloys in all the conditions. In particular the corrosion rate for Mg-10Gd in the T4 condition was 0.7 mm/y. The corrosion rate in the T6 condition was even smaller at 0.4 mm/y despite the presence of nano-sized precipitates, which does not have an adverse influence on the corrosion rate. The corrosion rate for Mg–15Gd was much higher due to the micro-galvanic acceleration by the second phase.

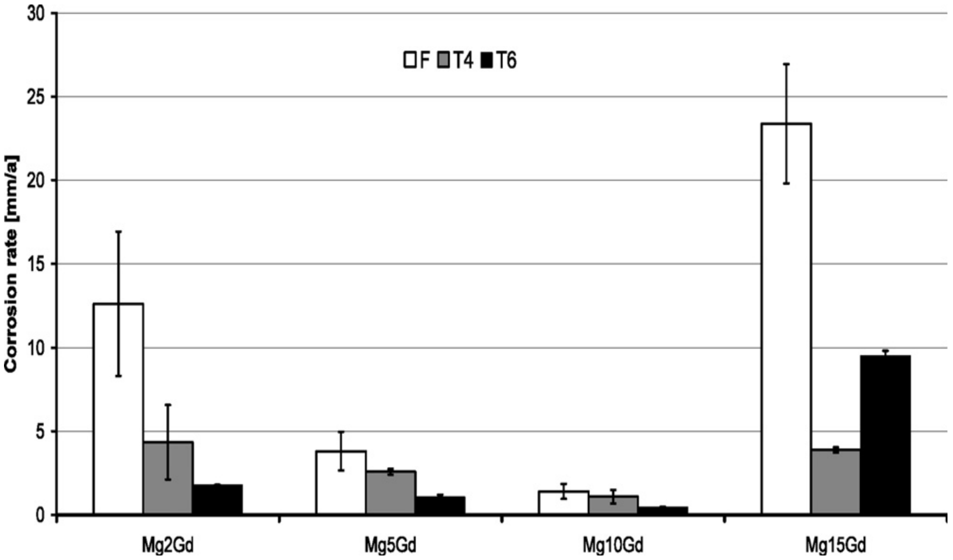

Fig. 11: Corrosion rate of binary Mg-Gd alloys in 1 wt.% NaCl solution at room temperature [113].

Since Gd is an expensive alloying element for the industrial applications, alloy concentration has to be controlled. Therefore, for the industrial applications such as car components, other alloying elements are introduced and the Gd content is generally kept below 10 wt.%. There is a large amount of research on Mg-Gd-Y alloys system [106-110], As-cast Mg-10Gd-2Y-0.5 Zr alloy in T6 condition following T4 treatment has a TYS of 239 MPa, which is further increased to 331 MPa in the extruded and T6 treated condition [108]. Liang et al. [110] investigated the corrosion property of Mg-7Gd-3Y-0.4Zr alloy in 5 wt.% NaCl solution and found a low corrosion rate of 0.3 $mg\cdot cm^{-2}\cdot d^{-1}$ in T4 condition and 0.6 $mg\cdot cm^{-2}\cdot d^{-1}$ in T6 condition.

These previous studies show that the Mg-Dy and Mg-Gd based alloying systems have a good combination of mechanical and corrosion properties. So far, there is no report on the Mg-Dy-Gd system. However, the previous investigations indicate these systems can be promising alloy systems for medical applications.

3 Motivation and objectives

Mg and its alloys have been investigated as implants for almost two centuries. However, they are not used in commercial implants. One of the key issues is that Mg alloys do not show a moderate and homogeneous degradation rate to maintain the mechanical integrity of the implant during the healing process. This could be caused by the insufficient mechanical properties, rapid corrosion or localized corrosion. One of the most effective ways to tailor the mechanical and corrosion properties of Mg is by controlling alloying additions. In this work, Mg-Dy alloys and Mg-Dy-Gd-Zr alloys are designed and investigated. Rare earth elements Dy and Gd are selected as main alloying elements due to the following reasons.

- Successful clinical trials of Mg-RE stent have been performed [13]. Although some problems still need to be solved, Mg-RE alloys have shown a good potential for medical applications [14].
- A large concentration of Dy and Gd can be tolerated in *in vitro* cytotoxicity tests [3]. Both Dy and Gd are used as contrast medium for magnetic resonance imaging and they show acceptable biocompatibility [92, 114].
- The solubility of Dy and Gd is high in Mg matrix reaching a maximum value of 25.4 wt.% and 23.5 wt.%, respectively [111]. Thus, both mechanical and corrosion properties can be tailored by changing the alloy content and heat treatment.

The objectives for this work include:

- Investigate the influence of Dy and Gd content on the microstructure, mechanical and *in vitro* bio-corrosion properties of Mg-Dy-Gd-Zr alloys.
- Investigate the influence of heat treatment on the microstructure, mechanical and corrosion properties of Mg-RE alloys.
- Investigate the bio-corrosion products of Mg-RE alloys and their preliminary cytotoxicity.
- Develop new Mg-RE alloys with adjustable mechanical properties, low corrosion rate and good biocompatibility.

4 Experimental procedures

4.1 Materials

Permanent mould direct chill casting (Fig. 12) was used to prepare 8 alloys with nominal chemical compositions listed in Table 12. High-purity Mg (MEL, UK, 99.94 wt.%) was molten in a mild steel crucible under a protective atmosphere (Ar + 2% SF6). Pure Dy (Grirem, China, 99.5 wt.%), pure Gd (Grirem, China, 99.5 wt.%) and Mg-33.3wt.%Zr master alloy were added at a melt temperature of 720 °C. The melt was stirred at 200 rpm for 30 min. After that, the melt was cast using a directly chilled permanent mould casting method. Firstly, the melt was poured into a mould preheated at 500 °C. The filled mould was held at 670 °C for 30 min under the protective gas. Then the whole steel crucible with the melt was lowered into cooling water at a rate of 10 mm/s. When the bottom of steel crucible touched the water, it was stopped for 1 second. When the melt was fully immersed, the solidification finished. The size of ingot was cylinder, Φ12cm × 20cm, and cuboid block, 20 cm ×12 cm × 6 cm, for alloys with and without Zr, respectively.

Fig. 12: Casting furnace (left) and permanent mould direct chill casting system (right)

The chemical compositions of these alloys were analyzed using X-ray fluorescence (XRF) analyzer (Bruker AXS S4 Explorer, Germany) for Dy, Gd and Ni, and using spark optical emission spectroscopy (Spectrolab M9 Kleve, Germany) for Zr, Fe and Cu.

Table 9: Nominal chemical compositions of experimental alloys (wt.%).

alloys	abbreviations	Dy	Gd	Zr	Mg
Mg-5Dy	--	5	--	--	Balance
Mg-10Dy	--	10	--	--	Balance
Mg-15Dy	--	15	--	--	Balance
Mg-20Dy	--	20	--	--	Balance
Mg-10Dy-0.2Zr	D10K	10		0.2	Balance
Mg-8Dy-2Gd-0.2Zr	DG82K	8	2	0.2	Balance
Mg-5Dy-5Gd-0.2Zr	DG55K	5	5	0.2	Balance
Mg-2Dy-8Gd-0.2Zr	DG28K	2	8	0.2	Balance

For binary Mg-Dy alloys, solution treatment (T4) was performed at 520 °C for 24 hours followed by water quenching, and ageing treatment (T6) was performed at 200 °C and 250 °C followed by air cooling. For alloys D10K, DG82K, DG55K and DG28K, T4 was performed at 520 °C for 8 hours followed by water quenching, and T6 was performed at 200 °C followed by air cooling.

4.2 Microstructure

4.2.1 Optical microscopy

Specimens were cut from the same location in different ingots to avoid the influence of solidification condition on microstructure, as illustrated in Fig. 13. For the preparation and examination of optical microstructure, specimens were mounted with cold setting polymers. Powdered and liquid Demotec 30 was mixed in the ratio 1:1, and then poured into the mounting mould with specimen inside. The polymer paste took approximately 15 min to solidify under room temperature. After solidification of the polymer, the mounting moulds were removed carefully in case of deformation of specimens. Specimens were then ground using silicon carbide emery paper up to 2500 grit, and then polished with 0.05 µm colloidal silica (OPS). The polished surface was finally cleaned using ethanol and dried under blowing warm air. Specimens were etched in a solution containing 8 g picric acid, 5 ml acetic acid, 10 ml distilled water and 100 ml ethanol, and quickly washed using ethanol and dried with blowing warm air. Macro structure was investigated using a high-resolution scanner (HP Scanjet 4890). Microstructure was characterized using light microscope (Reichert-Jung MeF3) with a digital camera attachment. Grain sizes were determined using the line intercept methods [115].

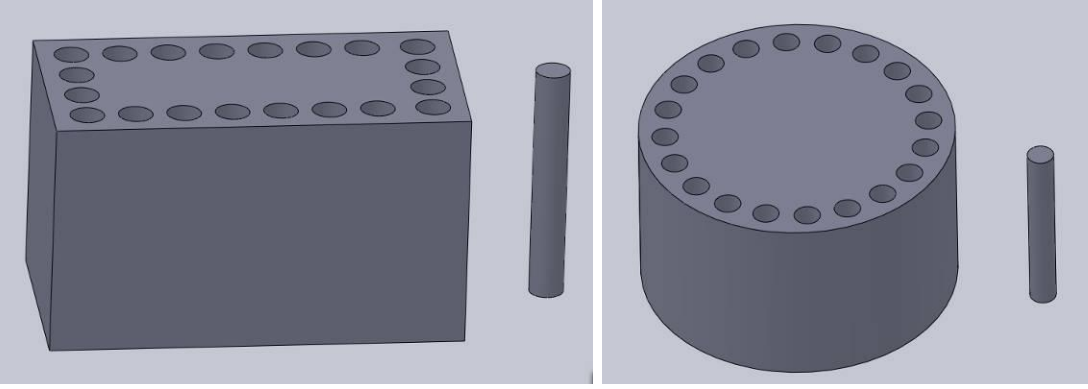

Fig. 13: Schematic illustration about the positions of specimens' preparations

4.2.2 Scanning electron microscopy

Specimens were ground and polished with the same method described in optical microscopy and were further electropolished using an electrolytic apparatus (LectroPol-5, Struers Inc) at a voltage of 30 V for 70 seconds. The composition of the electrolyte is shown in Table 10. A Zeiss Ultra 55 (Carl Zeiss GmbH, Oberkochen, Germany) scanning electron microscope (SEM) equipped with energy dispersive X-ray (EDX) analyzer was used to observe the microstructure at 15KV. EDX was used to analyze the compositions of different phases with a minimum live time of 50 seconds.

Table 10: Composition of electrolyte for electropolishing.

Component	Sodium Thiocyanate Dihydrate	Citric Acid	Ethanol	Propanol	Hydroxyquinoline	Perchloric Acid
amount	60 g	75 g	800 ml	100 ml	10 g	15 ml

4.2.3 Transmission electron microscopy

Mg-20Dy alloy aged at 250°C for 16 h, aged at 200°C for 168h, and DG28K alloy aged at 200°C for 72 h were selected for transmission electron microscopy (TEM). Specimens were ground mechanically to about 400 μm and then cut to Φ3 mm discs with an Abrasive Slurry Disc Cutter (Model 360, South Bay Technology, Inc). The discs were mechanically ground to 120 μm and further thinned by electropolishing in a twin jet electropolisher using a solution of 2.5 % $HClO_4$ and 97.5 % ethanol at about −45 °C and a voltage of 40 V. Afterwards, the polished specimens were washed in acetone. The TEM examinations were carried out on a Philips CM 200 instrument with an energy dispersive X-ray analysis (EDX) system operating at 200 kV.

4.2.4 XRD analysis

For phase analysis, X-ray diffraction (XRD) measurements were performed using a diffractometer (Siemens D5000, Germany) with Cu K-α_1 radiation (wavelength λ= 0.15406 nm). The measurement was carried out at 40 kV voltage and 40 mA current, with a step size of 0.02 degree. Specimens were prepared by grinding to 2500 grit with silicon carbide emery paper. CaRIne crystallography software (version 3.1) was used to simulate the diffraction peaks of β′ phase based on its crystal structure (orthorhombic, a = 0.64 nm, b = 0.22 nm, c = 0.52 nm) [115, 116].

4.3 Mechanical Properties

4.3.1 Hardness

In order to investigate the influence of alloying elements content and heat treatment on the mechanical properties, Vickers hardness was measured. Specimens were prepared by mounting and grinding up to 2500 grit with silicon carbide emery paper. Measurement was carried out using a Vickers hardness testing machine (KARL FRANK GMBH) with a load of 5 Kg and a dwell time of 10 seconds. An average of 10 measurements was made for each condition as shown in Fig. 14.

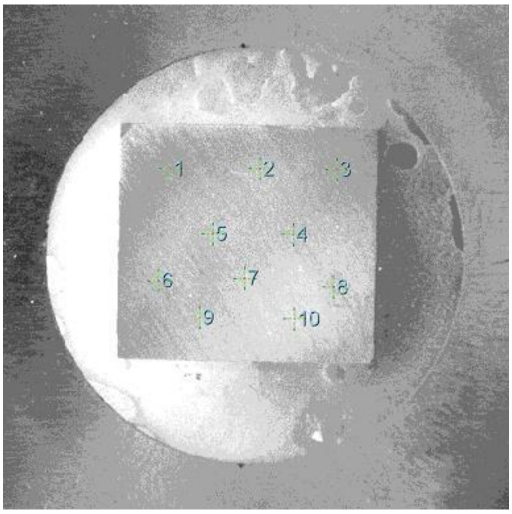

Fig. 14: A specimen after hardness test. The specimen size is 18 mm × 18 mm.

4.3.2 Tension and Compression

Tension and compression tests were performed at room temperature using a Zwick 050 testing machine (Zwick GmbH & Co., KG, Ulm, Germany) according to DIN EN 10002 [49] and DIN 50106 [112], respectively. Fig. 15 shows the pictures of tensile and compressive specimens. Tensile specimens with a gauge length of 30 mm, a diameter of 6 mm and threaded heads were used. The compressive specimens were cylinders with a height of 16.5 mm and a diameter of 11 mm. Both tension and compression tests were done under a strain rate of 1×10^{-3} s^{-1}. At least three specimens were tested under each condition.

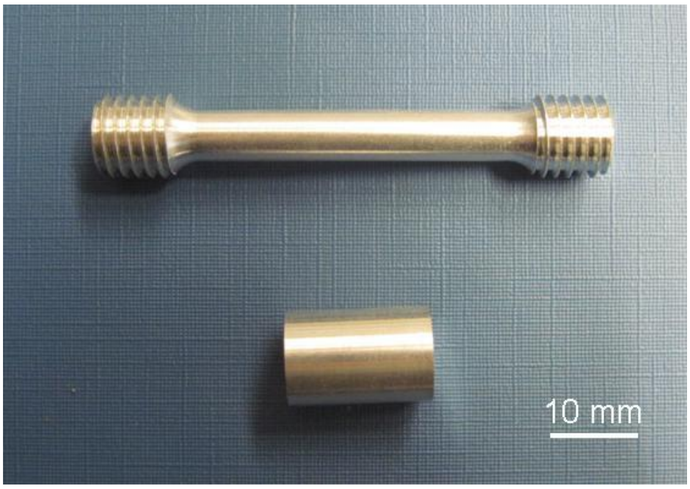

Fig. 15: Tensile and compressive specimens.

4.4 Corrosion rate

Weight loss tests were performed in two conditions:

- 0.9 wt. % NaCl solution at room temperature.
- Cell culture medium (CCM) consisting of Dulbecco's modified eagle medium (DMEM) (Sigma Aldrich Chemie, Taufkirchen, Germany) and 10% fetal bovine serum (FBS Gold, PAA Laboratories, Linz, Austria) in an incubator under cell culture conditions (37°C, 21% O_2, 5% CO_2, 95% rH), as shown in Fig. 16. The composition of DMEM is listed in Table 11.

Fig. 16: Incubator used in corrosion tests.

Table 11: Composition of DMEM (mg/L)

Inorganic salts	Calcium Chloride ($CaCl_2 \cdot 2H_2O$)	264
	Ferric Nitrate ($Fe(NO_3)_3 \cdot 9H_2O$)	0.1
	Magnesium Sulfate ($MgSO_4 \cdot 7H_2O$)	200
	Potassium Chloride (KCl)	400
	Sodium Bicarbonate ($NaHCO_3$)	3700
	Sodium Chloride (NaCl)	6400
	Sodium Phosphate Monobasic($NaH_2PO_4 \cdot 2H_2O$)	141
Organic salts	Vitamins	35.6
	Amino Acids	1852
	D-Glucose (Dextrose)	4500
	Phenol Red	15
	Sodium Pyruvate	110

The specimens were prepared by grinding each side with 2400 grid emery paper and degreasing the surfaces with ethanol prior to corrosion tests. For the corrosion tests in CCM, the specimens were sterilized in 70% ethanol for 15 min before the start of tests. Then all procedures were carried out under sterile conditions. The specimens were either immersed in NaCl solution for 3 d or immersed in CCM for 14 d, respectively. The corrosion products were removed by immersing the corroded specimens in chromic acid (180 g/l) for 20 min at room temperature. The average corrosion rate was calculated in millimetre per year (mm/y) using the following equation:

$$CR = \frac{8.76 \times 10^4 \times \Delta g}{A \cdot t \cdot \rho}$$

Equation 3

Where Δg is weight change in g, A is initial surface area in cm^2, t is immersion time in hours (h) and ρ is density of the alloy in $g \cdot cm^{-3}$. At least three specimens were tested for each condition.

4.5 Characterization of corrosion layer

4.5.1 Measurement of corrosion layer thickness

The thickness of the corrosion layer was measured with a coating thickness gauge (MiniTest 600, ElectroPhysik, Germany) and was further verified by observing the cross section of the corroded sample with optical microscope. For preparation of cross section, the specimens were embedded into resin and ground to 4000 grid emery paper perpendicularly to the corroded surface. After grinding, the specimens were mechanically polished, and then cleaned in 100% ethanol in an ultrasonic bath to remove contaminations on the surface.

4.5.2 Corrosion morphology observation

Micro corrosion morphology observations and compositions analysis of corrosion layer were performed using a Zeiss Ultra 55 scanning electron microscope equipped with energy dispersive X-ray (EDX) analyzer and operated at 15kV. The cross section of the corroded sample (after 3 days immersion and drying) was prepared by cutting with 30 keV gallium focused ion beam (FIB), equipped on a SEM (Auriga, Zeiss, Oberkochen, Germany). To prevent destroying corrosion layer and obtain precise cutting along the corrosion layer, a layer of platinum was deposited on the corroded surface. The morphology observation, line scanning and mapping of the cross section of the corrosion layer were performed directly after cutting, operating at 15 kV.

4.5.3 XPS analysis

X-ray induced photoelectron spectroscopy (XPS) experiments were carried out on a Kratos Axis Ultra DLD (Kratos Analytical Ltd., Manchester, UK) attached with a 15 kV

X-ray gun using monochromatic Al K-α radiation. Corrosion layer of Mg-10Dy alloy and pure Dy metal were prepared by 24 h immersion in the CCM under cell culture condition. Samples were cleaned with distilled water and dried under vacuum conditions. The measured area was 700 µm × 300 µm and the pass energy was 40 eV at the regions of measurements and 160 eV for survey scans. As a result of nonconductive nature of the corrosion products, a charge neutralizer was used to correct the chemical shifts caused by charging. Additionally, argon ions (4000 eV) were used to etch the specimens in order to investigate the composition of corrosion layer at different depth. The applied sputtering rate is about 40nm/min. Curve fitting of the spectra was performed with Casa 2.3.15 software (Casa Software Ltd., Teighnmouth, Devon, UK, 2003). Element binding energy database used is the NIST Standard Reference Database 20, Version 3.5.

4.6 Evaluation of cytotoxicity

4.6.1 Specimens preparation

The cytotoxicity of new developed alloys was studied via direct cell adhesion tests. Cylindrical specimens with a diameter of 10 mm and a height of 1.5 mm were prepared by electrical discharge machining. Both sides of these specimens were ground with 2500 grit emery paper and ultrasonically cleaned in ethanol for 3 min and then dried in air. Pure Mg specimens were also investigated as a reference, to evaluate the influence of alloying elements on the cytotoxicity. Before cytotoxicity tests, all specimens were sterilized in 70% ethanol for 15 min and pre-incubated for 2 h and 3 days under cell culture condition in CCM. Agarose coating was prepared on 12-well-plates (Nunc, Wiesbaden, Germany) to avoid growing of cells on the plates.

4.6.2 Isolation and culture of primary human osteoblasts

Osteoblasts were obtained from bone chips of a patient undergoing total hip arthroplasty following the protocol of Gallagher [117]. The isolation protocol was approved by the local ethic committee. Cancellous bone was removed from the femoral head with bone rongeurs in pieces of about 5 mm diameter. Bone marrow and non-bone components are removed by thoroughly vortexing in PBS repeatedly for 30 s, during which the PBS was replaced continuously. After the bone fragments became white and ivory-like they were cultured in DMEM Glutamax-I with 10%

FBS,1% penicillin and 100 mg/L streptomycin (Invitrogen Corporation, 166 Karlsruhe, Germany) for about 10 days without changing the medium. Then medium was changed every 2–3 days. Passage was done at 70–80% confluence. Experiments were performed with cells in the 2^{nd} passage.

4.6.3 Direct cell contact tests

The schematic illustration of the direct cell contact test is shown in Fig. 17. Osteoblasts were seeded on top of the specimens in 12-well-plates in 50 µl solution at a density of 100,000 cells per specimen and incubated for 40 min for the cells to settle down. Thereafter, 3 ml CCM was added to each well. After 3 days and 7 days incubation, the cytotoxicity of specimens was evaluated using SEM and fluorescence microscopy. Two samples were investigated for each condition.

- SEM observation

After incubation, the specimens were washed with PBS and then immersed into 2.5% glutaraldehyde solution over night to fix the cells. The specimens were then immersed into 1% osmium tetroxide for 30 min for staining. Gradual dehydration was carried out in a graded aqueous alcohol series from 20 to 100 vol.% isopropanol (2-propanol, Merck; Darmstadt, Germany). Finally, the specimens were dried via critical point drying in isopropanol (Leica EM CPD030, Leica Mikrosysteme, Wetzlar, Germany). Morphology of cells on the specimens was observed using SEM operated at 1 kV.

- Fluorescence microscopy (live dead staining)

LIVE/DEAD Viability/Cytotoxicity Kit (Invitrogen) for mammalian cells was used for staining. The staining solution consisted of 98.6 vol.% CCM, 0.4 vol.% Calcein AM and 1 vol.% Ethidiumhomodimer-1. After incubation, the specimens were washed with PBS and then covered with the staining solution. The samples were then incubated in cell culture condition for 20 min, and staining solution was replaced by the CCM. Fluorescence microscope (Nikon TI Eclipse) was used to record the fluorescence images. Four images were taken randomly and used for cell viability calculation using the following equation.

$$CV = \frac{NL}{NL + ND} \times 100\%$$

Equation 4

Where CV is the cells viability, NL is the numbers of live cells and ND is the numbers of dead cells.

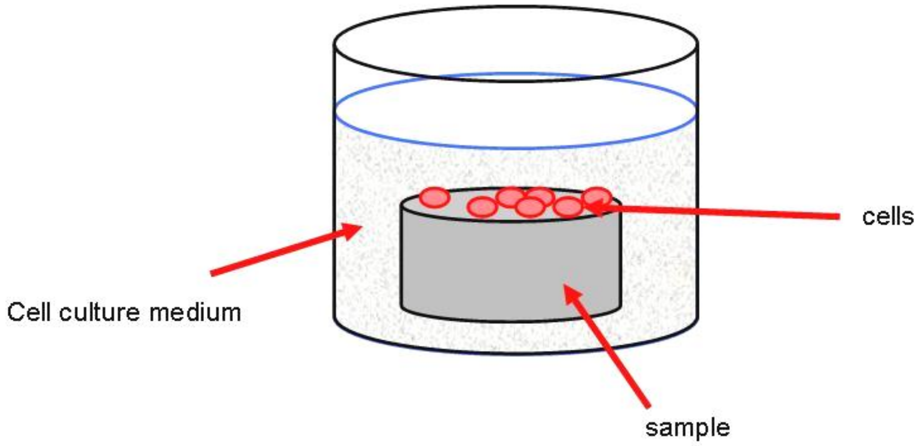

Fig. 17: Schematic illustration of a direct cell adhesion test.

5 Results

5.1 Mg-Dy alloys

5.1.1 Chemical composition

The actual composition of the alloys investigated were measured using spark optical emission spectroscopy (OES), as listed in Table 12. The content of Ni can not be determined by the spark optical emission spectroscopy due to the overlap of Ni peaks with the strong Dy peaks. Therefore, the content of Ni was determined by XRF and the Ni content was below the threshold value for 0.004 wt.%.

Table 12: Actual chemical compositions of experimental alloys (wt.%).

Alloys	Dy	Fe	Ni	Cu	Mg
Mg-5Dy	4.5	0.004	<0.004	0.07	Balance
Mg-10Dy	9.2	0.005	<0.004	0.007	Balance
Mg-15Dy	13.0	0.007	<0.004	0.008	Balance
Mg-20Dy	18.6	0.009	<0.004	0.01	Balance

5.1.2 Microstructure characterization

5.1.2.1 As cast microstructures

The optical macrostructure of Mg-Dy alloys in the as-cast (F) condition is shown in Fig. 18. Very inhomogeneous microstructure is formed due to the fast solidification experienced during the direct chill casting (water quenching). The grain size is smaller at the edge than that at the centre. The influence of Dy content on the grain size was investigated by measuring the grain size at the edge of the ingots for all alloys. The grain size decreases significantly with the increase in the Dy content from 5 wt.% to 10 wt.%, but further addition of Dy has less influence on the grain size, as shown in Table 13.

The optical microstructures of the as-cast Mg-Dy alloys (Fig. 19) are typical dendritic structure that is observed in many cast alloys. The dendritic morphology becomes smaller and smaller with the increase in the Dy content. A small number of second phase particles were found in the Mg-5Dy, Mg-10Dy and Mg-15Dy alloys. Both size and amount of the secondary phases increased significantly in Mg-20Dy alloy but the particles were not resolved by optical microscopy.

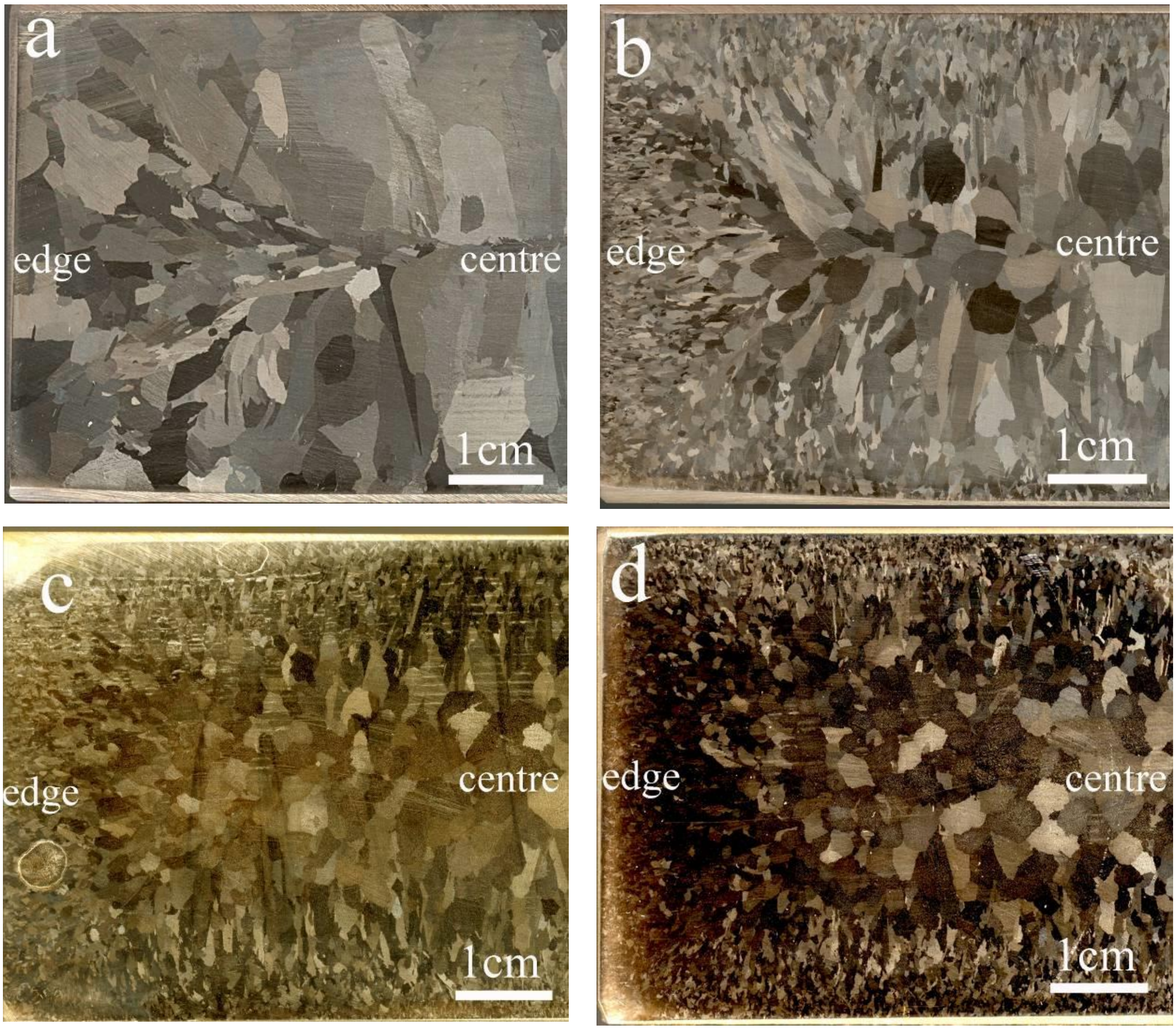

Fig. 18: Optical macrostructures of as cast Mg-Dy alloys: (a) Mg-5Dy; (b) Mg-10Dy; (c) Mg-15Dy; (d) Mg-20Dy.

Table 13: Grain size of Mg-Dy alloys at edge (mm).

Alloy	Mg-5Dy	Mg-10Dy	Mg-15Dy	Mg-20Dy
Edge (F)	3.34±2.87	0.61±0.46	0.56±0.26	0.64±0.23
Edge (T4)	3.82±4.14	1.23±0.68	0.79±0.44	0.52±0.43

Fig. 20 illustrates the SEM microstructure of the as-cast Mg-Dy alloys. The bright areas shown in the pictures are caused by the segregation of Dy, which mainly locates at the interdendritic region and the grain boundaries. With the increase in the Dy content, both the area fraction of Dy segregation and the amount of secondary phases increase. When the content of Dy reaches 20 wt.%, the amount of second phase with a spherical morphology increases significantly.

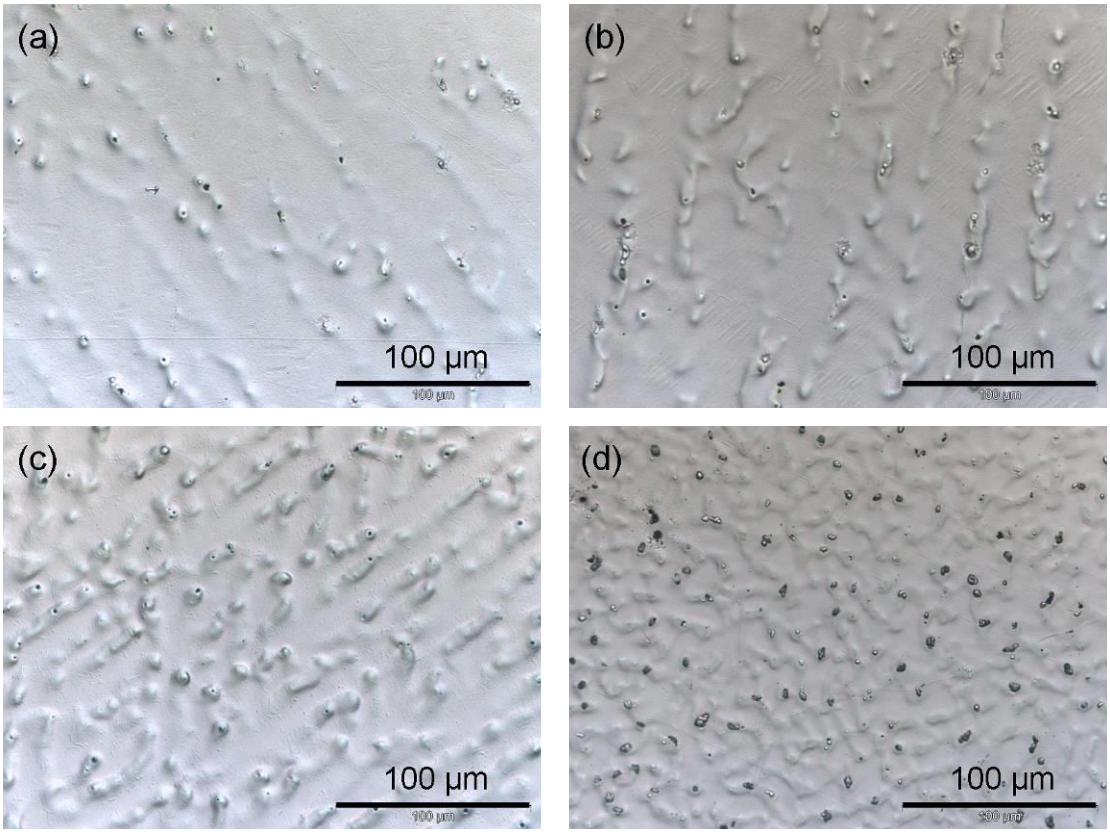

Fig. 19: Optical microstructures of as-cast: (a) Mg-5Dy; (b) Mg-10Dy; (c) Mg-15Dy; (d) Mg-20Dy alloys.

The distribution of Dy in the different regions was analyzed using EDX (Table 14). The Dy content in Mg matrix (F), as indicated by character A, is about half the composition of the alloy. For example, the content of Dy in the Mg matrix is 2.17 wt.% and 10.3 wt.% for Mg-5Dy and Mg-20Dy alloys, respectively. The Dy content in the segregated area, as indicated by character B, is much higher than that in the matrix and it increases with the increased Dy content. The content of Dy in the segregated regions increase from 19.26 wt.% to 29.2 wt.% when the Dy addition increases from 5 to 20 wt.%. EDX analysis showed the composition of the second phase to be about 85 at.% Mg, 14 at.% Dy and 1 at.% O (Fig. 20 (e)). The SEM microstructure shows that the amount of second phase is very low for Mg-5Dy, Mg-10Dy and Mg-15Dy alloys. Thus Mg-20Dy alloy was selected for the XRD phase analysis to determine the second phase and the XRD shows that the second phase is $Mg_{24}Dy_5$ Fig. 21). The TEM micrograph of the second phase and the corresponding diffraction pattern which can be indexed as the β phase [118] (Fig. 22).

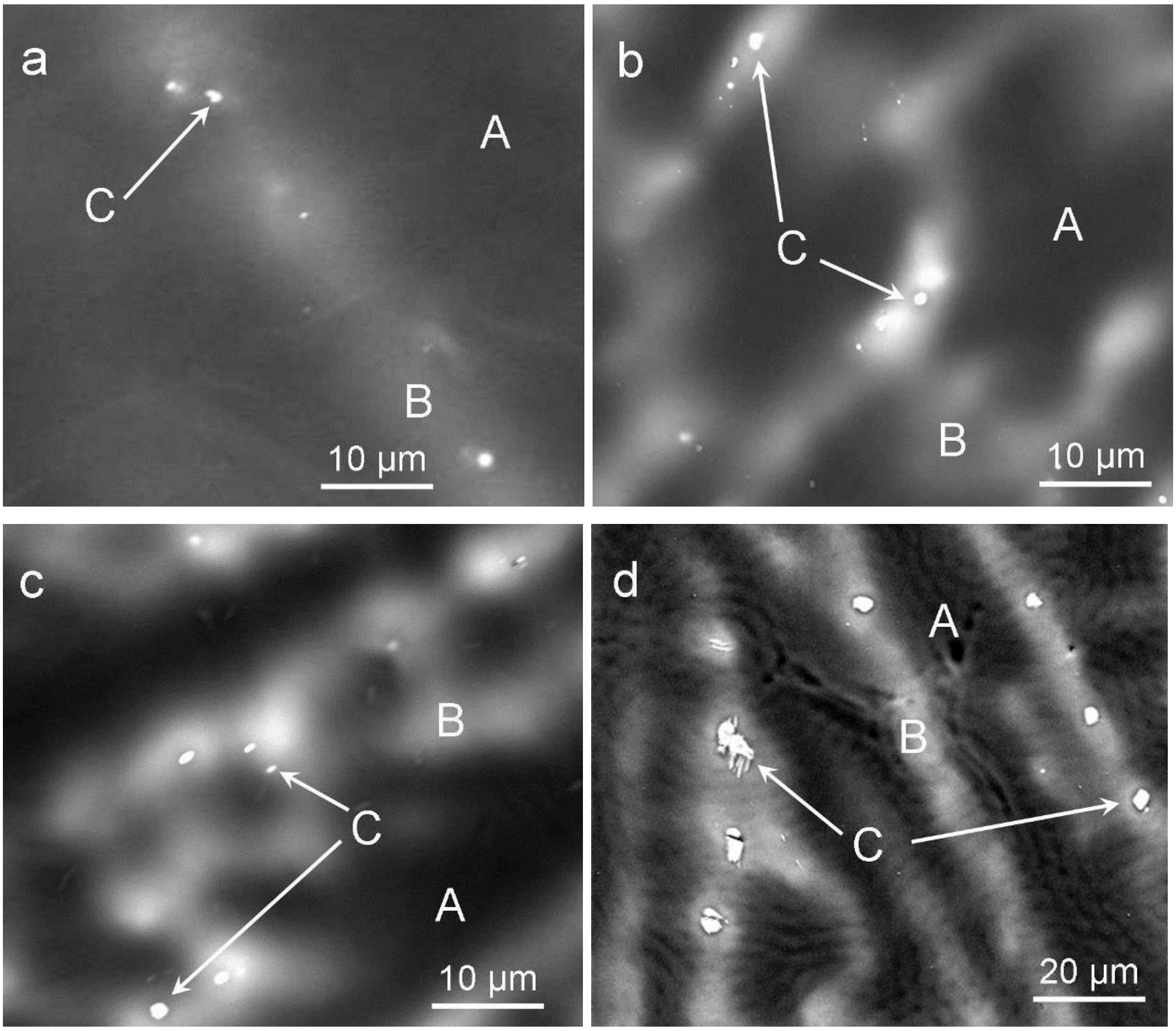

Fig. 20: SEM (BSE) microstructures of as-cast Mg-Dy alloys: (a) Mg-5Dy; (b) Mg-10Dy; (c) Mg-15Dy; (d) Mg-20Dy; (A: Mg matrix; B: segregation of Dy; C: second phase).

Table 14: Distribution of Dy in different areas of Mg-Dy alloys (wt.%).

alloys	Mg-5Dy	Mg-10Dy	Mg-15Dy	Mg-20Dy
Matrix (F)	2.17±0.15	4.92±0.09	7.81±0.36	10.3±0.62
segregation region of Dy (F)	19.51±0.68	21.67±0.86	25.345±0.54	28.9±0.92
Second phase (F)	---	---	---	51.8±1.20
Matrix (T4)	4.38±0.05	8.23±0.04	12.38±0.25	18.01±0.18

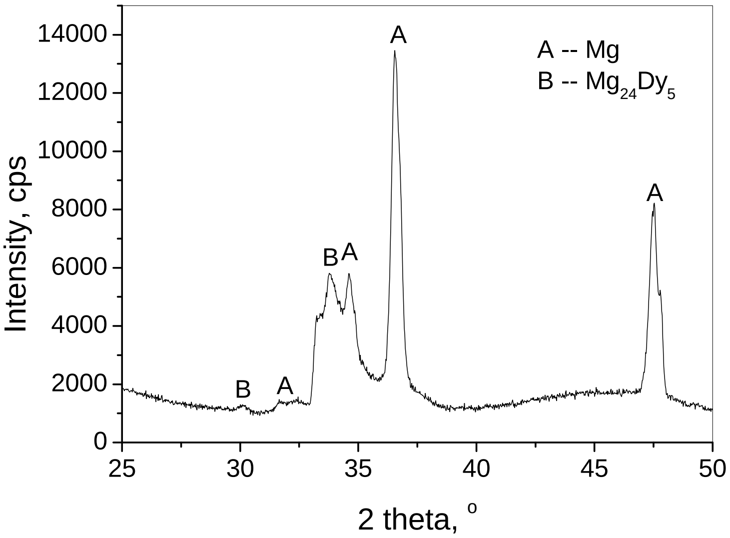

Fig. 21: XRD pattern of the as-cast Mg-20Dy alloy in as cast condition.

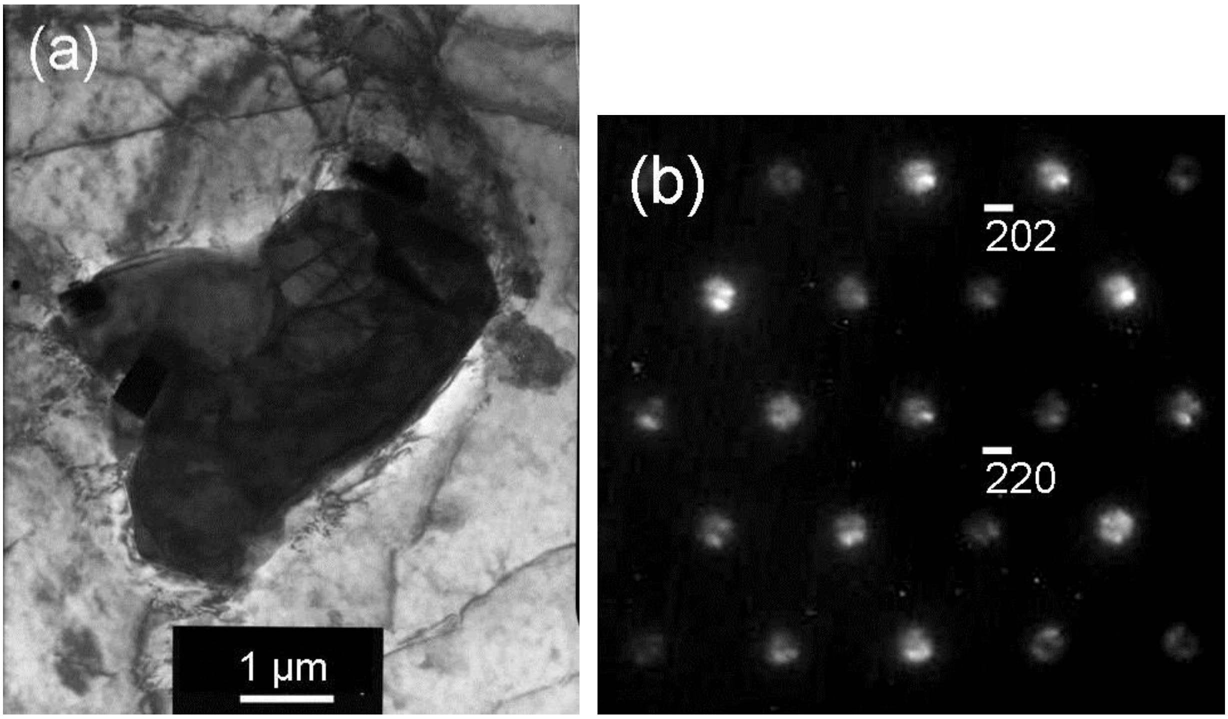

Fig. 22: (a): TEM micrograph of second phase in the as-cast Mg-20Dy alloy and (b) the corresponding diffraction pattern along zone axis [111].

5.1.2.2 Microstructures after T4 treatment (520 °C/24 h)

Based on Mg-Dy phase diagram (Fig. 9) and previous result on binary Mg-Gd alloys [34], T4 treatment was performed at 520 °C for 24 hours. After T4 treatment, the grain size of Mg-Dy alloys increased but it is difficult to determine an exact grain size due to inhomogeneity in the grain size observed within the microstructure (Table 13). Fig. 23 shows the microstructure of Mg-Dy alloys after T4 treatment. The segregation of Dy is completely eliminated and only very few precipitates remained in the alloys, mainly in Mg-20Dy alloy. The Dy content in the matrix was analyzed using EDX and the measured area is indicated by arrow D. As listed in Table 14, the Dy content in the matrix of Mg-5Dy, Mg-10Dy, Mg-15Dy and Mg-20Dy alloys are 4.38, 8.23, 12.38 and 18.01 wt.%, respectively, which are close to the actual Dy content. This indicates that the Dy has dissolved into the Mg matrix following the T4 treatment.

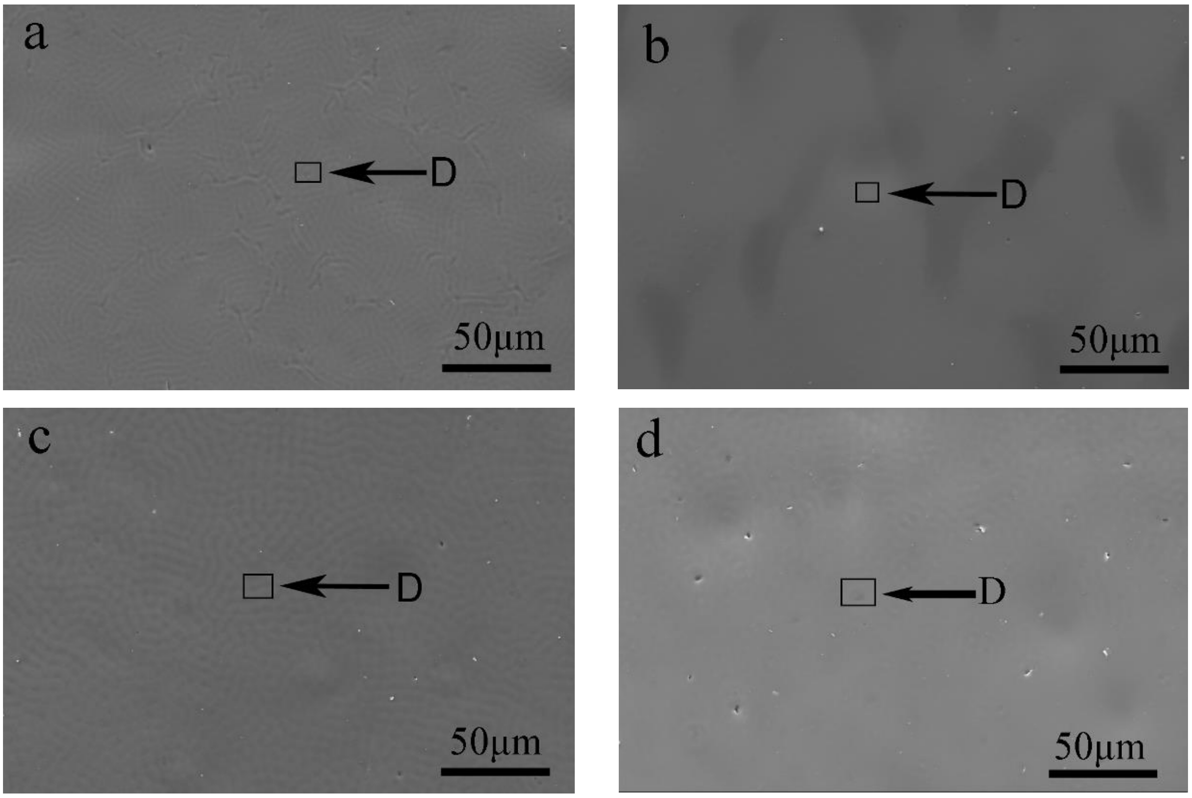

Fig. 23: Microstructures of Mg-Dy alloys after T4 treatment (520 °C for 24h): (a) Mg-5Dy; (b) Mg-10Dy; (c) Mg-15Dy; (d) Mg-20Dy.

5.1.2.3 Microstructures after T6 treatment

The age hardening response was measured for the Mg-(10-20)Dy alloys at 200 and 250 °C (Fig. 24). The solubility of Dy is approximately 10 wt.% at 200 °C according to the Mg-Dy binary phase diagram [111] thus the age hardening response of the Mg-5Dy alloy was not investigated.

At 200 °C, the age hardening response may exist for all three alloys but only very small changes in hardness can be observed for the Mg-10Dy and Mg-15Dy. For Mg-20Dy alloy aged at 200°C, there is little change of the hardness in the initial period (stage I). And then, the hardness increases apparently with the increase of ageing time up to 168 h (stage II). When the ageing time exceeds 168 h (stage III), the increasing rate of hardness becomes very slow. The maximum hardness was not observed even after ageing for 480 h. At 250 °C, none of the alloys investigated show appreciable age hardening and the hardness change is not significant.

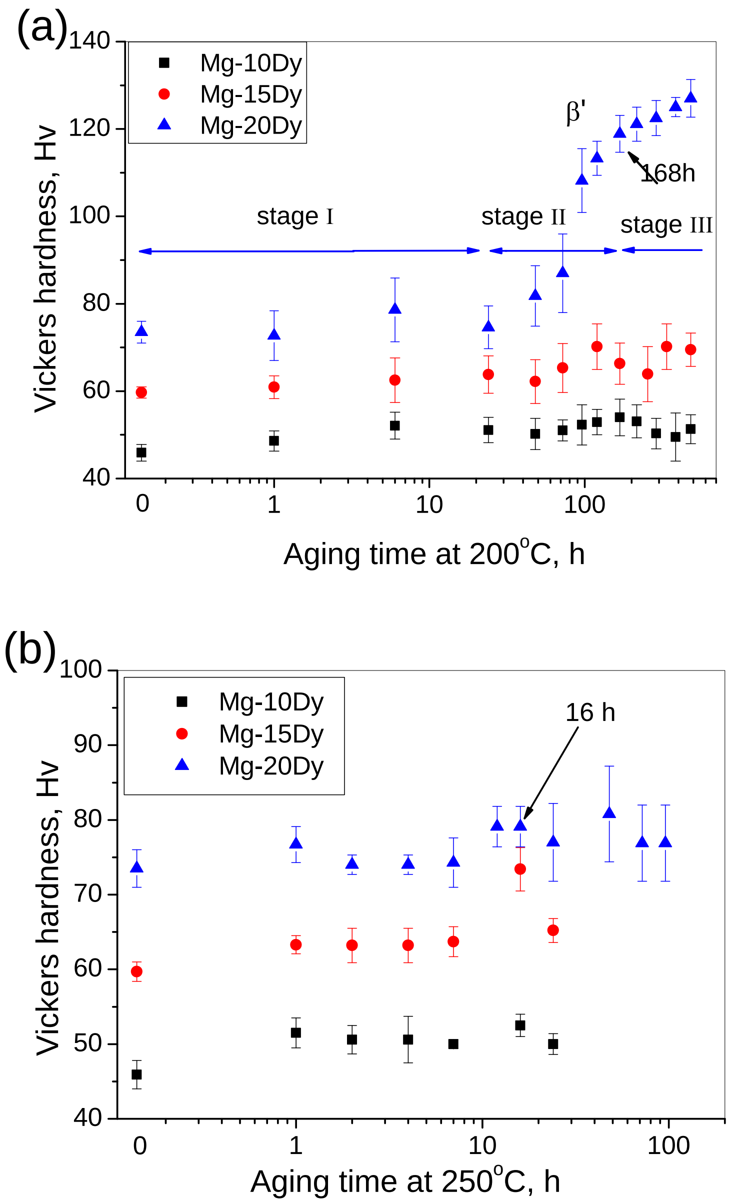

Fig. 24: Vickers hardness as a function of ageing time for Mg-Dy alloys aged at: (a) 200°C and (b) 250°C.

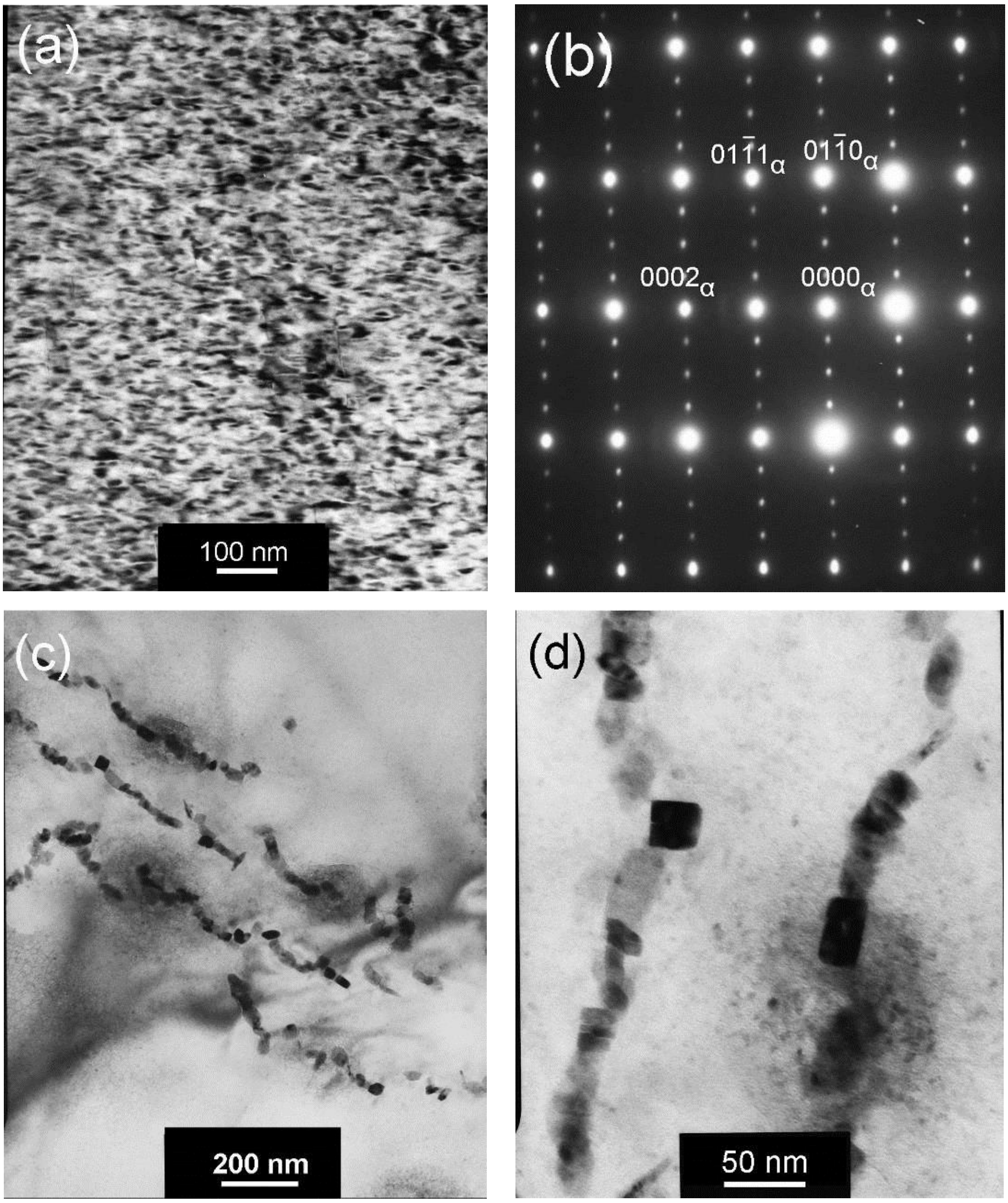

Fig. 25: TEM microstructure and diffraction pattern of Mg-20Dy alloy: (a) aged at 200 °C for 168 h and (b) corresponding diffraction pattern (the zone axis is $[2\bar{1}\bar{1}0]_\alpha$); (c) aged at 250 °C for 16 h at low magnification; (d) aged at 250 °C for 16 h at high magnification.

Based on the age hardening curves TEM investigations on the precipitates were performed for Mg-20Dy alloy aged at 200°C for 168 h (T6-1) which is the end of rapid increase in hardness and at 250°C for 16 h (T6-2), as shown in Fig. 25. The microstructure after T6-1 treatment shows that very fine precipitates homogeneously distribute in all over the matrix (Fig. 25 (a)). The selected area electron diffraction pattern obtained with the beam parallel to $[2\bar{1}\bar{1}0]_\alpha$ shows additional reflection (Fig.

25 (b)). Analysis of these reflections indicates that the fine precipitates are the metastable phase β′, which in Mg-Gd binary has been determined to have a composition of $Mg_{13}RE_3$ and a base-centred orthorhombic structure, with lattice parameters a = 0.64 nm, b = 2.22 nm, c = 0.52 nm [116]. This is independently verified with XRD analysis (Fig. 26). The orientation relationship between β′ and matrix is $(001)_{\beta'} // (0001)_{\alpha}$, $[100]_{\beta'} // [2\bar{1}\bar{1}0]_{\alpha}$ [118]. In T6-2 condition, only a few precipitates are formed and the distribution of such precipitates is not uniform (Fig. 25 (c)). The size of the precipitates is about 30- 50 nm in length and 10-30 nm in width (Fig. 25 (d)). Due to the non-uniform distribution of these precipitates and relatively small volume fraction, selected area diffraction patterns could not be recorded.

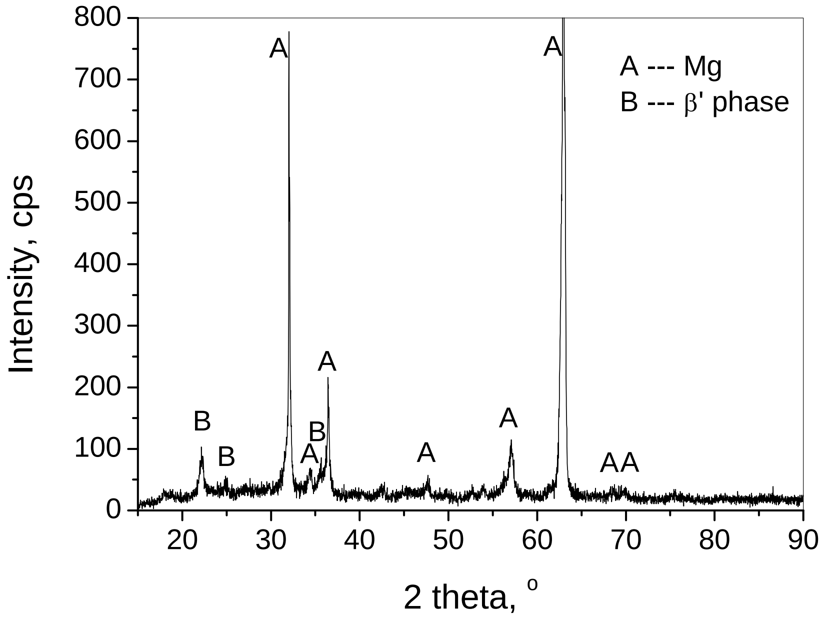

Fig. 26: XRD pattern of Mg-20Dy alloy aged at 200°C for 168 h.

5.1.3 Mechanical properties

5.1.3.1 Hardness

Fig. 27 shows the Vickers hardness of Mg-Dy alloys in different conditions. In the as-cast condition, the Vickers hardness is approximately 41 HV for Mg-5Dy alloy. With the increase in Dy content, the hardness increases and reaches around 78 HV for Mg-20Dy alloy. After T4 treatment, the Vickers hardness slightly decreases for all alloys. After T6-1 treatment, although the improvement in hardness is still very small for Mg-10Dy and Mg-15Dy alloys, it is significant for Mg-20Dy alloy, increasing from

72 HV to 116 HV. After T6-2 treatment, the hardness is only marginally improved for all tested alloys compared with T4 condition.

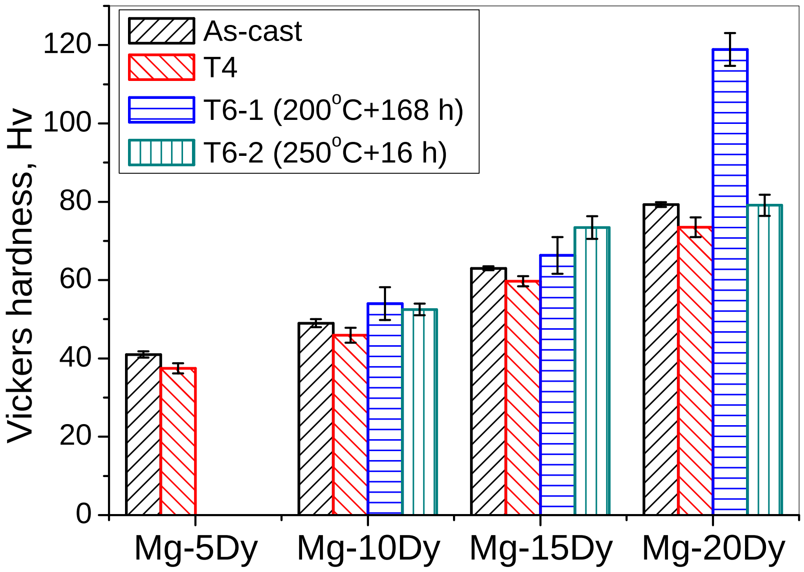

Fig. 27: Vickers hardness of Mg-Dy alloys in different conditions.

5.1.3.2 Tensile properties

The tensile yield strength (TYS) of Mg-Dy alloys tested following different processing conditions for Mg-Dy alloys are shown in Fig. 28 (a). In the as cast condition the tensile yield strength increases with the increase in the amount of Dy. A maximum of 112 MPa was reached with a Dy content of 20wt%. After T4 treatment, the TYS decreases for all alloys. For example, it reduces from 82 MPa and 105 MPa to 63 MPa and 68 MPa for Mg-10Dy and Mg-15Dy alloys, respectively. T6-1 treatment leads to a slight improvement of the TYS for Mg-10Dy alloy. A significant improvement from 110 MPa to 167 MPa is obtained for Mg-20Dy alloy after T6-1 treatment due to precipitation hardening. After T6-2 treatment, the TYS remains unchanged for Mg-10Dy and Mg-15Dy alloys and increases slightly for Mg-20Dy alloy compared with T4 condition.

The ultimate tensile strength (UTS) of Mg-Dy alloys in different conditions are illustrated in Fig. 28 (b). In the as-cast condition, Mg-5Dy alloy has the lowest UTS with a value of about 77 MPa. With the increase in the Dy content to 10wt% the UTS increases to 115 MPa but further increase in the Dy content has a little influence on the UTS. After the T4 treatment, a little change in the UTS is observed for the Mg-5Dy, Mg-15Dy and Mg-20Dy alloys, but the UTS of Mg-10Dy alloy reduces from 130 MPa to 103 MPa. After T6-1 treatment, the UTS significantly increases from 147 to 219 MPa for Mg-20Dy alloy, while no change in the UTS is observed for the Mg-10Dy and Mg-15Dy alloys. After T6-2 treatment, the UTS remain unchanged for all tested alloys compared with T4 condition.

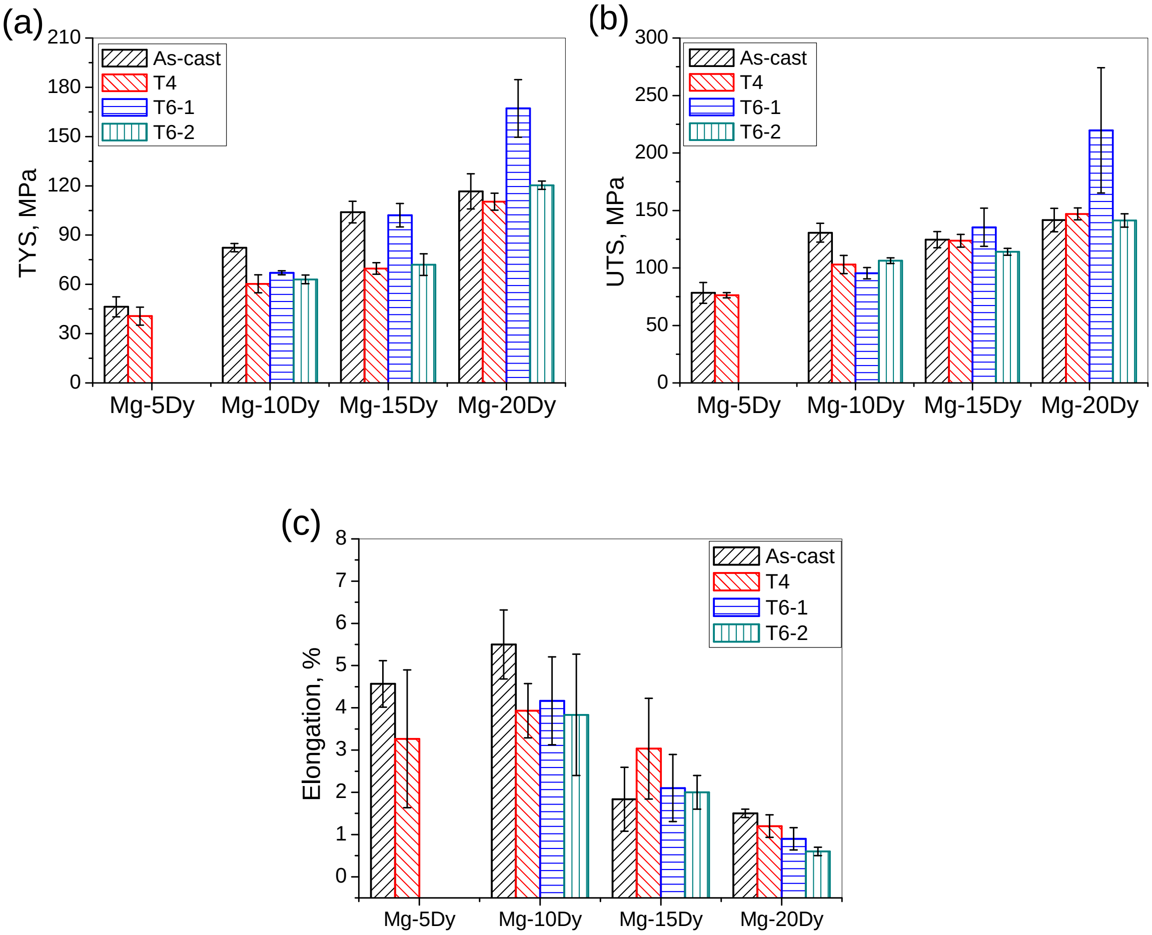

Fig. 28; Tensile properties of Mg-Dy alloys in different conditions: (a) tensile yield strength (TYS); (b) ultimate tensile strength (UTS); (c) elongation

The tensile elongations to failure for Mg-Dy alloys under different conditions are presented in Fig. 28 (c). Due to inhomogeneous microstructure large variations in the tensile elongations were observed. In the as-cast condition, the tensile elongation increases by a small amount with increased Dy content from 5 wt.% to 10 wt.%. Above 10wt% Dy the elongation decreases. Considering the large deviation, the elongation stays at the same level for Mg-(5-15)Dy alloy under different conditions. For Mg-20Dy alloy, the elongation reduces after both T6-1 and T6-2 treatment.

5.1.3.3 Compressive properties

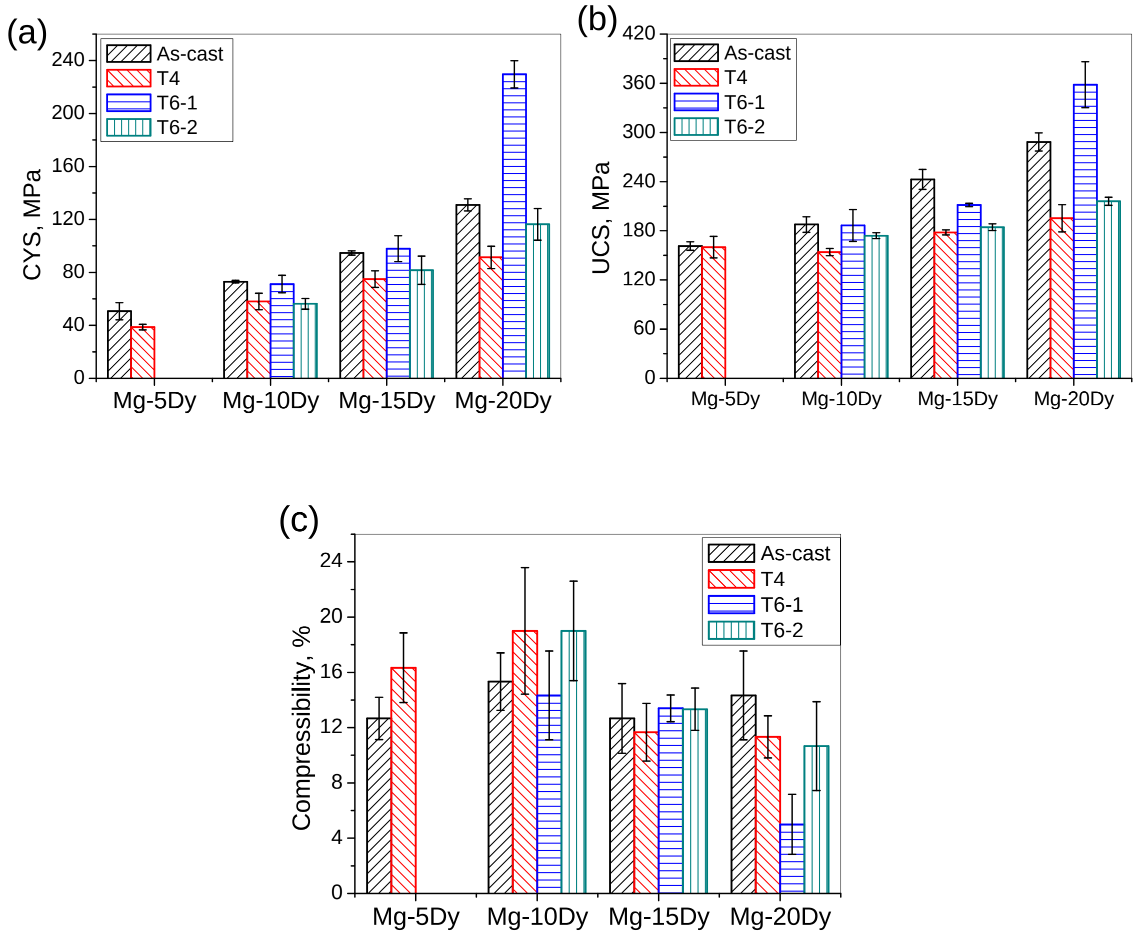

Fig. 29: Compressive properties of Mg-Dy alloys in different conditions: (a) compressive yield strength (CYS); (b) ultimate compressive strength (UCS); (c) Compressibility (strain at maximum stress point)

The compressive properties of Mg-Dy alloys under different processing conditions are summarized in Fig. 29. The compression results follow a similar trend to that of tension. In the as-cast condition, both the compressive yield strength (CYS) and ultimate compressive strength (UCS) are enhanced linearly with the increase of Dy content. They reach to 136 MPa and 290 MPa for Mg-20Dy alloy, respectively (Fig. 29 (a, b)). The compressibility is similar between the alloys in the as-cast condition at ~ 13% (Fig. 29 (c)). After T4 treatment, both of the CYS and UCS decrease for all alloys. Following T4 heat treatment the CYS and UCS are 84 MPa and 186 MPa for Mg-20Dy alloy, respectively (Fig. 29 (a, b)). The compressibility remains at the same level after T4 treatment considering the large deviation (Fig. 29 (c)). After T6-1 treatment, there is a small increment in the CYS for the Mg-(10-15) Dy alloys while a significantly high increment from 116 MPa to 229 MPa for Mg-20Dy alloy due to formation of fine scale precipitates (Fig. 29 (a)). T6-2 treatment had no effect on the compression properties of Mg-10Dy and Mg-15Dy alloys, while a marginal improvement in the CYS for Mg-20Dy alloy was observed (Fig. 29 (a)).

5.1.4 Corrosion in NaCl

5.1.4.1 Corrosion rate

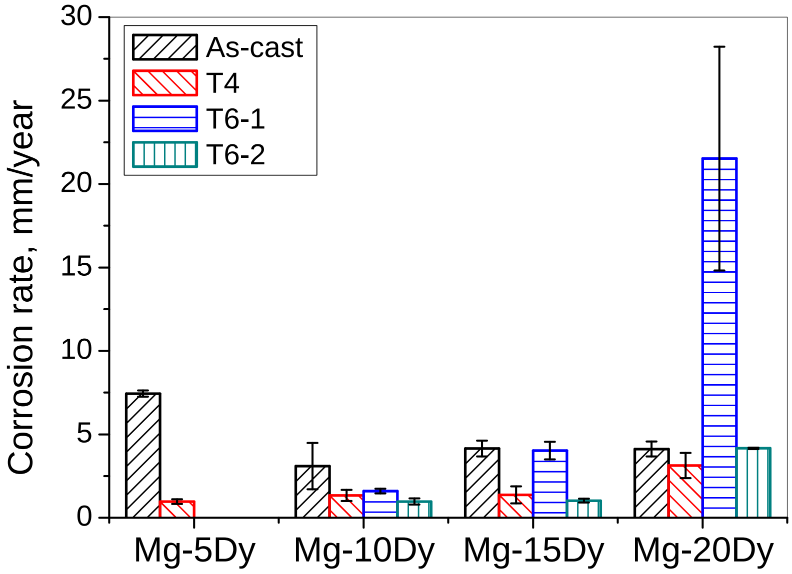

Fig. 30: Corrosion rates of Mg-Dy alloys after 72h immersion in 0.9wt.% NaCl solution at room temperature.

Fig. 30 shows the corrosion rate of Mg-Dy alloys in 0.9 wt.% NaCl solution at room temperature. In the as-cast condition the Mg-10Dy alloy shows the lowest corrosion rate at 3 mm/year compared with Mg-5Dy alloy at 7.5 mm/year. At Dy concentration higher than 10 wt% the corrosion rate increases again but do not reach the 7.5mm/year observed for the Mg-5Dy alloy. The corrosion rate is lower for the T4 treated alloy as compared with the as-cast condition. For example, the corrosion rate of Mg-5Dy alloy decreases from 7.5 mm/year to 0.9 mm/year after T4 treatment. The corrosion rate of Mg-10Dy and Mg-15Dy alloys is about 1.3 mm/year, which is slightly higher than that of Mg-5Dy alloy. In comparison, the Mg-20Dy alloy has a high corrosion rate at 3.1 mm/year after T4 treatment. After T6-1 treatment, the corrosion rate of Mg-10Dy alloy remains at the same as that of the T4 condition. However, the corrosion rate increases significantly for Mg-15Dy and Mg-20Dy alloys. For the Mg-20Dy alloy the corrosion rate increased to 21.5 mm/y, which is ~ 7 times that of the T4 treated alloy (3.1 mm/y). After T6-2 treatment, the corrosion rate of the Mg-20Dy alloy increased marginally from 3.1 to 4.1 mm/y. While the corrosion rate decreases slightly for Mg-10Dy and Mg-15Dy alloys following T6-2 heat treatment as compared with the T4 treated alloy.

5.1.4.2 Morphology after corrosion

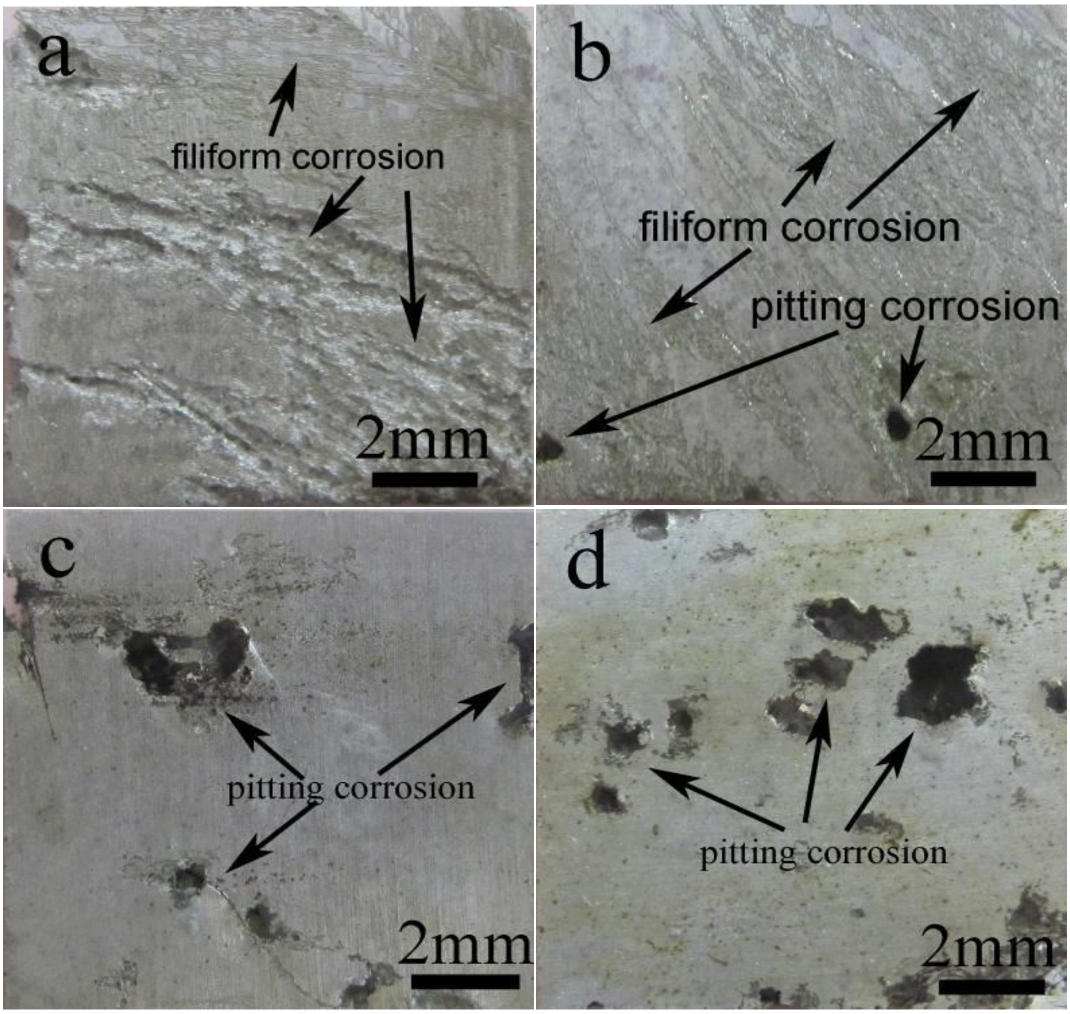

Fig. 31: Typical corrosion morphology of as-cast Mg-Dy alloys after 72h immersion in 0.9wt.% NaCl solution at room temperature, which were observed after removing the corrosion products: (a) Mg-5Dy alloy; (b) Mg-10Dy alloy; (c) Mg-15Dy alloy; (d) Mg-20Dy alloy.

The typical macro corrosion morphology of as-cast alloys is shown in Fig. 31. Apparent filiform corrosion occurs on the surface of the Mg-5Dy alloy after 72 h immersion testing (Fig. 31 (a)). The amount of filiform corrosion diminishes with an increased content of Dy. When the content of Dy is more than 15 wt.%, little filiform corrosion is observed (Fig. 31 (c, d)). With the increase of Dy the amount of pitting corrosion increases. Both the filiform and pitting corrosion lead to a high corrosion rate. As a result, the lowest corrosion rate is observed for the Mg-10Dy alloy due to the balance between the pitting and filiform corrosion.

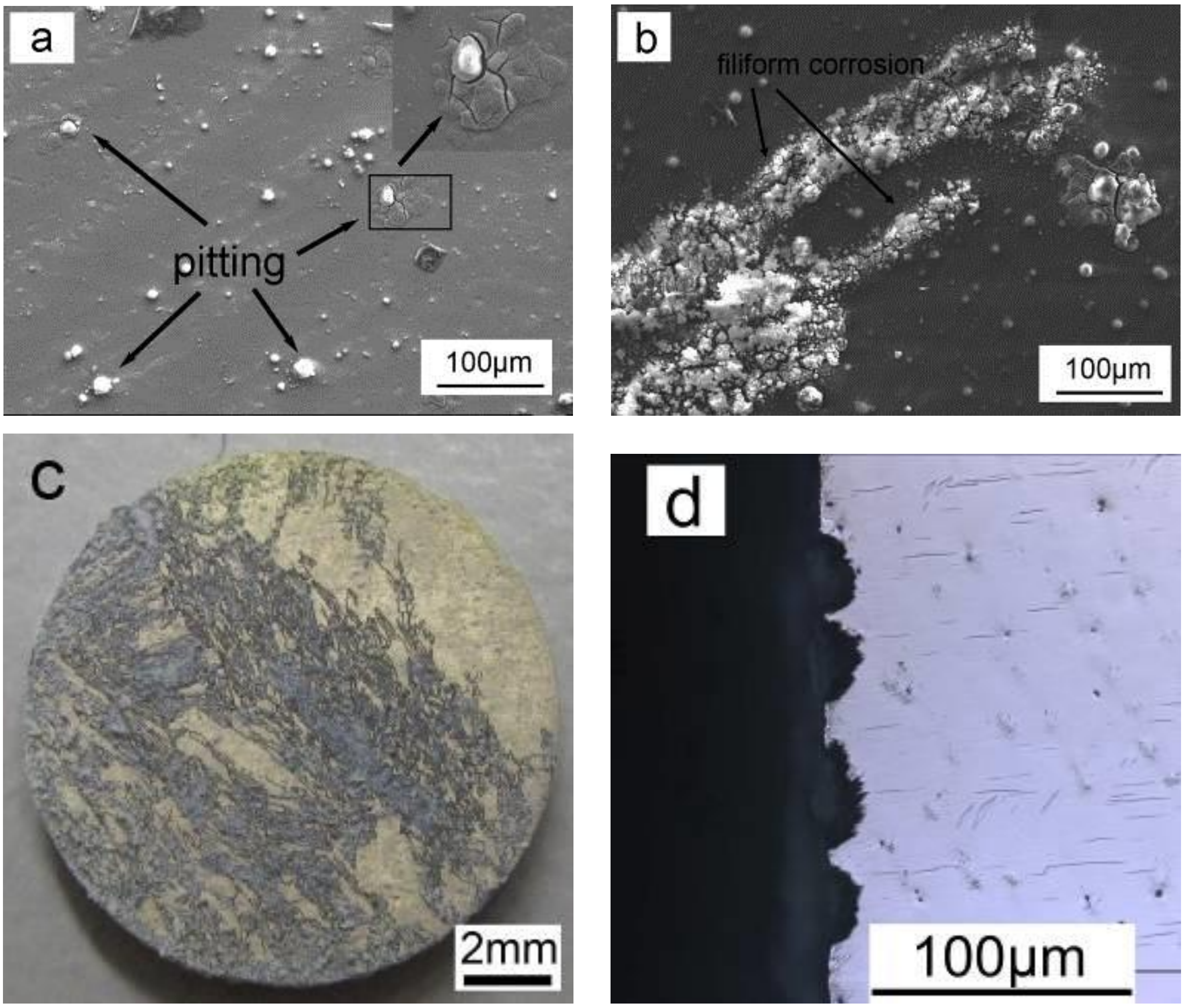

Fig. 32: Corrosion morphology of Mg-5Dy alloy after immersion in 0.9wt.% NaCl solution at room temperature: (a) SEM morphology after immersion for 30min; (b) SEM morphology after immersion for 3h; (c) optical image after immersion for 24h; (d) longitudinal cross-section morphology after immersion for 24h

To further understand the corrosion process, the corrosion morphology of Mg-5Dy and Mg-20Dy alloys was studied after different immersion time, (Fig. 32 and Fig. 33). For the Mg-5Dy alloy, the initial pitting corrosion occurs after immersion for 30 min, and then transforms to filiform corrosion over time (Fig. 32 (a, b)). After immersion for 24 h, the filiform corrosion spreads all over the surface (Fig. 32 d) and cross-sectional investigation showed that the corrosion reaches a depth of less than 20 µm (Fig. 32 d). For the Mg-20Dy alloy, the initiation of pitting corrosion is observed after immersion for 3 h (Fig. 33 a). After immersion for 24 h, apparent pitting corrosion (covered by corrosion products) can be seen clearly even by eye, but no filiform corrosion is observed for this alloy (Fig. 33 b). The cross-section of the corrosion morphology (Fig. 33 c) reveals the presence of severe pitting corrosion up to a depth of 100 µm.

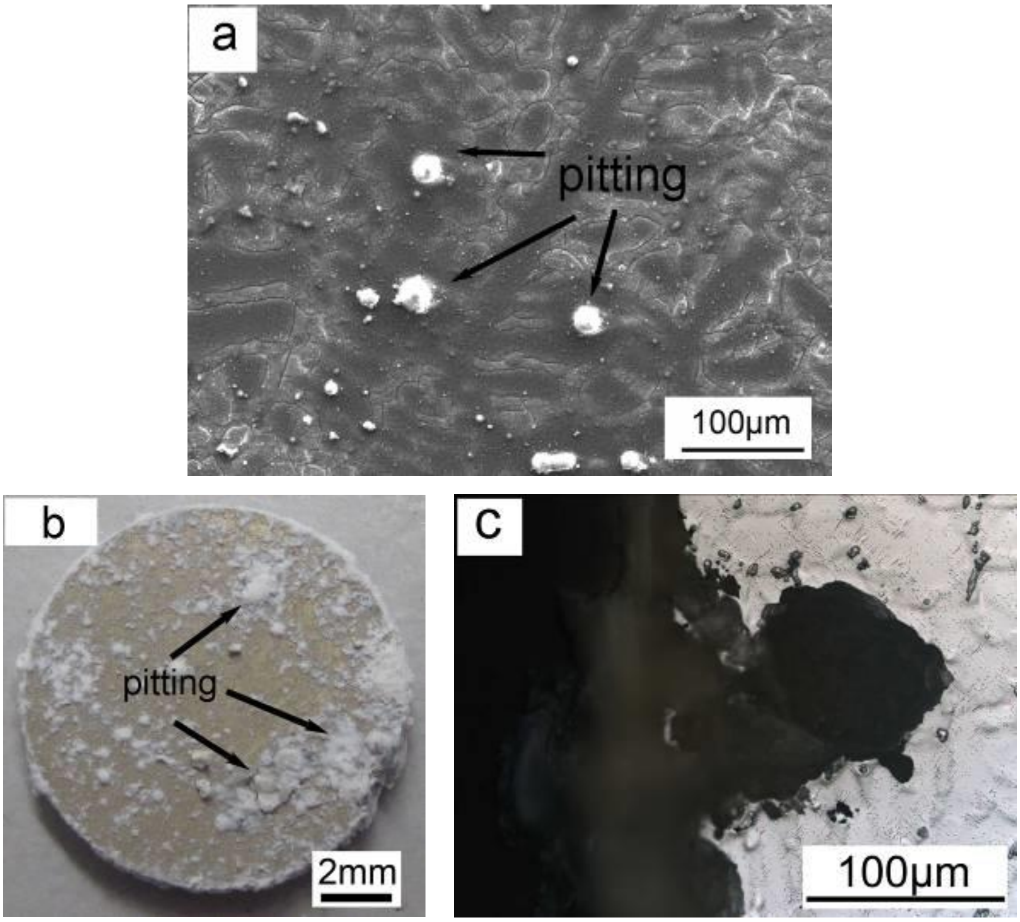

Fig. 33: Corrosion morphology of Mg-20Dy alloy after immersion in 0.9wt.% NaCl solution at room temperature. (a) SEM morphology after immersion for 3h; (b) optical image after immersion for 24h; (c) longitudinal cross-section morphology after immersion for 24h

After T4 treatment, the trend of corrosion morphology between filiform and pitting corrosion remains similar (Fig. 34). The filiform corrosion decreases while the pitting corrosion increases with the increase of Dy content. However, for a given alloy, both the pitting and filiform corrosion reduce after T4 treatment compared with the corrosion studies in the as-cast condition.

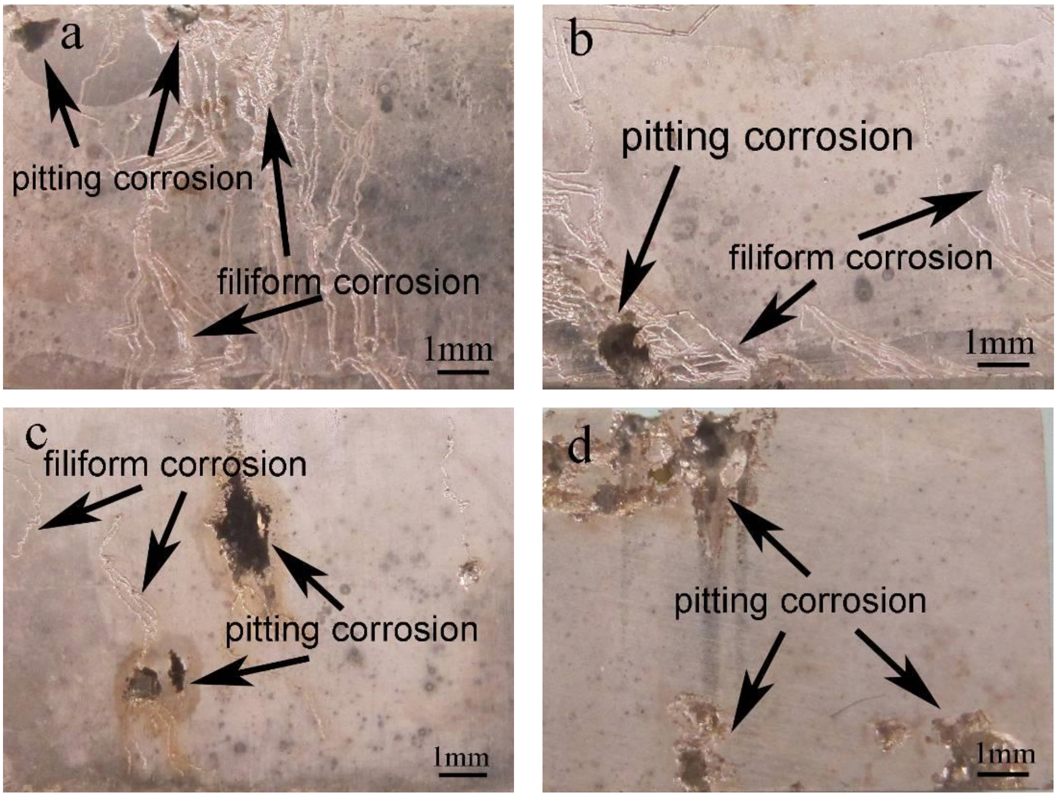

Fig. 34: Typical corrosion morphology of T4 treated Mg-Dy alloys after immersion for 72h in 0.9wt.% NaCl solution at room temperature (corrosion products have been removed): (a) Mg-5Dy alloy; (b) Mg-10Dy alloy; (c) Mg-15Dy alloy; (d) Mg-20Dy alloy.

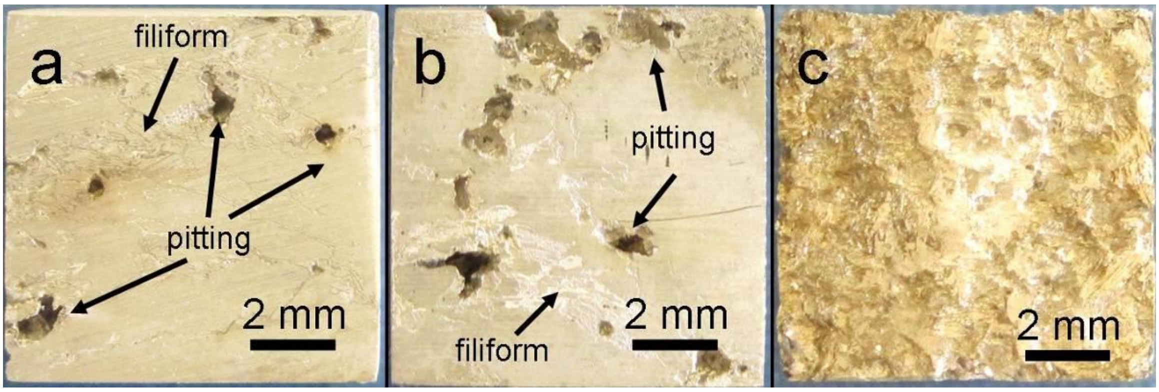

Fig. 35: Typical corrosion morphology of T6-1 treated Mg-Dy alloys after immersion for 72 h in 0.9wt.% NaCl solution at room temperature and removing corrosion products: (a) Mg-10Dy alloy; (b) Mg-15Dy alloy; (c) Mg-20Dy alloy.

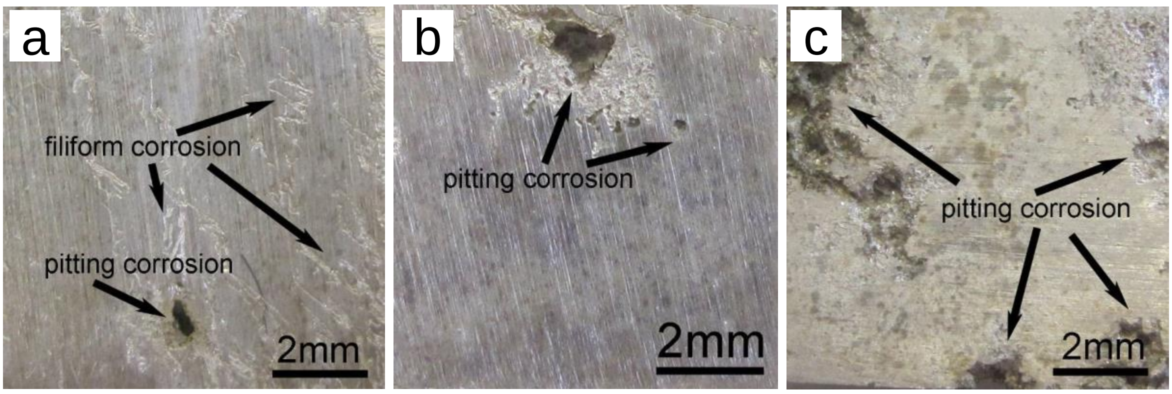

Fig. 36: Typical corrosion morphology of T6-2 treated Mg-Dy alloys after 72 h immersion in 0.9wt.% NaCl solution at room temperature and removing corrosion products: (a) Mg-10Dy alloy; (b) Mg-15Dy alloy; (c) Mg-20Dy alloy.

After the T6-1 treatment, the corrosion morphology remains unchanged for Mg-10Dy alloy, while the pitting corrosion increased for Mg-15Dy alloy. In the Mg-20Dy alloy severe pitting corrosion is observed following T6-1 heat treatment. The pits are interconnected and results in extensive corrosion. After the T6-2 treatment, the corrosion morphology of the investigated alloys is similar to those observed after the T4 heat treatment.

5.1.5 Corrosion in cell culture medium

5.1.5.1 Corrosion rate

The 0.9 wt% NaCl solution only provides a basic understanding of the corrosion behaviour of magnesium. In order to develop a magnesium alloy for biological applications this is not sufficient and the corrosion behaviour of Mg-Dy alloys was studied in CCM which has a close composition to that of human body fluid.

The corrosion rates of Mg-Dy alloys after immersion for 14 days in the CCM under cell culture conditions are shown in Fig. 37. In the as-cast condition, the corrosion rate is about 1 mm/y for Mg-5Dy alloy which decreased to ~ 0.8 mm/y for Mg-10Dy alloy. Further increase in the Dy content leads to an increase of the corrosion rate. After the T4 treatment, the corrosion rate of Mg-5Dy, Mg-10Dy and Mg-20Dy alloys remains unchanged from that of the as-cast values, but it reduces from 1.2 to 0.5 mm/y for Mg-15Dy alloy. After T6-1 and T6-2 treatment, the corrosion rates of all tested alloys are similar to the corrosion rates measured after T4 treatment.

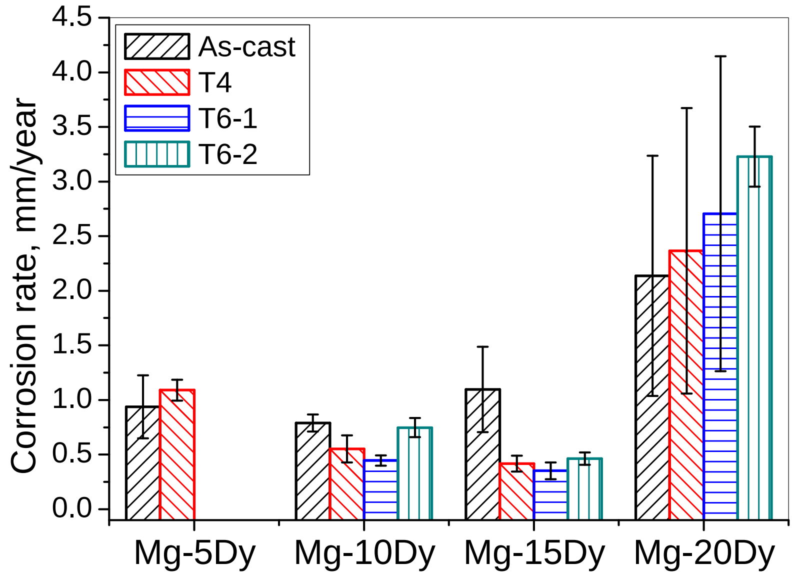

Fig. 37: Corrosion rates of Mg-Dy alloys after immersion for 14 days in CCM under cell culture conditions.

5.1.5.2 Morphology after corrosion

The macro corrosion morphology of the as cast Mg-Dy alloys after 14 days immersion in CCM under cell culture conditions can be seen in Fig. 38. Uniform corrosion is visible on the surface of Mg-5Dy alloy (Fig. 38 (a)), while localized corrosion occurs in the other alloys as indicated by arrows in Fig. 38 (b, c, d). The localized corrosion is increasingly severe with the increase of Dy amount.

In order to understand the influence of microstructure on the corrosion behaviour of Mg-Dy alloys, the microstructure of the as-cast Mg-Dy alloys and the corresponding corrosion morphology after 1 day immersion in CCM were investigated (Fig. 39). Most of the surface of the Mg-5Dy alloy is covered by very thick corrosion layer (dark colour) except for the few areas of Dy segregation (bright colour). With the increase of Dy, the areas covered by thick corrosion layer are reduced due to the increase of segregation areas of Dy. For example, only around half of the area is covered by the thick corrosion layer for Mg-20Dy alloy.

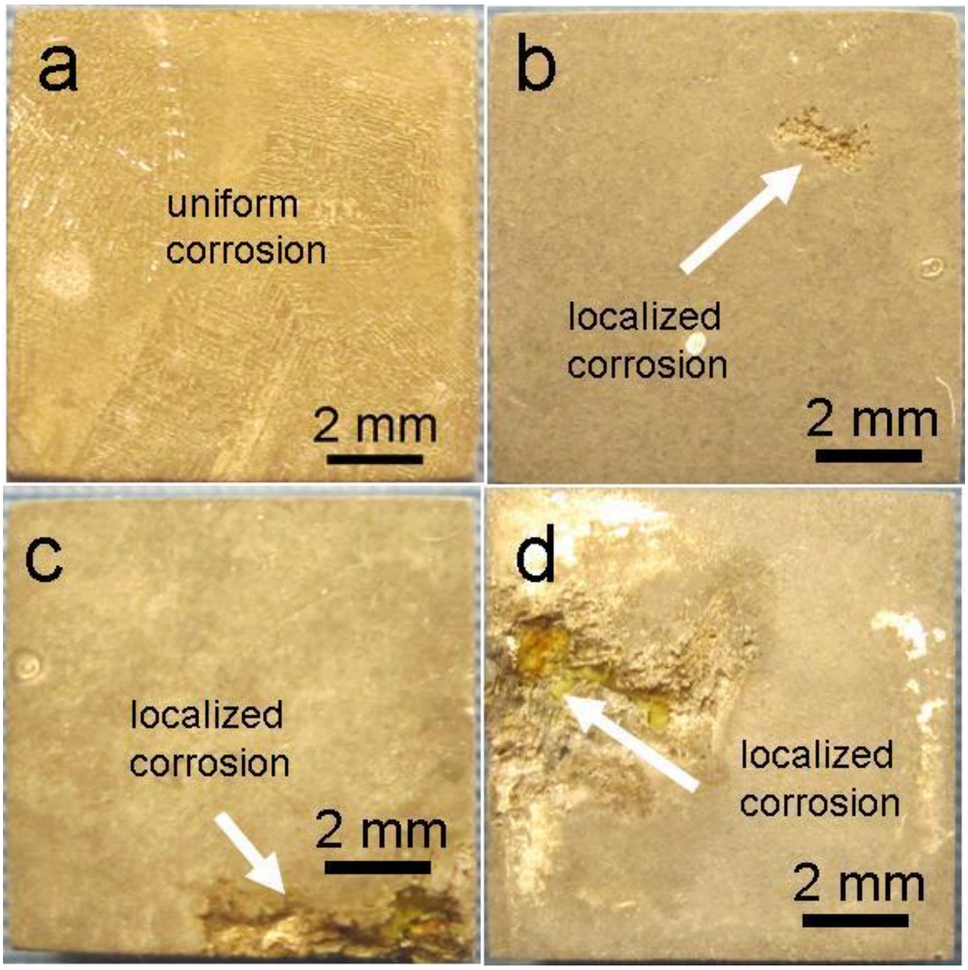

Fig. 38: Typical macro corrosion morphology of the as-cast Mg-Dy alloys after 14 days immersion in CCM under cell culture conditions (after removal of corrosion products): (a) Mg-5Dy alloy; (b) Mg-10Dy alloy; (c) Mg-15Dy alloy; (d) Mg-20Dy alloy.

The observations made from optical microstructure were further confirmed with SEM microstructural investigations (Fig. 40). The corroded surface is composed of dark and bright contrast regions. The dark regions correspond to the regions with bright contrast under optical microscopy. According to EDX analysis, the O content in the dark areas (as indicated by arrow A) is about 0.8 at.%, indicating marginal corrosion occurs in these areas. In the bright areas (as indicated by arrow B), about 16.79 at.% O was detected, indicating some corrosion has occurred in the bright areas and a corrosion film has formed. In addition, there are a large number of cracks formed in the corrosion layer during drying. Based on these results, it can be confirmed that the segregation of Dy leads to inhomogeneous corrosion of Mg-Dy alloys.

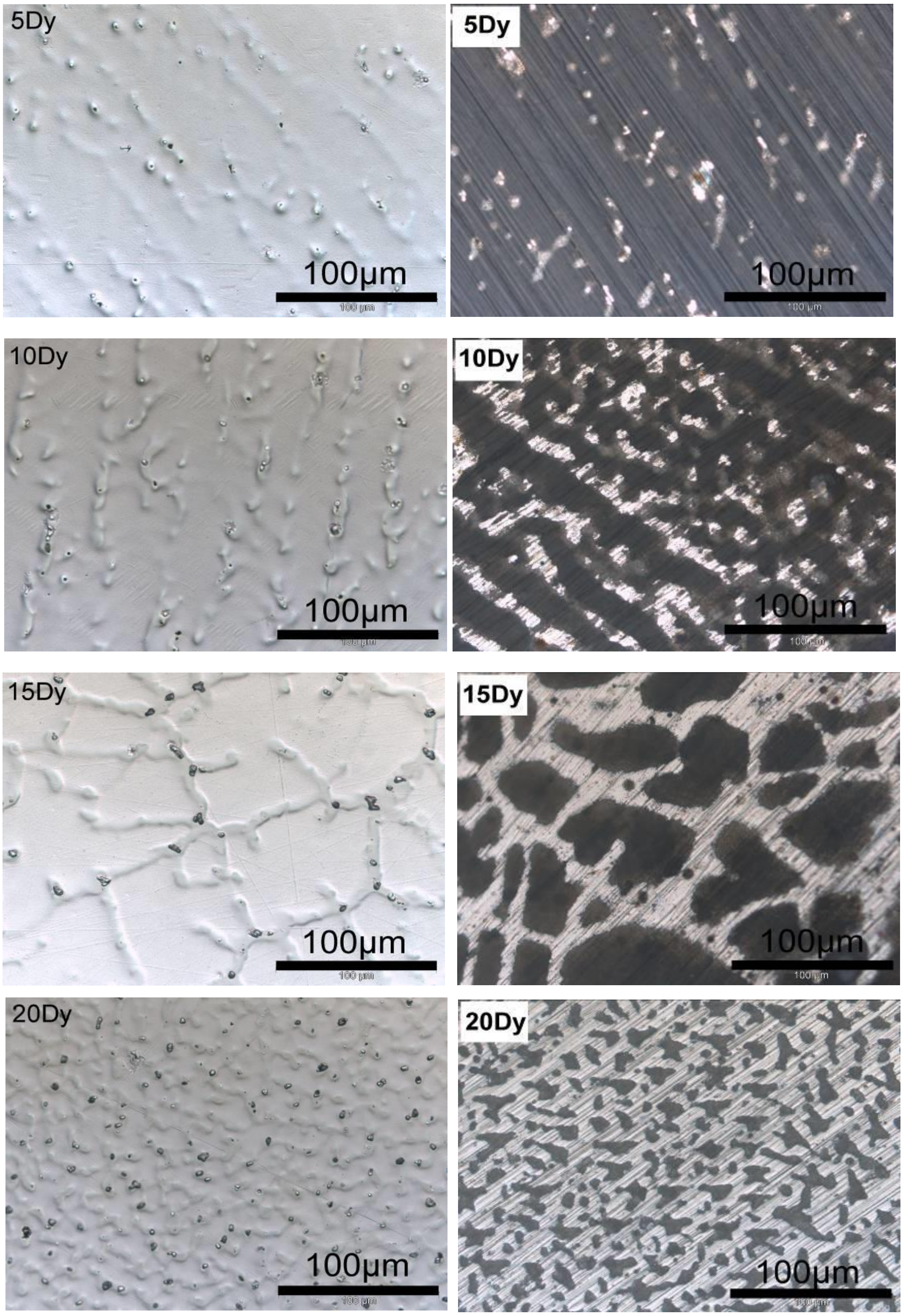

Fig. 39: Original microstructure of the as-cast Mg-Dy alloys (left) and their corresponding corrosion morphology (right) after 1 day immersion in CCM under cell culture conditions.

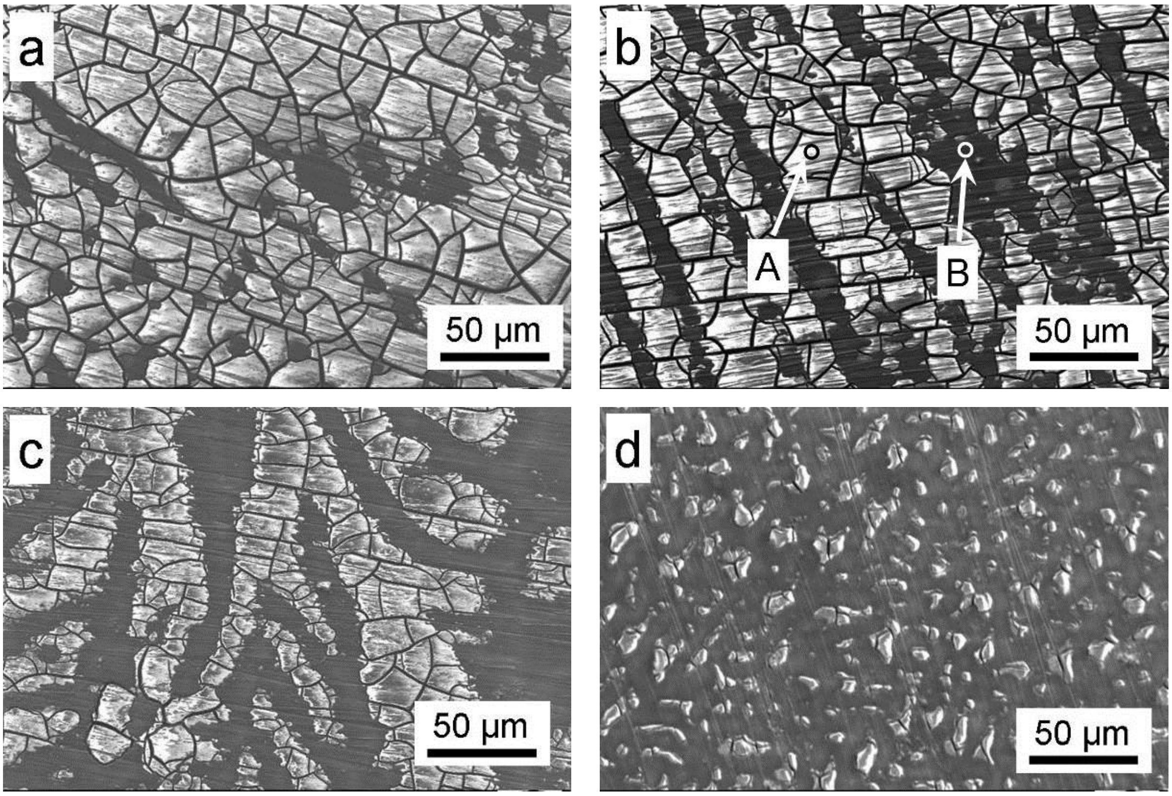

Fig. 40: SEM (secondary electron) morphology of corrosion layers for the as-cast Mg-Dy alloys after 1 day immersion: (a) Mg-5Dy alloy; (b) Mg-10Dy alloy; (c) Mg-15Dy alloy; (d) Mg-20Dy alloy.

The typical macro corrosion morphology of the T4 heat treated Mg-Dy alloys following 14 days immersion in CCM after removal of corrosion products are shown in Fig 39. Uniform corrosion occurs on the surface of Mg-5Dy and Mg-10Dy alloys. Unlike Mg-5Dy and Mg-10Dy alloys, the localized corrosion occurs on the surface of Mg-15Dy and Mg-20Dy alloys. Although the localized corrosion occurs on the alloys containing 15-20 wt% Dy, the corrosion resistance was improved with the increased Dy. The cross sectional structure of the corrosion layer after 3 days immersion is shown in Fig. 42. Increase in the Dy content reduces the thickness of the corrosion layer as indicated in Table 15. The thickness of corrosion layer decreases from ~14.6 µm to 9.4 µm as the Dy content increases from 5 to 10 wt.%, and falls below 2 µm for the Mg-20Dy alloy in regions away from the pitting corrosion (Fig. 42 (d)).

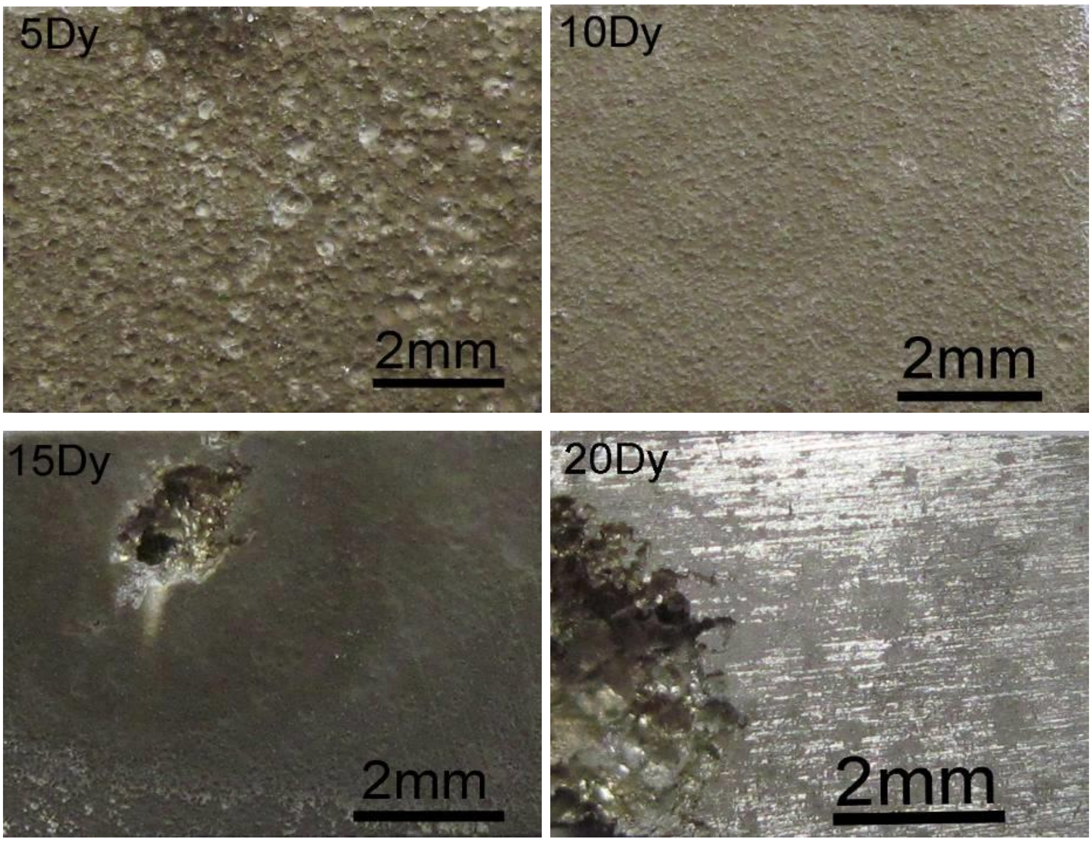

Fig. 41: Typical corrosion morphology of T4 heat treated Mg-Dy alloys after 14 days immersion in CCM under cell culture conditions (After the removal of corrosion products).

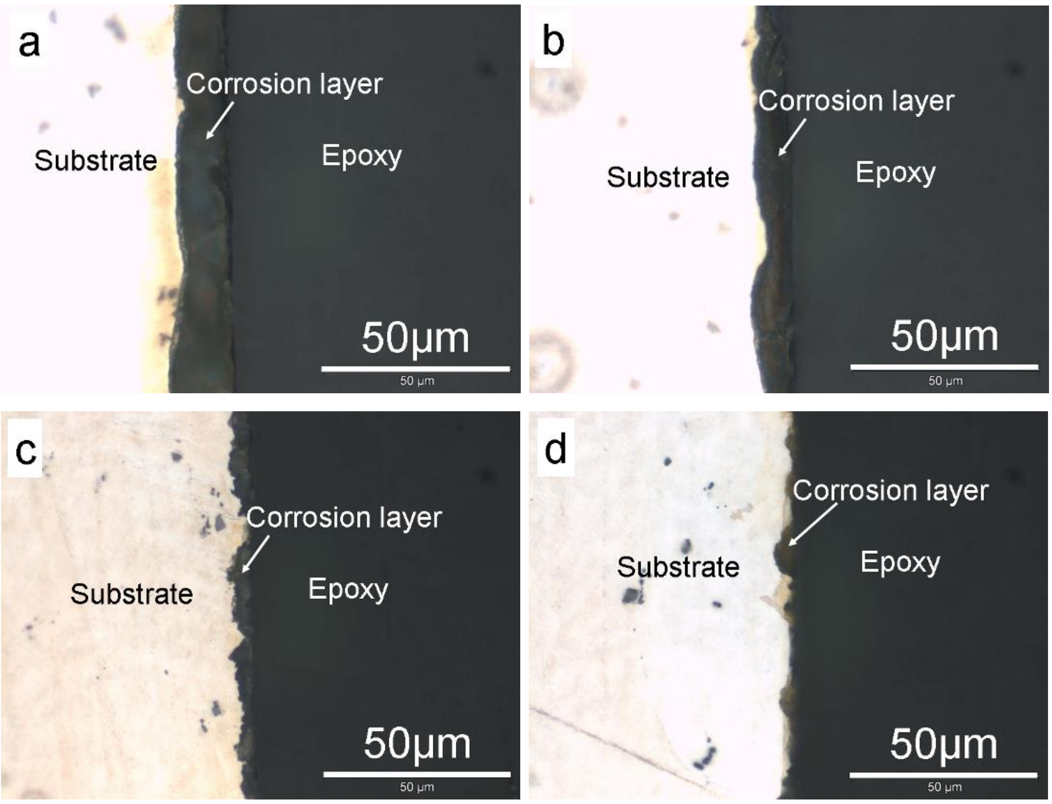

Fig. 42: Cross sectional morphology of T4 heat treated Mg-Dy alloys after 3 days immersion in CCM under cell culture conditions: (a) Mg-5Dy; (b) Mg-10Dy; (c) Mg-15Dy; (d) Mg-20Dy

Table 15: Thickness of corrosion layer after 3 days immersion in CCM under cell culture conditions

Alloys	Mg-5Dy	Mg-10Dy	Mg-15Dy	Mg-20Dy
Layer thickness (µm)	14.6±4.8	9.4±3.3	4.4±1.9	3.1±2.1

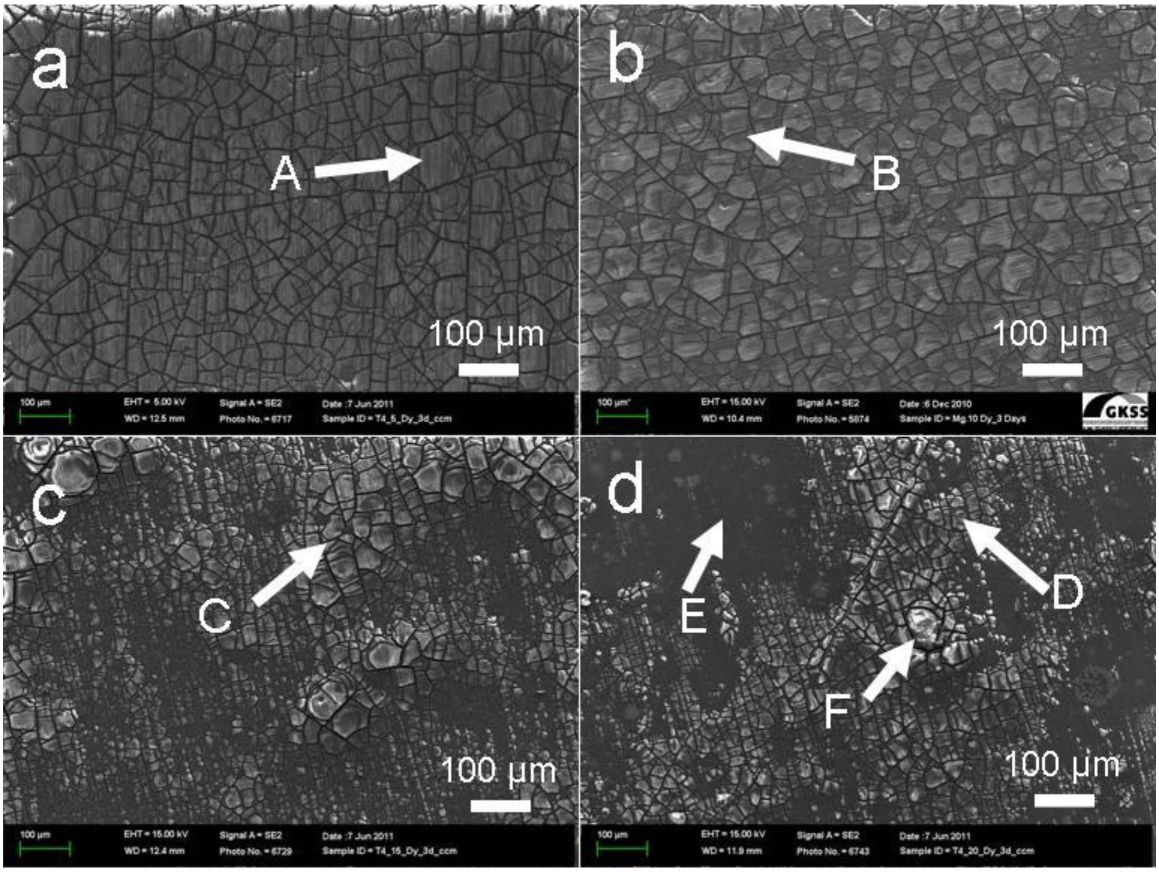

Fig. 43: Corrosion morphology of T4 heat treated Mg-Dy alloys after 3 days immersion in CCM under cell culture conditions: (a) Mg-5Dy; (b) Mg-10Dy; (c) Mg-15Dy; (d) Mg-20Dy

Fig. 43 shows the morphology of corrosion layer of T4 heat treated Mg-Dy alloys after 3 days immersion in CCM. The Mg-5Dy and Mg-10Dy alloys contained a very uniform corrosion layer while in the Mg-15Dy and Mg-20Dy alloys the corrosion layer is not uniform and the thickness of the corrosion layer varies. The Mg-20Dy alloy contained pitting corrosion (marked with arrow F) in addition to the uniform corrosion (Fig. 43 (d)). The composition of the corrosion layer analyzed by EDX is listed in Table 16. All alloys show Dy enrichment in the corrosion layer. The Dy content increased in the corrosion layer with the increase in Dy content of the alloys from 5 to 15 wt. % (point (A, B, C)). Following this trend the Dy content of the corrosion layer is expected to be higher for the Mg-20Dy alloy. However, due to the relatively thinner corrosion layer on Mg-20Dy alloy, some of the EDX signal comes from the substrate.

As a result, large amount of Mg is detected at point D and E 51.1 and 78.3 at.%, respectively, and correspondingly the detected Dy content is not as high as expected. In the areas subjected to pitting corrosion, a higher amount of C, P and Ca is detected, revealing the formation and accumulation of corrosion products (point F).

Table 16: Composition of corrosion layer analyzed by EDX for points shown in Fig. 43 (at.%).

	C	O	Mg	P	Ca	Dy
Point A	3.77	43.37	25.71	10.89	8.81	7.45
Point B	3.75	32.04	24.91	8.18	10.36	17.67
Point C	3.70	27.25	20.49	9.25	6.89	32.40
Point D	2.89	19.16	51.10	3.57	3.74	19.54
Point E	0	14.53	78.31	2.53	1.16	3.47
Point F	14.51	40.11	11.34	11.52	15.22	5.17

5.1.5.3 Corrosion layer characterization

Based on the above investigation, T4 heat treated Mg-10Dy alloy has the best combination of mechanical and corrosion properties. Therefore, this alloy was selected to conduct further investigations on the bio-corrosion layer formed in CCM.

The corrosion morphology of Mg-10Dy alloy after immersion for different time periods is shown in Fig. 44. Large number of cracks has formed on the surface of all samples due to dehydration during drying. After 1 day immersion, the surface of the sample is fully covered by a corrosion layer. Some pitting corrosion occurs at the places covered by locally piled corrosion products as indicated by arrows in (Fig. 44 (a)). The pitting corrosion is inhibited by the corrosion layer and does not develop into the regions of localized corrosion with further immersion (Fig. 44 (b)). After 11 days immersion, the morphology of the corrosion layer remains very uniform (Fig. 44 (c)).

Fig. 45 shows the thickness of the corrosion layer on the surface of T4 heat treated Mg-10Dy alloy as a function of immersion time. The thickness of corrosion layer increases with increasing immersion time and two different stages were observed. In stage I (up to immersion for 11 days), the growth rate of corrosion layer thickness reduces gradually with increase in immersion time. Then, in stage II (immersion for more than 11 days), the growth rate of corrosion layer thickness increases rapidly and remains unchanged and the corrosion layer thickness reaches ~ 75 µm after immersion for 28 days.

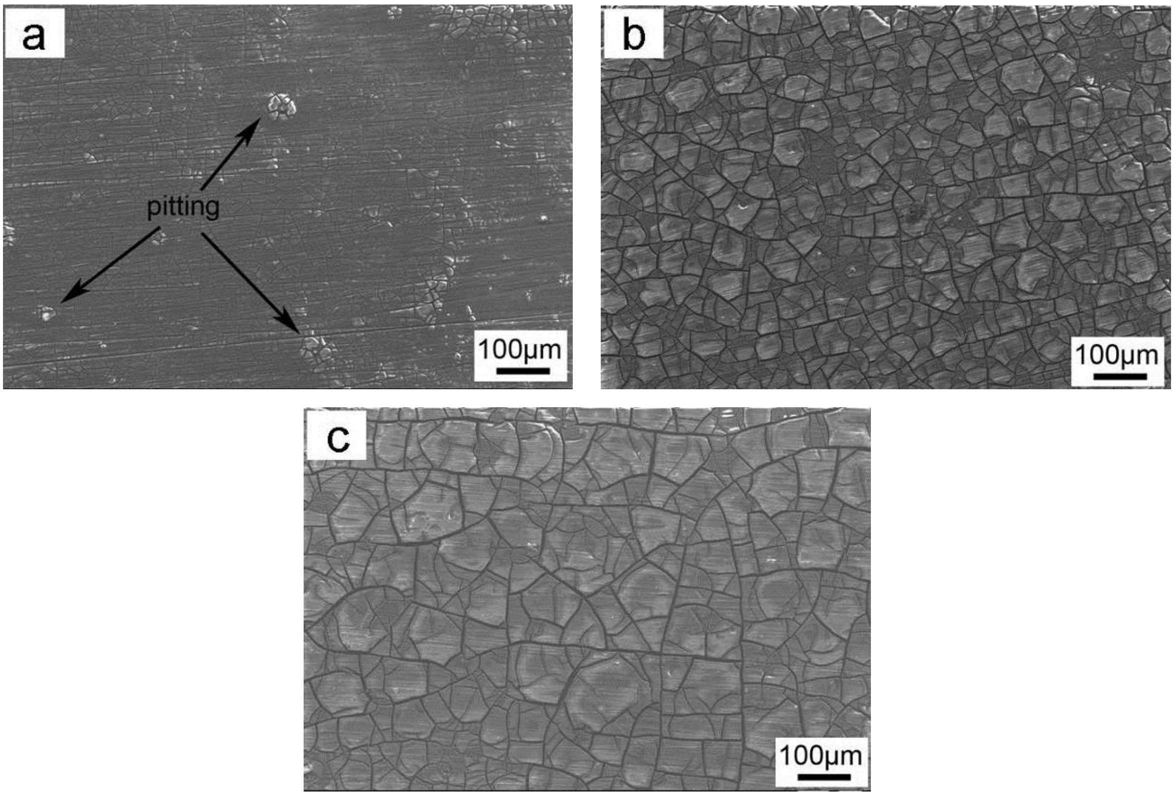

Fig. 44: Typical corrosion morphology of Mg-10Dy alloy after immersion for different time in CCM under cell culture conditions.

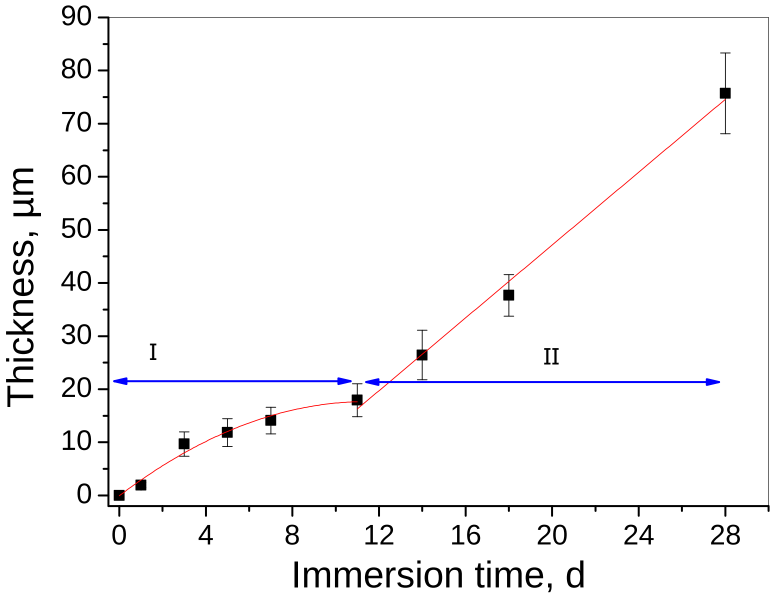

Fig. 45: Thickness of the corrosion layer on the T4 heat treated Mg-10Dy alloy as a function of immersion time in CCM under cell culture conditions.

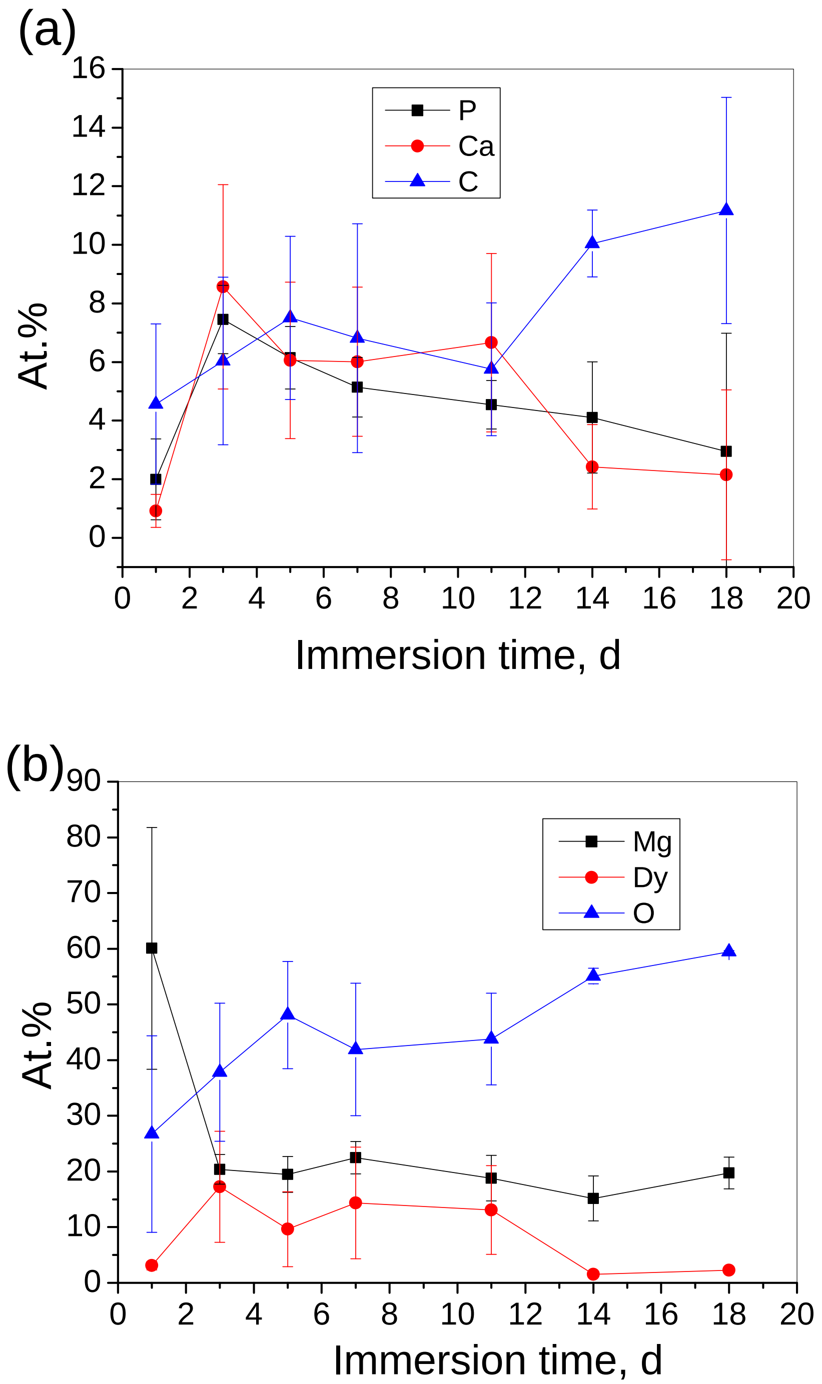

Fig. 46: Distribution of main elements in the surface of corrosion layer analyzed by EDX.

The distribution of the main elements in the surface of the corrosion layer is shown in Fig. 46. After immersion for 1 day, majority of the signal collected by EDX is from the Mg substrate as the corrosion layer is very thin (about 2 µm as shown in Fig. 45). As a result, the composition of the corrosion layer analyzed by EDX contains large amount of Mg (around 60 at.%) and only a small amounts of other elements such as P and Ca. When the immersion time is between 3 and 11 days, the contents of all the main elements (Mg, Dy, O, C, P and Ca) remain at the same level on the surface of corrosion layer although the thickness of corrosion layer increases. The Dy is enriched (around 12 at.%) at the surface of the corrosion layer, which is ~ 7 times higher than that contained in the alloy (1.6 at.%). When the immersion time exceeds 14 days, the contents of P, Ca and Dy reduce while the contents of C and O increased in the corrosion layer.

Both the surface and cross-section morphology of the corrosion layer are shown in Fig. 47. In order to analyze the corrosion layer in detail focused ion beam (FIB) was used to cut the corrosion layer. Platinum was deposited on to the surface of corrosion layer to prevent damage to the corrosion product from FIB (Fig. 47 (a)). On the top of the cross-section of the corrosion layer, the deposited platinum is clearly visible (Fig. 47 (b)). The thickness of the corrosion layer is ~ 7.5 µm, which is consistent with the results shown in Fig. 45. Some cavities are observed at the interface between the corrosion layer and substrate (Fig. 47 (c). These cavities are likely to have formed during the dehydration. During drying, the volume of the corrosion layer reduces, but the substrate remains unchanged. Therefore, this mismatch at the interface is likely to cause the cavities.

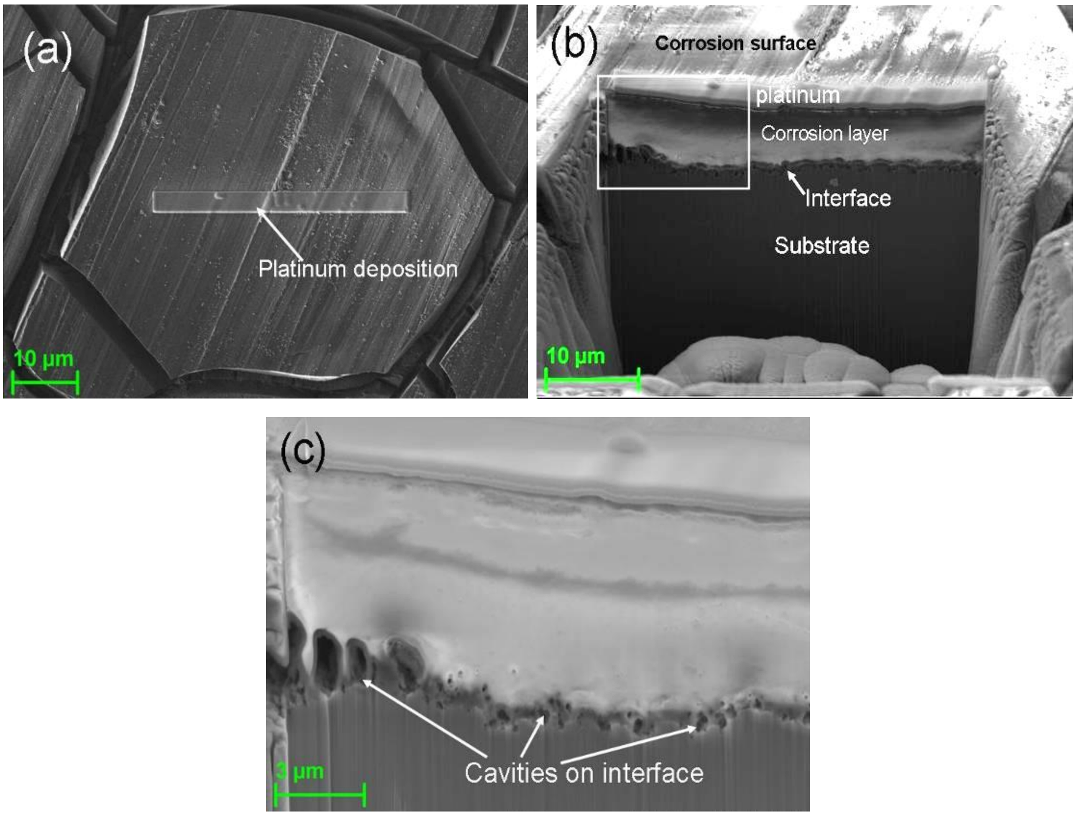

Fig. 47: SEM pictures showing the surface and cross-section morphology of corrosion layer after immersion for 3 days: (a) cutting position on the surface; (b) cross-section, low magnification; (c) cross-section, high magnification.

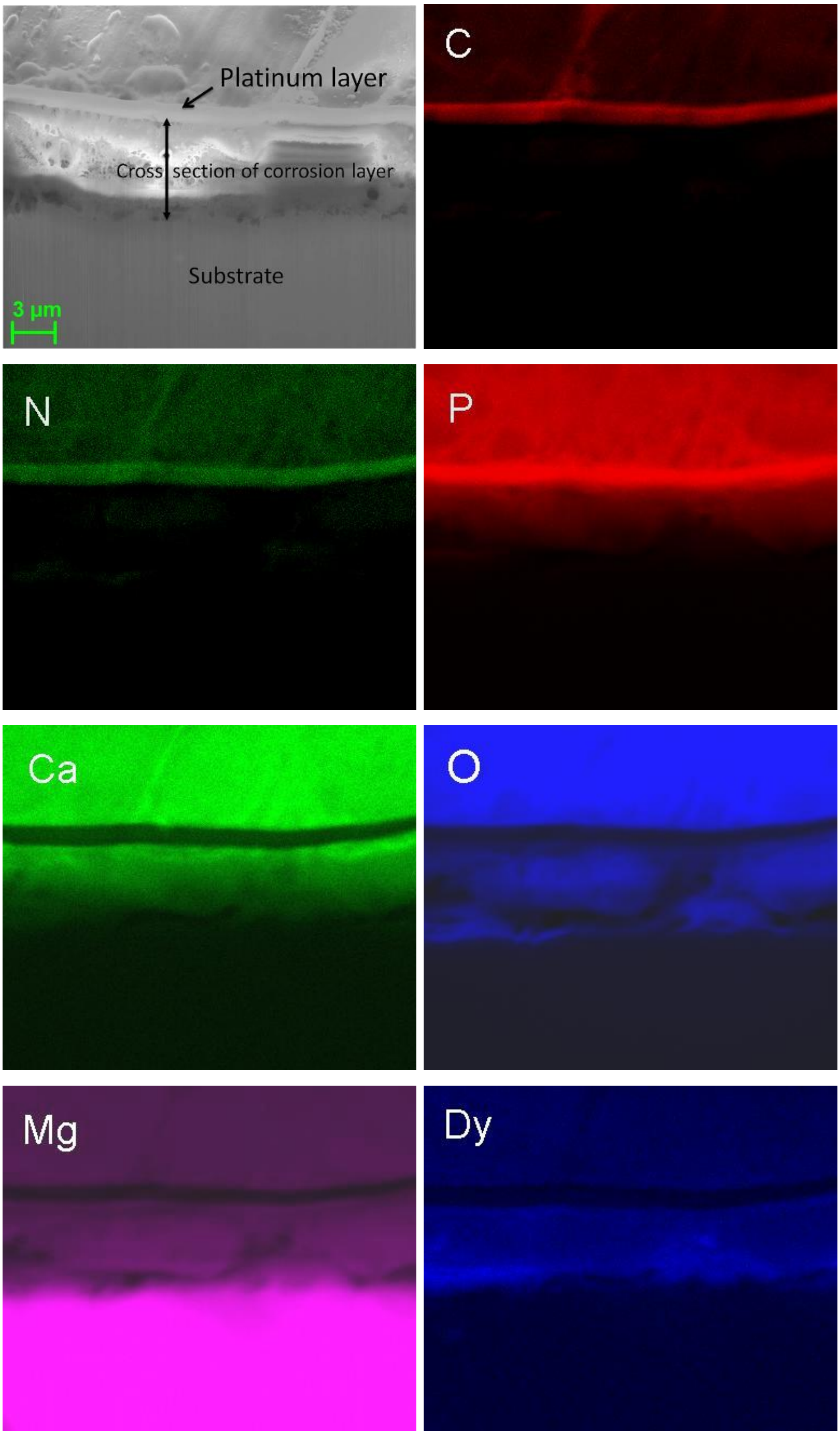

Fig. 48: Distribution of elements in the corrosion layer (EDX mapping).

The EDX map showing the distribution of elements in the corrosion layer is shown in Fig. 48. N and C distribute mainly on the surface of corrosion layer. On the Pt deposition area, it seems N and C content is higher, which could be due to the interference of Pt information rather than a fact. The amount of P and Ca at the surface of corrosion layer is higher than that near the interface. Very high intensity of P is detected in the Pt deposition area due to the overlap of the EDS binding energy of P and Pt. Mg distributes homogeneously in the corrosion layer. Dy is found in the whole corrosion layer. The intensity of Dy in the corrosion layer is much higher than that in the Mg substrate. In order to further understand the distribution of elements in the corrosion layer, EDX line scanning was conducted (Fig. 49). The line scanning starts from A and ends at B for the corrosion layer as indicated in Fig. 49 (a). The line segment before A is the platinum layer deposited on the samples and the segment after B is Mg-10Dy alloy substrate. The C and N contents are very high on the surface of corrosion layer and reduce dramatically inside the corrosion layer. The O content distributes homogeneously inside the corrosion layer, but it increases at the interface between the corrosion layer and Mg matrix. This indicates that some oxygen driven corrosion process could happen. Mg is distributed homogeneously in the corrosion layer while Dy is enriched in the corrosion layer compared with the magnesium matrix. Both P and Ca content reduce gradually from the surface of corrosion layer to the interface between Mg and corrosion layer.

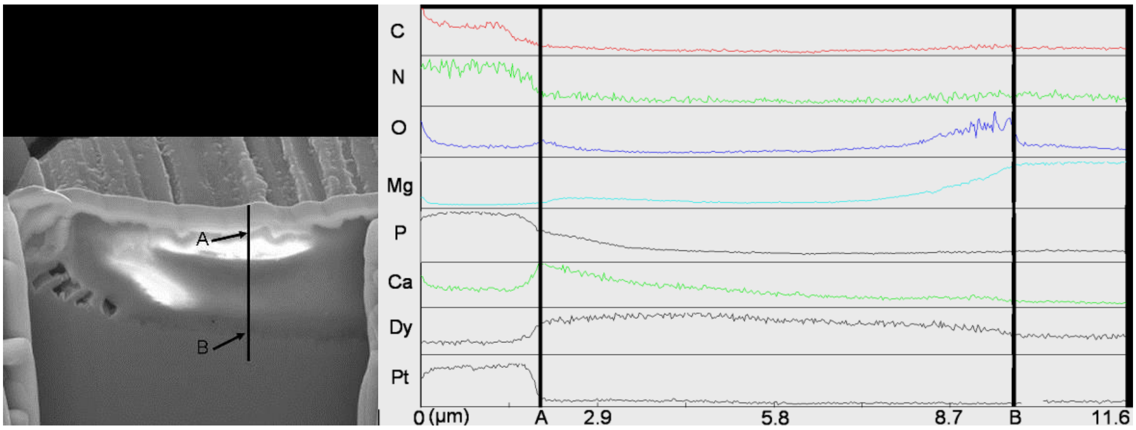

Fig. 49: Distribution of elements in the corrosion layer analyzed by EDX line scanning.

In Fig. 50 and Fig. 51, the XPS results are presented in the form of elemental depth profiles. The XPS results were recorded for sputtering times of 0-5000 s and after 5000 s sputtering the XPS peaks detected changes both in intensity and types, suggesting that the alloy substrate is reached. The peak detected after 5000 s sputtering at the binding energy for the Ca (2p) is from the Mg (auger KLL) due to the magnesium alloy rather than from Ca. Peaks of C and N were identified on the surface of corrosion layer and these decrease significantly after sputtering for 1000 s and no C and N peaks were detected. Both Dy and Mg peaks show similar intensities through the corrosion layer. The nature of Dy peak changes after 5000 s sputtering as the alloy substrate is reached. The peak intensities of the P and Ca reduce from the surface of corrosion layer to the interface between corrosion layer and the Mg alloy. The XPS results are consistent with that obtained through EDX line scanning and mapping. The O peak changes its shape depending on the sputtering time (Fig. 51). This is due to overlapping of three different peaks containing O. These peaks can be fitted to belong to O^{2-}, OH^{-} and PO_4^{3-}.

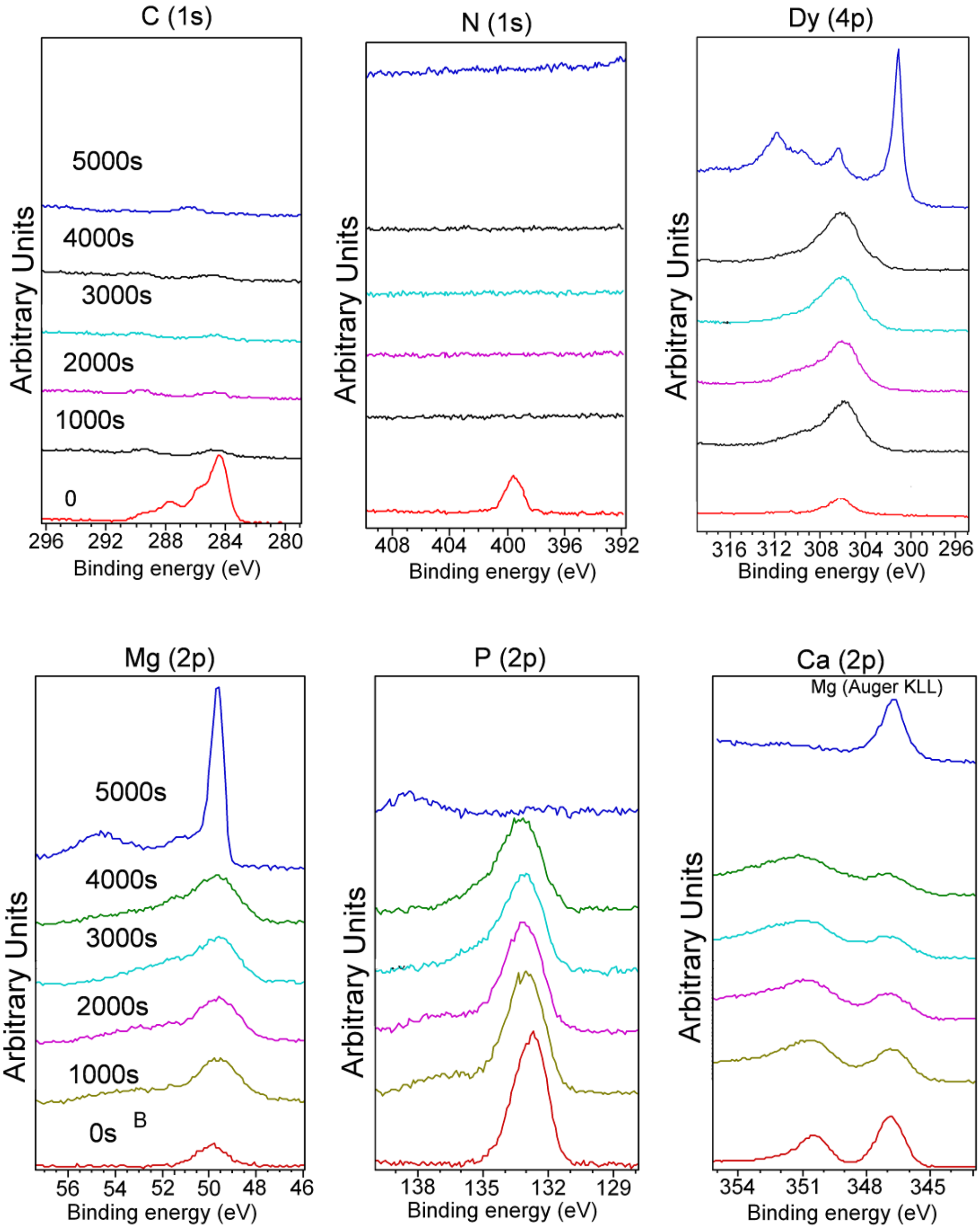

Fig. 50: Distribution of C, N, Dy, Mg, P, and Ca in the corrosion layer analyzed by XPS.

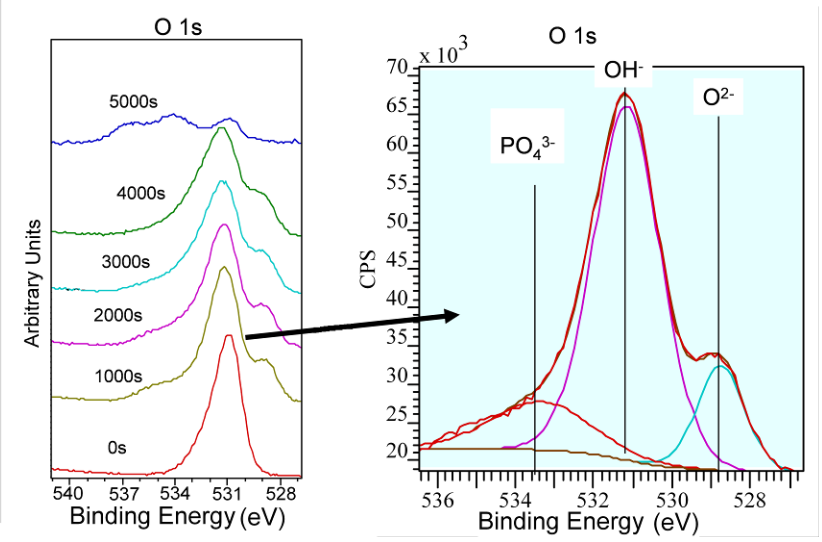

Fig. 51: Distribution of O element in the corrosion layer analyzed by XPS.

Both of Mg and Dy are present in the Mg-10Dy alloy, as a result it is very difficult to identify the chemical state of Dy in the corrosion products. To investigate the chemical state of Dy in the corrosion layer, the XPS analysis was carried out on the surface of pure Dy metal after immersion in the CCM for 1 day (Fig. 52). The O 1s peak is split into two clear broad peaks (b). At lower binding energy, peak position of the O 1s peak is identified at BE=528.8 eV, corresponding to Dy-O bonding of Dy_2O_3. At higher binding energy, the peak position of the O 1s peak is observed at BE=531.3 eV, corresponding to Dy-OH binding of $Dy(OH)_3$. Therefore, the Dy-containing corrosion products on pure Dy are a mixture of Dy_2O_3 and $Dy(OH)_3$.

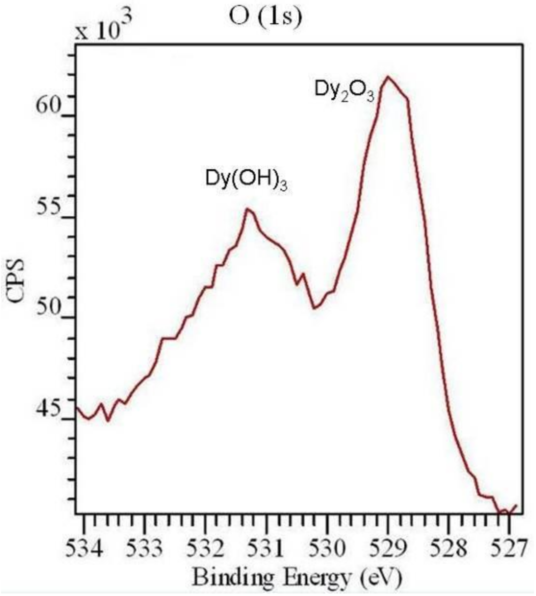

Fig. 52: XPS result of pure Dy metal immersed in CCM for 1 day (after 100 s sputtering).

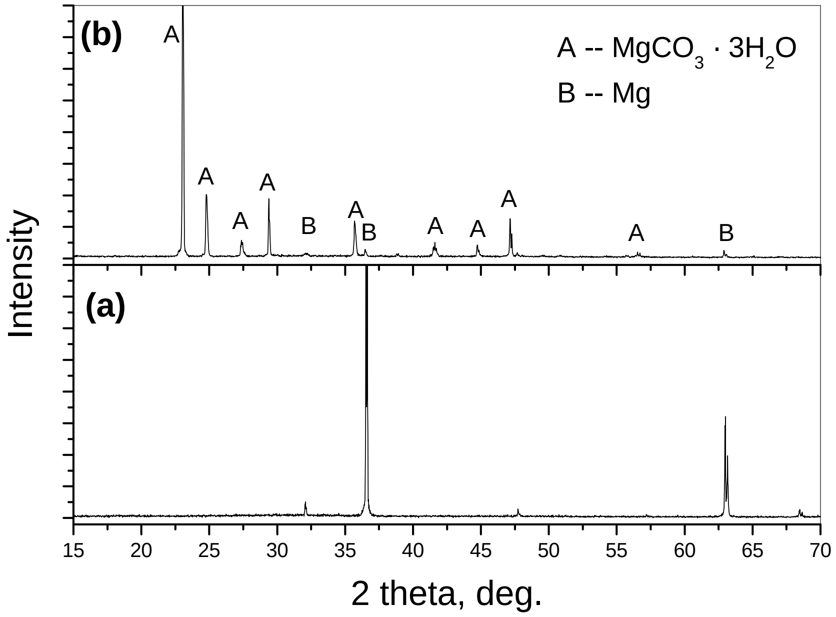

Fig. 53: XRD patterns of corrosion layer after immersion for: (a) 14 days and (b) 28 days.

Fig. 53 shows the XRD patterns of the corrosion layer after immersion for 14 days and 28 days. After immersion for 14 days, only pure Mg is identified in the XRD profile indicating a very thin corrosion layer which is penetrated by the X-ray (Fig. 53 (a)). As a result, most of the collected signals are from the Mg matrix. Following immersion for 28 days only few small peaks due to Mg was found, and main peaks were identified as $MgCO_3 \cdot 3H_2O$ (Fig. 53 (b)).

5.1.6 Cytotoxicity evaluation

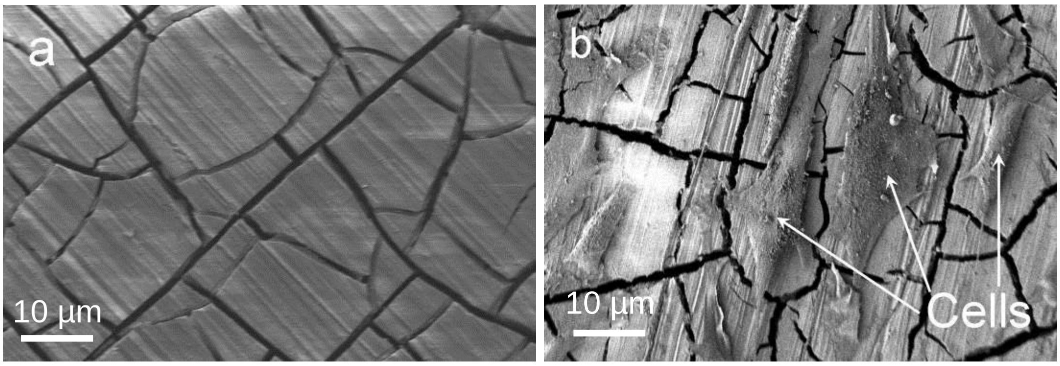

Fig. 54: (a) Morphology of bare corrosion layer; (b) Morphology of osteoblasts on corrosion layer

To illustrate the cell morphology on the corrosion layer, the morphology of corrosion layer without and with cells are shown in Fig. 54. For the bare corrosion layer, only some cracks are observed (Fig. 54 (a)). For the corrosion layer with cells on it, the irregular shape adhesions (as indicated by arrows) are osteoblasts.

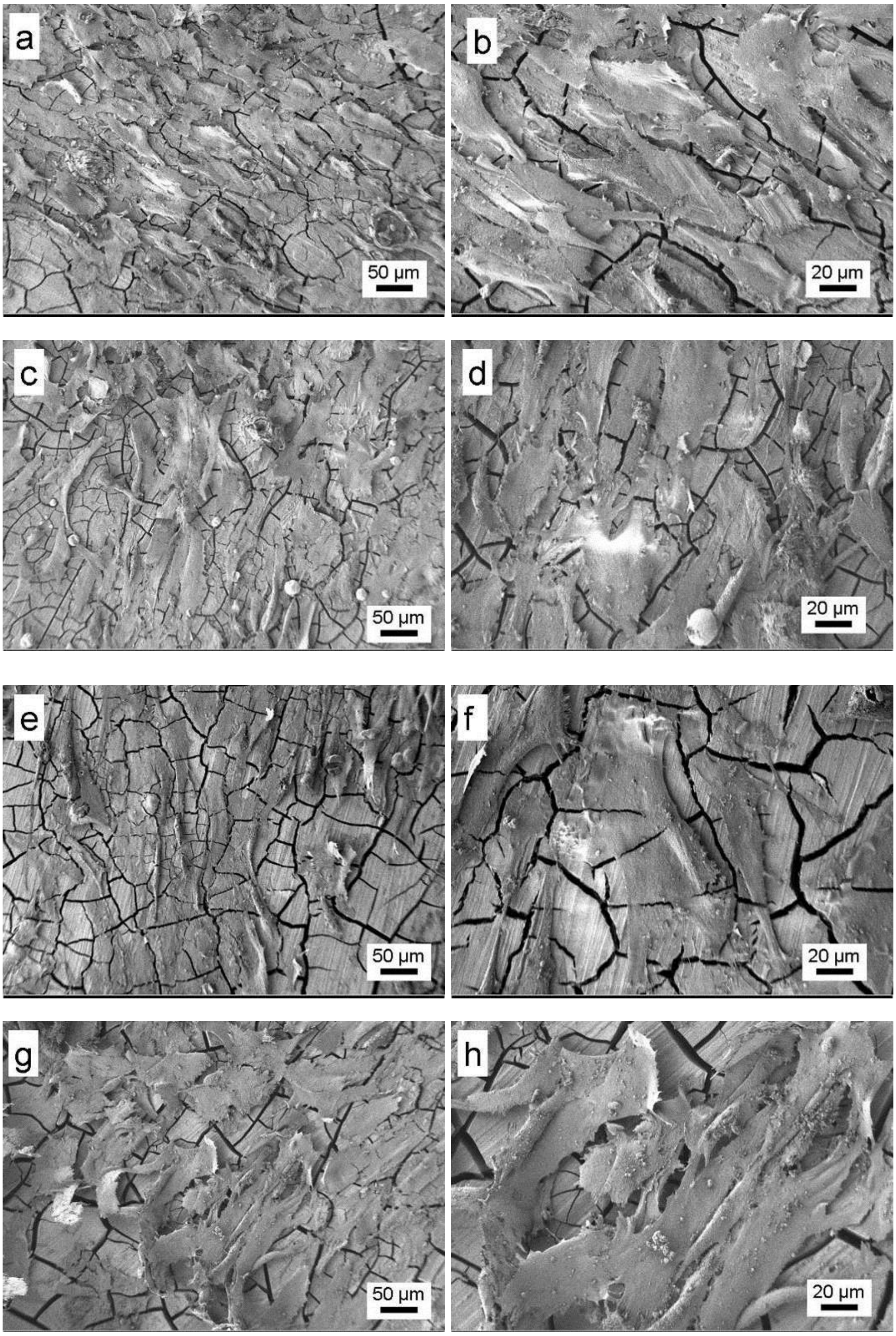

Fig. 55: Osteoblast morphology on the specimens after culture for 3 days and 7 days: (a, b) pure Mg after 3 days culture; (c, d) Mg-10Dy after 3 days culture; (e, f) pure Mg after 7 days culture; (g, h) Mg-10Dy after 7 days culture. Prior to cells seeding, specimens were pre-incubated in CCM for 2 h.

Fig. 55 shows the osteoblast morphology on the Mg-10Dy alloy after culture for 3 and

7 days. The purpose of this preliminary cytotoxicity study is to analyze the effect of Dy enrichment in the corrosion layer on the cell viability. Pure Mg was selected as a reference. After exposure for 3 days, a large number of cells were found on the surfaces of both pure Mg and Mg-10Dy (Fig. 55 (a, c)). The cells were well-spread and adhered to the surface on both pure Mg and Mg-10Dy (Fig. 55 (b, d)). After exposure for 7 days, no negative effect of Dy enrichment on cells was observed.

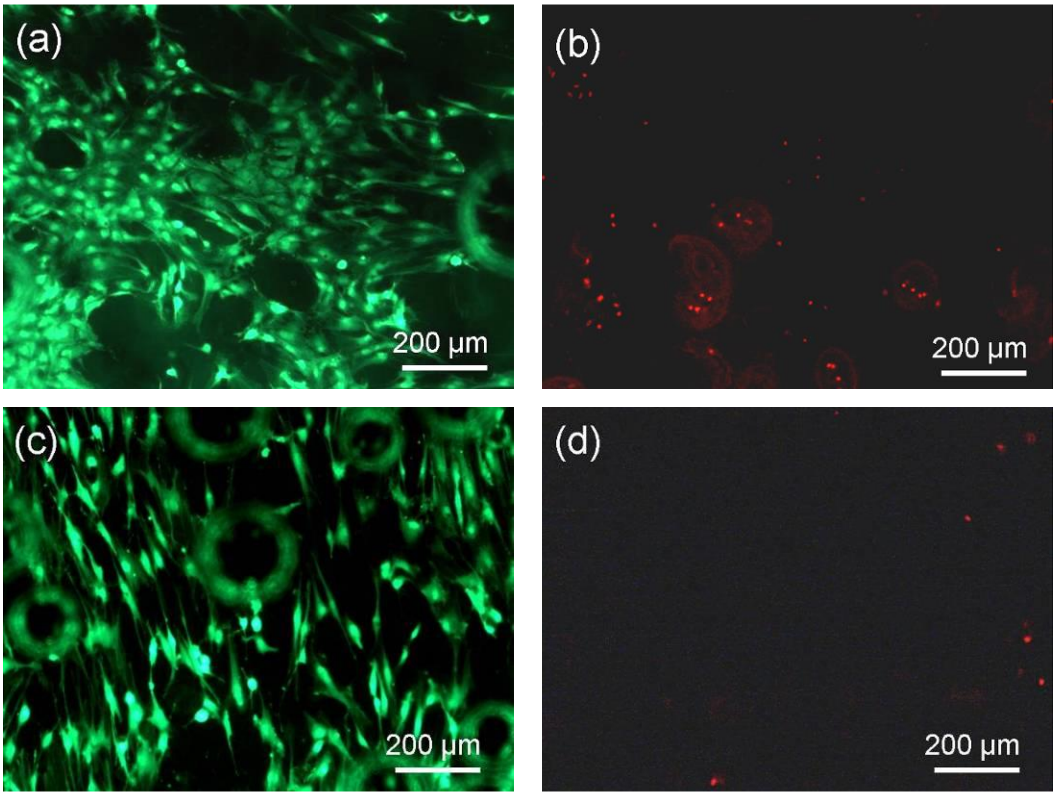

Fig. 56: Live (green) and dead (red) cells on pure Mg (a, b) and Mg-10Dy alloy (c, d) after culture for 3 days. Prior to the cells seeding, specimens were pre-incubated in CCM for 3 days. Images for live and dead cells were taken from the same position.

To further examine the cytotoxicity of the Dy-enriched corrosion layer on the cell viability, the corrosion layer was examined for live and dead cells by staining. The compositions of the corrosion layer is at stable state after immersion for 3 days in CCM thus the specimens were pre-incubated in CCM for 3 days prior to cell seeding. Fig. 56 and Fig. 57 show the live and dead cells on pure Mg and Mg-10Dy alloy after exposure for 3 and 7 days. Live and dead cells were stained green and red, respectively. A large number of live cells and only a few dead cells are observed on both the pure Mg and Mg-10Dy alloy after 3 days (Fig. 56). After 7 days, the number of dead cells remained very few in comparison with the number of live cells (Fig. 57).

Fig. 58 shows the quantification of cell viability on the pure Mg and Mg-10Dy alloy. After 3 days exposure, the viability is ~ 89% for cells on pure Mg and at higher value of 92% on Mg-10Dy alloy. After 7 days, the cell viability reaches to ~ 93% on both pure Mg and Mg-10Dy alloy. No cytotoxicity was observed for Mg-10Dy alloy where the corrosion layer was enriched with Dy.

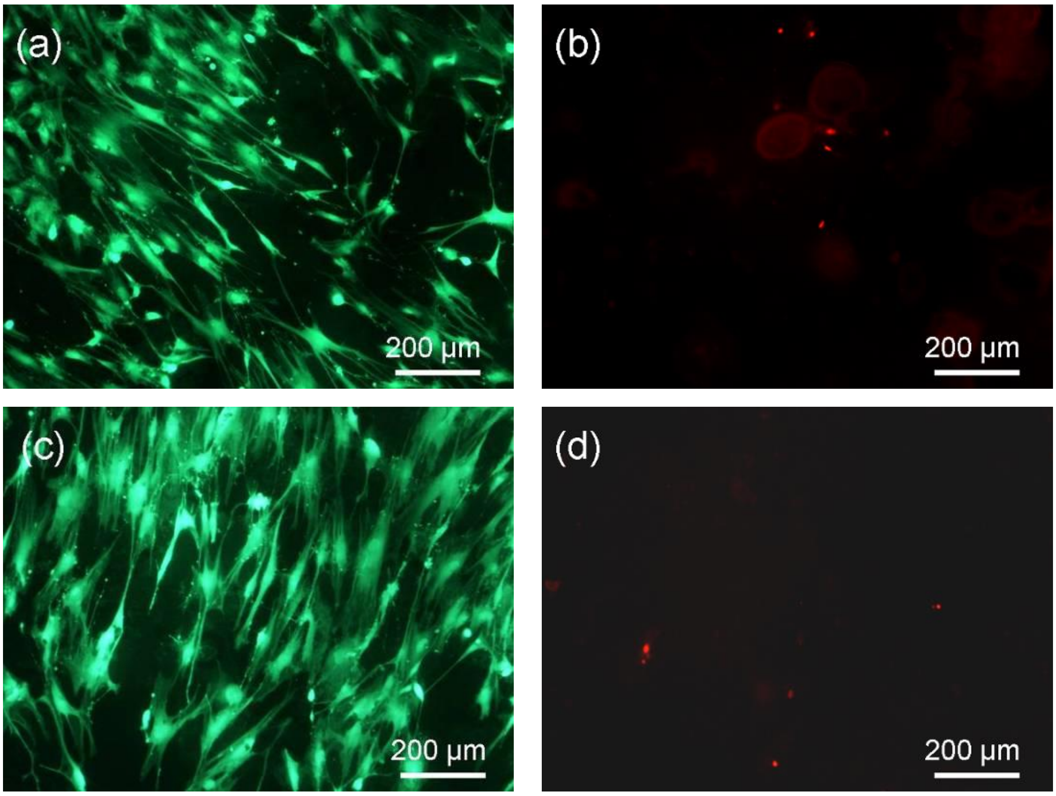

Fig. 57: Live (green) and dead (red) cells on pure Mg (a, b) and Mg-10Dy alloy (c, d) after culture for 7 days. Prior to the test, specimens were pre-incubated in CCM for 3 days. Images for live and dead cells were taken from the same location.

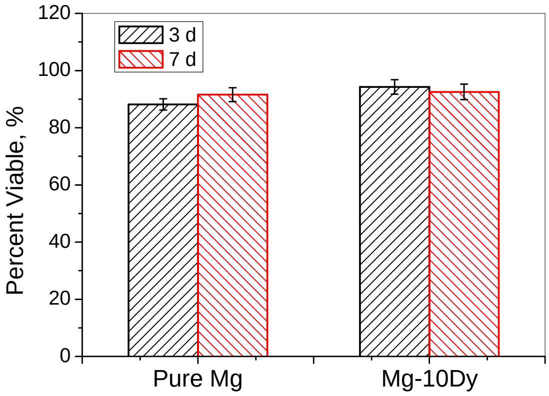

Fig. 58: Quantification of cell viability on pure Mg and Mg-10Dy alloys.

5.2 Mg-Dy-Gd-Zr alloys

Based on the above investigation on mechanical and corrosion properties of binary Mg-Dy alloys, the Mg-10Dy alloy is the best candidate for further study as a potential alloy for medical implants. However, the mechanical properties, such as yield strength and ductility of the Mg-10Dy alloy are not sufficient for medical applications. The Mg-10Dy alloy has very little age hardening response at 200°C, and the yield strength cannot be tailored through age hardening. It is necessary to further improve the yield strength and ductility of the Mg-10Dy alloy by alloying with additional elements but without the deterioration of corrosion resistance. Therefore, Mg-10wt.%RE-0.2Zr (RE=Dy+Gd) alloys were designed as Gd has better age hardening response at 200-250 ^{o}C compared with Dy. A small amount of Zr was added to these new alloys as a grain refiner to homogenize microstructure.

5.2.1 Chemical composition

Table 12 lists the actual compositions of Mg-Dy-Gd-Zr alloys. The loss of alloying elements Dy and Gd is ~ 10-20 wt.% for Gd and Dy. It is much higher for Zr with ~ 85 wt.% of the alloy additions lost during melting and casting. In comparison to the nominal compositions, the actual compositions of these alloys show a consistent loss in alloying additions.

Table 17: Actual chemical composition of experimental alloys (wt.%).

Alloys	Code	Dy	Gd	Zr	Fe	Ni	Cu	Mg
Mg-10Dy-0.2Zr	D10k	8.74	--	0.033	0.002	<0.004	0.004	Balance
Mg-8Dy-2Gd-0.2Zr	DG82K	7.08	1.57	0.037	0.002	<0.004	0.004	Balance
Mg-5Dy-5Gd-0.2Zr	DG55K	4.28	4.09	0.026	0.001	<0.004	0.004	Balance
Mg-2Dy-8Gd-0.2Zr	DG28K	1.60	7.24	0.030	0.003	<0.004	0.006	Balance

5.2.2 Microstructure characterizations

5.2.2.1 As cast microstructures

The macro structure of alloys horizontal and vertical to the casting direction is shown in Fig. 59 and Fig. 60, respectively. The macrostructure is very homogeneous in both the horizontal and vertical direction for all alloys, due to the grain refinement of Zr.

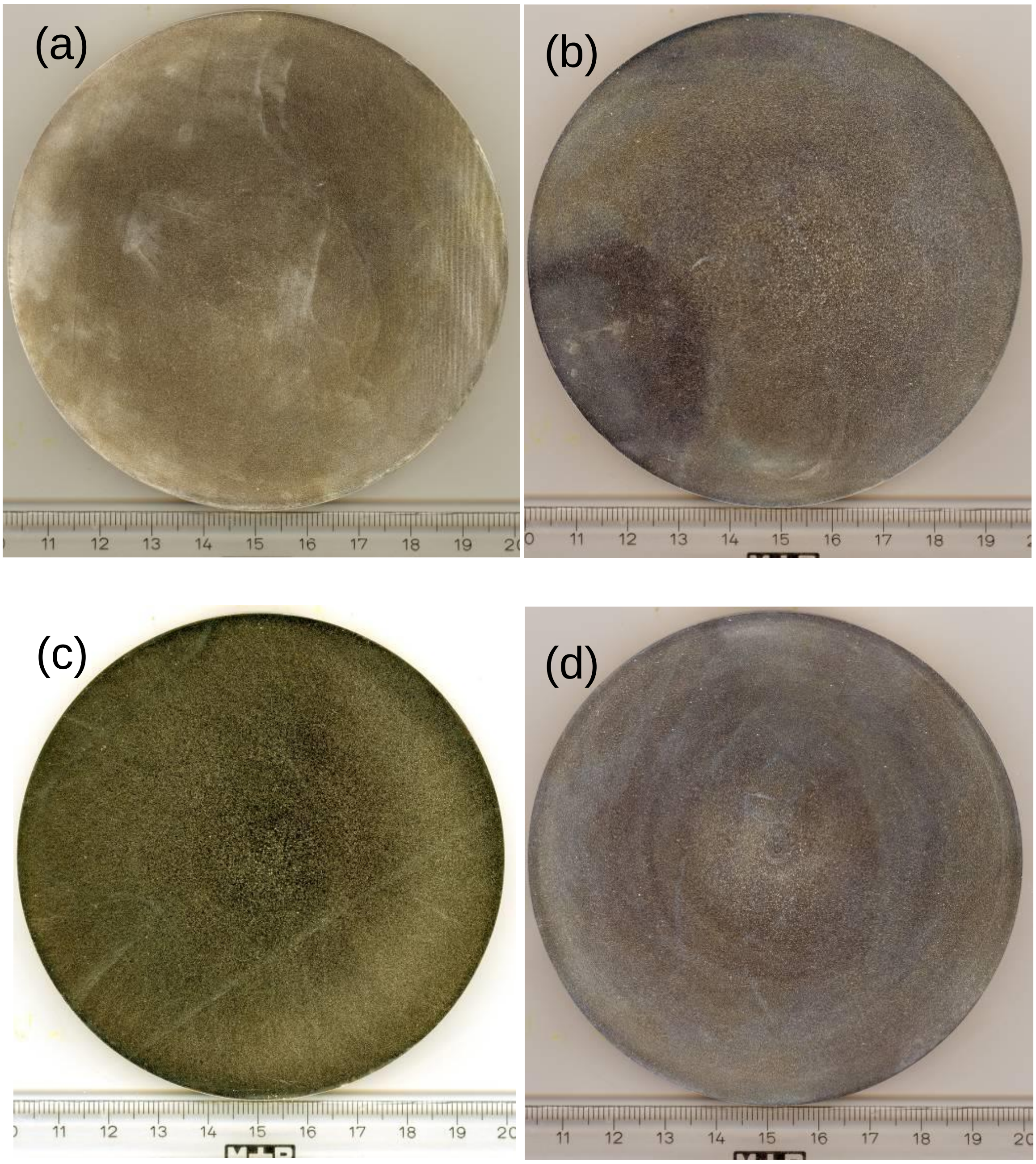

Fig. 59: Macro structure of the as-cast alloys in horizontal direction: (a) D10K; (b) DG82K; (c) DG55K; (d) DG28K. The unit of the scale is “cm”. The samples were cut from the middle part of the ingots.

Fig. 61 presents the optical microstructure of the as-cast alloys. An equi-axed grain structure was observed using optical microscopy, and the grain distribution is homogeneous. All the alloys have the similar grain size ~60 µm as shown in Fig. 62.

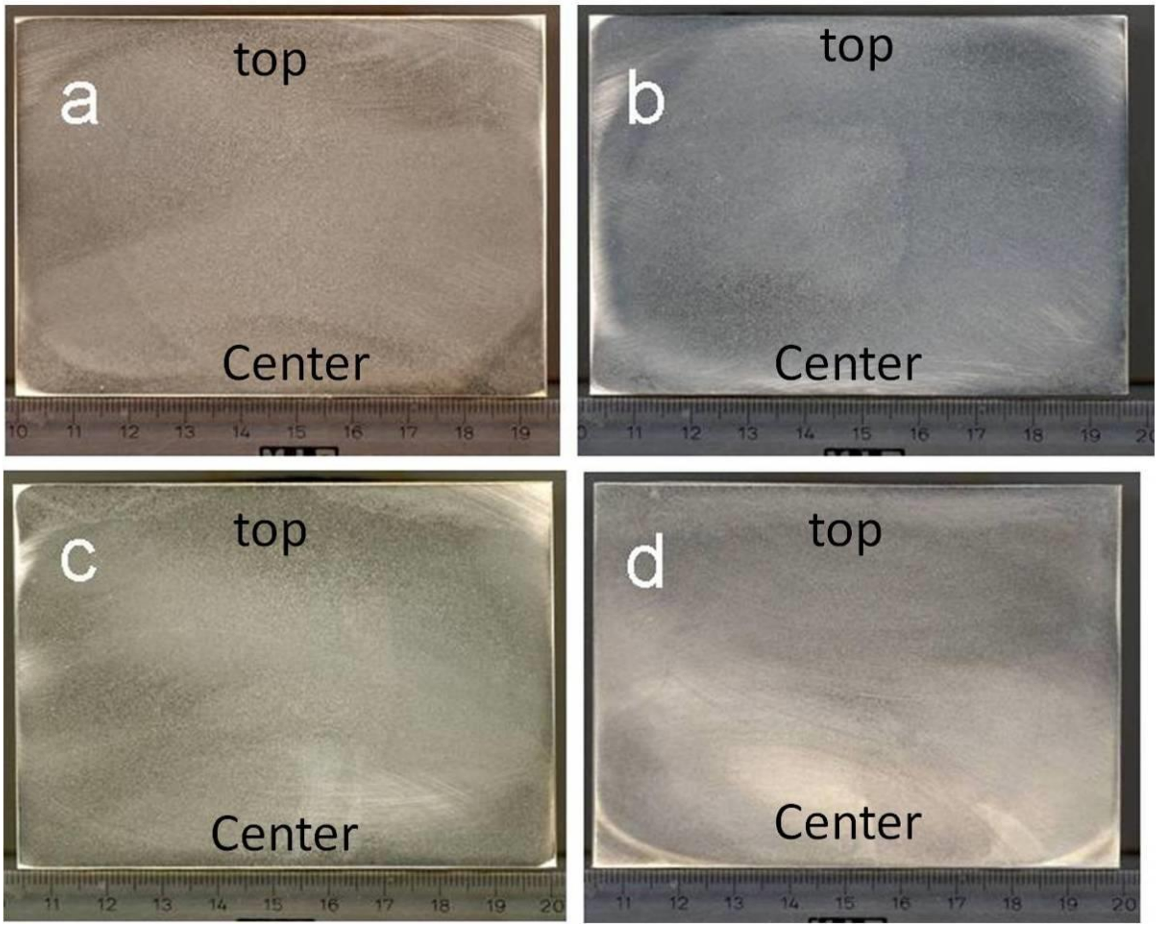

Fig. 60. Macro structure of the as-cast alloys in vertical direction: (a) D10K; (b) DG82K; (c) DG55K; (d) DG28K. The unit of the scale is “cm”. The samples were cut from the top part of the ingots.

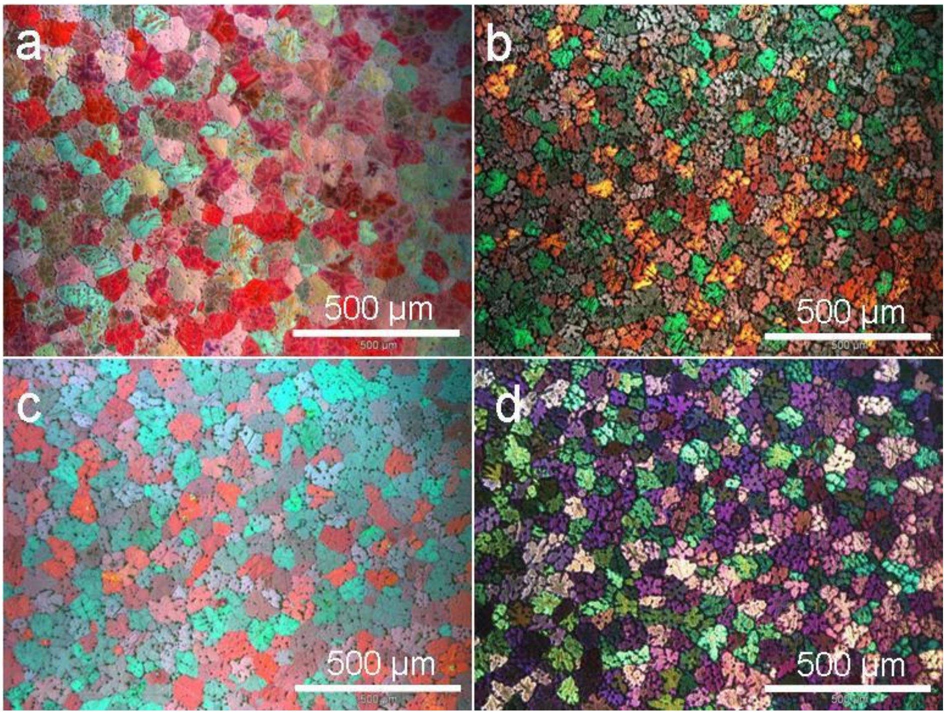

Fig. 61: Optical microstructure of the as-cast alloys: (a) D10K; (b) DG82K; (c) DG55K; (d) DG28K.

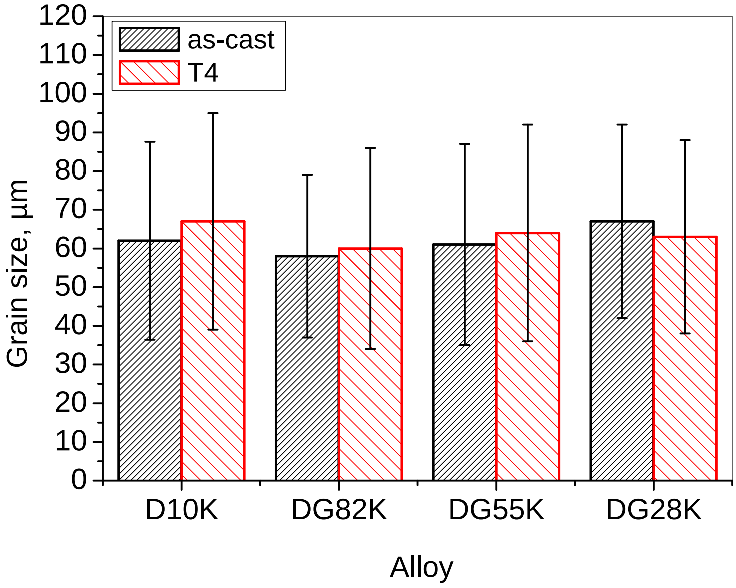

Fig. 62: Grain size of alloys in as-cast and T4 conditions

Fig. 63 shows the SEM microstructure of alloys in the as-cast condition. The SEM microstructure of all alloys consists of Mg matrix, segregation area with a high concentration of alloying elements and second phase particles as indicated by arrows, Fig. 63. A large amount of segregation was observed in all alloys located at the interdendritic region and the grain boundaries. The second phase is mainly distributed inside the segregation area. For D10K and DG82K alloys, only small number of fine scale second phase particles was observed (Fig. 63 (a), (b)). As the Gd content increases, both the amount and size of second phase particles increase (Fig. 63 (c), (d)). In DG28K alloy, the size of the second phase particles reaches to ~15 µm in length (Fig. 63 (e)).

The distribution of alloying elements in Mg matrix, segregation area and second phases was analyzed by EDX, Table 18. In the Mg matrix, with the increase in Gd content the concentration of dissolved Dy decreases. As an example, the DG82K alloy has 3.27 wt.% Dy and 0.68 wt.% Gd in the Mg matrix, while the DG28K alloy has 1.03 wt.% Dy and 2.36 wt.% Gd in its Mg matrix.

Very high percentage of alloying elements was detected in the segregated regions. Similar to the trend of alloying elements in the matrix, the total amount of alloying elements (Dy + Gd) in the segregated area also reduces with the increase in Gd. As an example, the Dy content is 19.6 wt.% in the segregation area of D10K alloy. The total Dy and Gd content is reduced to around 15.5 wt.% in the segregation area of DG28K.

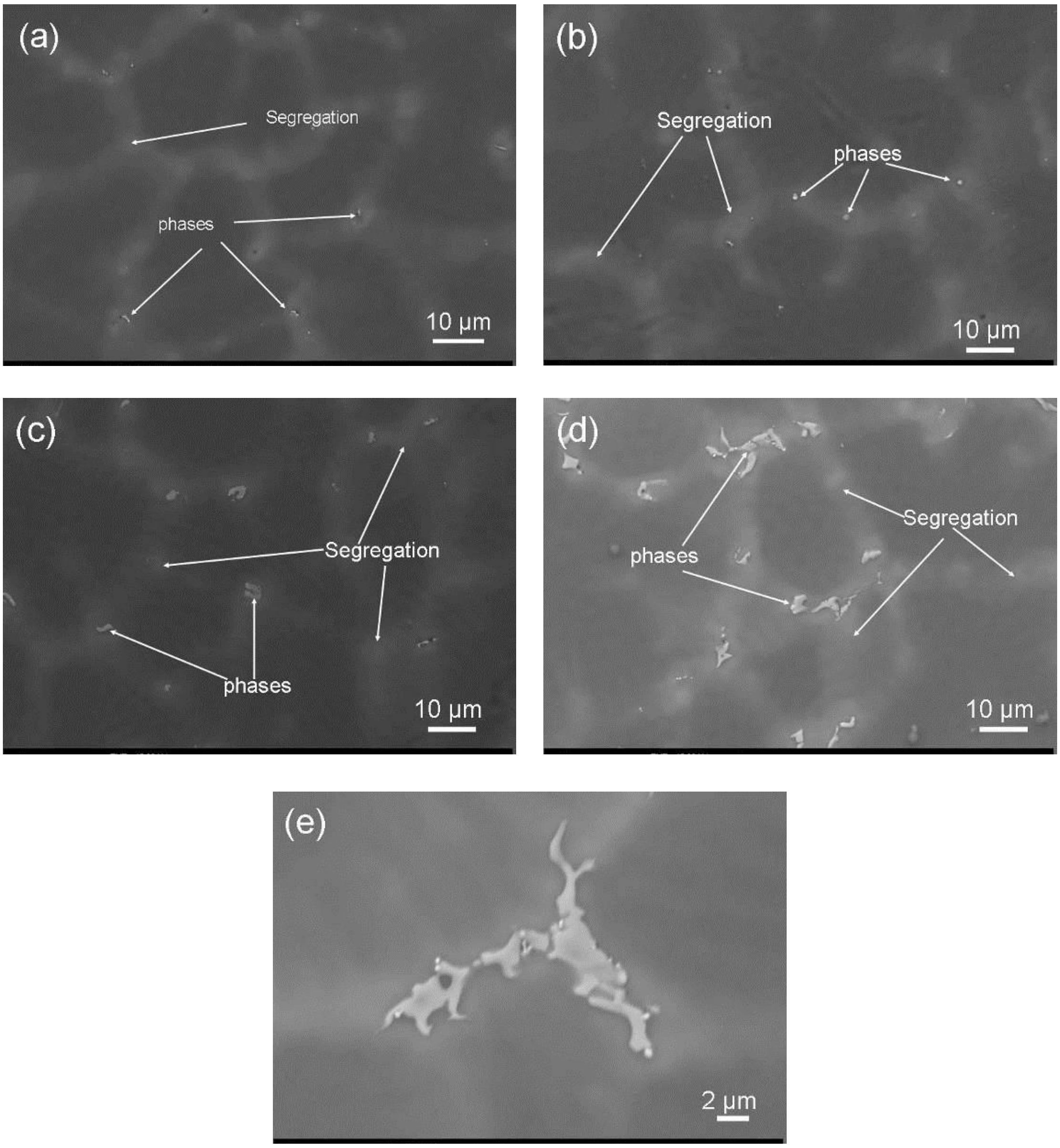

Fig. 63: SEM microstructure of the as-cast alloys: (a) D10K; (b) DG82K; (c) DG55K; (d) DG28K; (e) second phase in DG28K.

Due to the small size of second phases in D10K and DG82K alloys, EDX analysis on composition of these particles cannot be determined with any accuracy. Thus, only the composition of second phase particles in DG55K and DG28K are available (Table 18). Both Dy and Gd were found in the second phase particles, with the Gd amount much higher than Dy in the particles. As an example, there is approximately twice the

Gd content (32.5 wt.%) compared to the Dy content (14.6 wt.%) in the second phase particles of DG55K alloy, despite similar Gd and Dy content in the alloy. In the second phase particles in the DG28K alloy, the Dy content is only 6.7 wt.% while Gd content is ~44.1wt%. The total amount of RE (Dy + Gd) in the second phase particles is similar for all alloys and is ~ 50 wt.% (14at.%).

Table 18: Distribution of alloying element in as-cast alloys (wt.%), analyzed by EDX.

alloys	Dy (matrix)	Gd (matrix)	Dy (segregation)	Gd (segregation)	Dy (phase)	Gd (phase)
D10K	4.08±0.26	--	19.6±0.73	--	--	--
DG82K	3.27±0.11	0.68±0.08	14.8±1.61	4.1±0.64	--	--
DG55K	2.24±0.38	1.52±0.23	8.77±0.57	8.16±0.85	14.6±0.81	32.5±1.8
DG28K	1.03±0.06	2.36±0.14	3.3±0.17	12.2±0.34	6.74±0.25	44.1±1.82

5.2.2.2 Microstructures after T4 treatment

The optical microstructures show that the grains are still equiaxed and their distribution remains to be homogeneous after T4 heat treatment (Fig. 64). The grains did not coarsen during heat treatment and maintained a grain size of ~ 60 µm (Fig. 62). The SEM microstructures show that the segregation is completely eliminated for all alloys, and most of the second phase particles were dissolved into the matrix following T4 heat treatments (Fig. 65). Only very few second phase particles remained in the DG55K and DG28K alloys (Fig. 65 (c, d)).

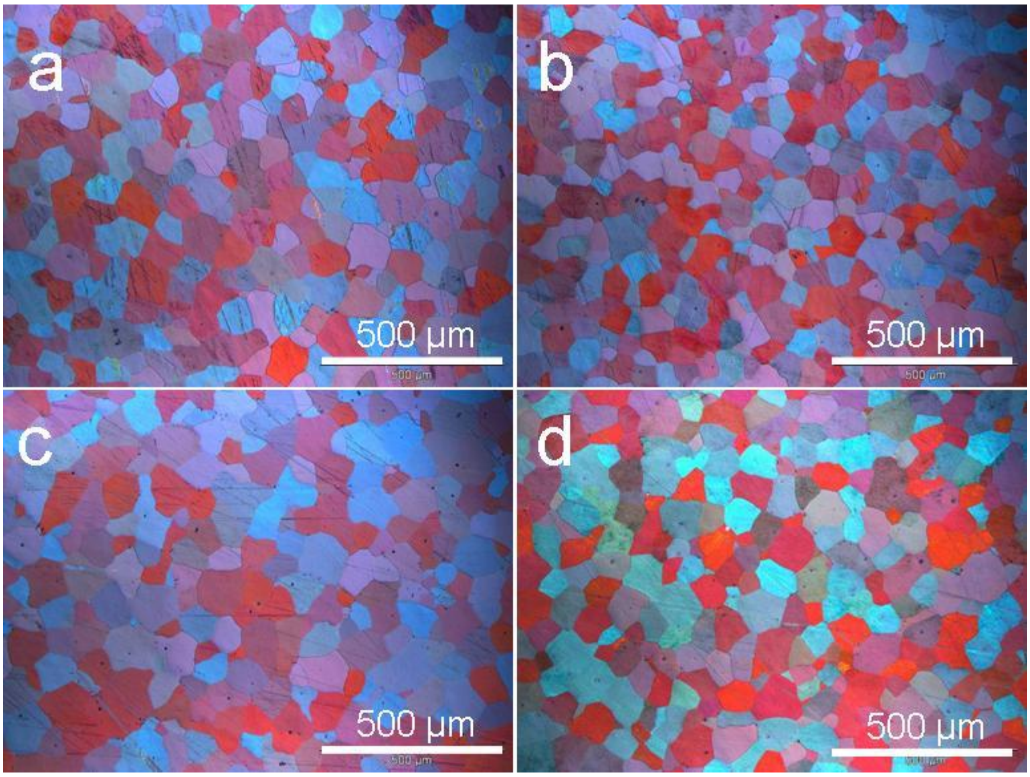

Fig. 64; Optical microstructure of alloys after T4 treatment: (a) D10K; (b) DG82K; (c) DG55K; (d) DG28K.

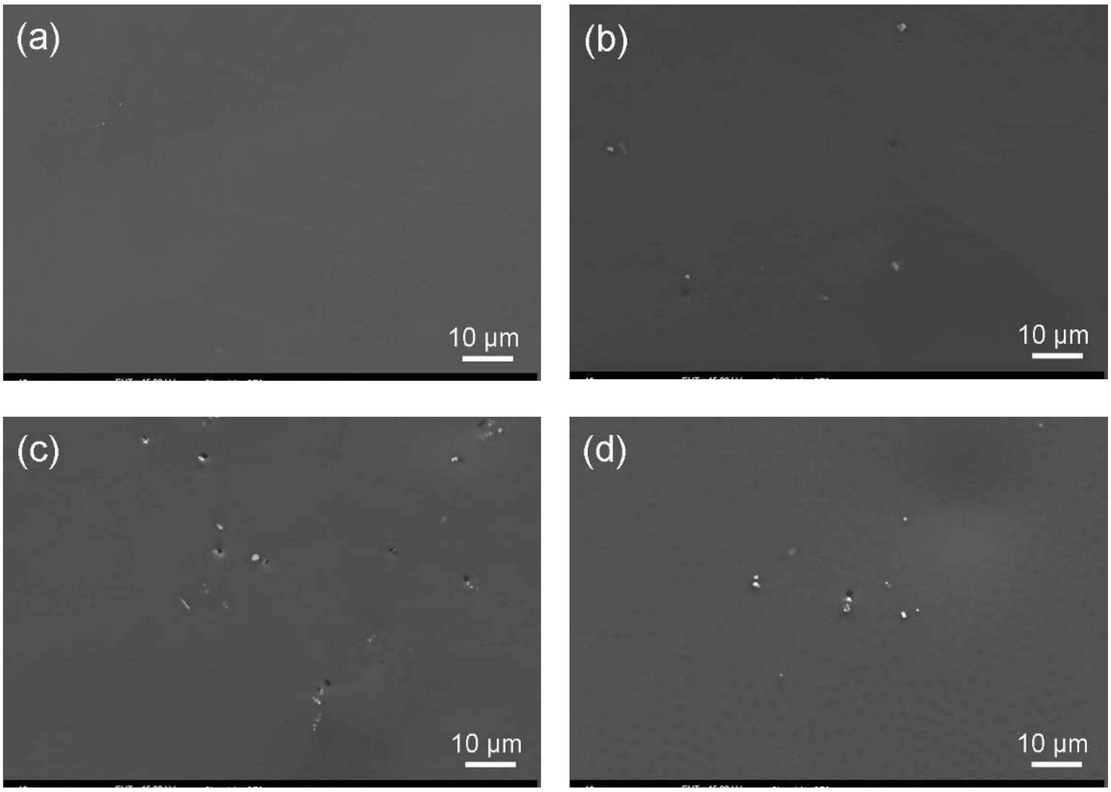

Fig. 65: SEM microstructure of alloys after T4 treatment: (a) D10K; (b) DG82K; (c) DG55K; (d) DG28K.

5.2.2.3 Microstructures after T6 treatment

The age hardening response of Mg-Dy-Gd alloy at 200 °C is shown in Fig. 66. D10K alloy show no age hardening at 200 ^{o}C. With increasing Gd content, age hardening is observed. DG82K and DG55K alloys reach the peak hardness after 216 h. DG28K alloy reached the peak hardness after only 72 h. A plateau following the maximum hardness was observed from 210 h to 384 h and from 72 to 120 h for DG55K and DG28K alloys, respectively. Further aging leads to a slow decrease in the hardness.

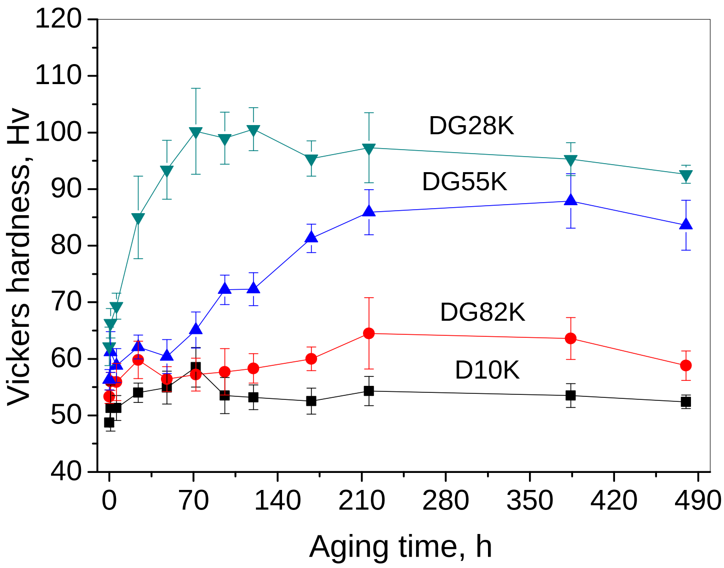

Fig. 66: Hardness of Mg-Dy-Gd alloys after ageing at 200 °C for different time.

Fig. 67 and Fig. 68 present transmission electron micrographs recorded from DG28K alloy aged at 200°C for 72 h. Large number of precipitates with plate-like morphology with a size of 20-50 nm in length and 10-25 nm in diameter were observed when the electron beam was parallel to $[10\bar{1}0]_{\alpha}$, (Fig. 67 (a, b)) The additional reflections on the selected area diffraction pattern (Fig. 67 (b)) can be indexed according to metastable phase β’ ($Mg_{13}RE_3$, base-centred orthorhombic structure (a = 0.64 nm, b = 2.22 nm, c = 0.52 nm)) [108]. The precipitates look to be spherical in morphology when the electron beam is approximately parallel to $[\bar{1}2\bar{1}3]_{\alpha}$, and they distributed uniformly in the matrix (Fig. 68 (a), (b)). XRD analysis also revealed β′ phase forms in DG28K alloy after ageing at 200°C for 216 h (Fig. 69).

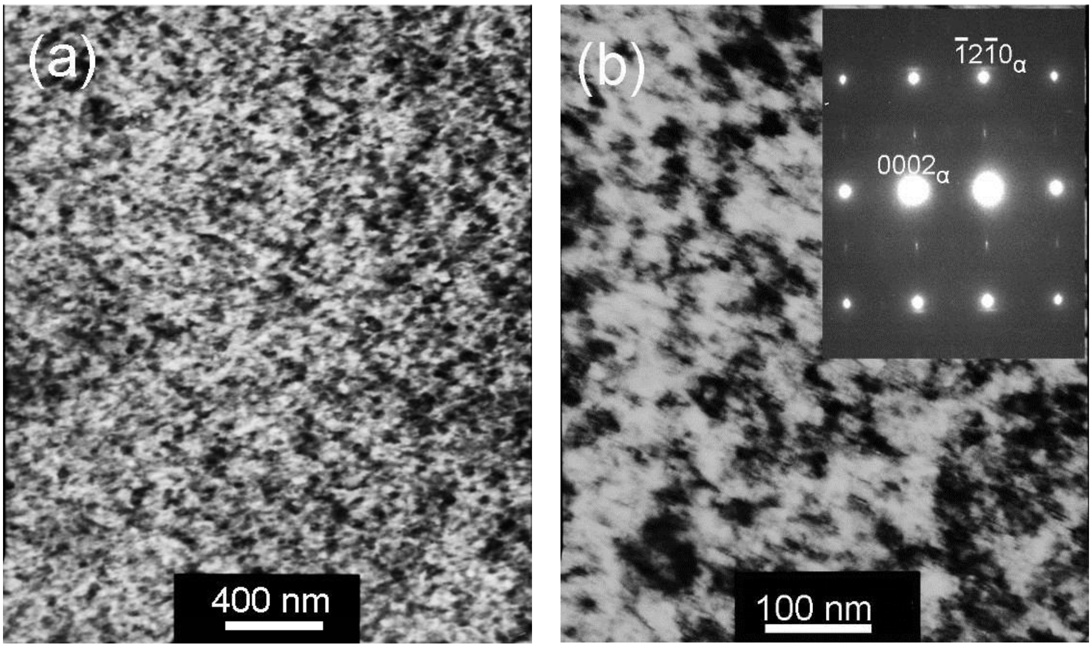

Fig. 67: TEM pictures and selected area diffraction pattern of DG28K alloy aged at 200°C for 72 h: (a) low magnification (b) high magnification and corresponding diffraction pattern along the zone axis $[10\bar{1}0]_\alpha$.

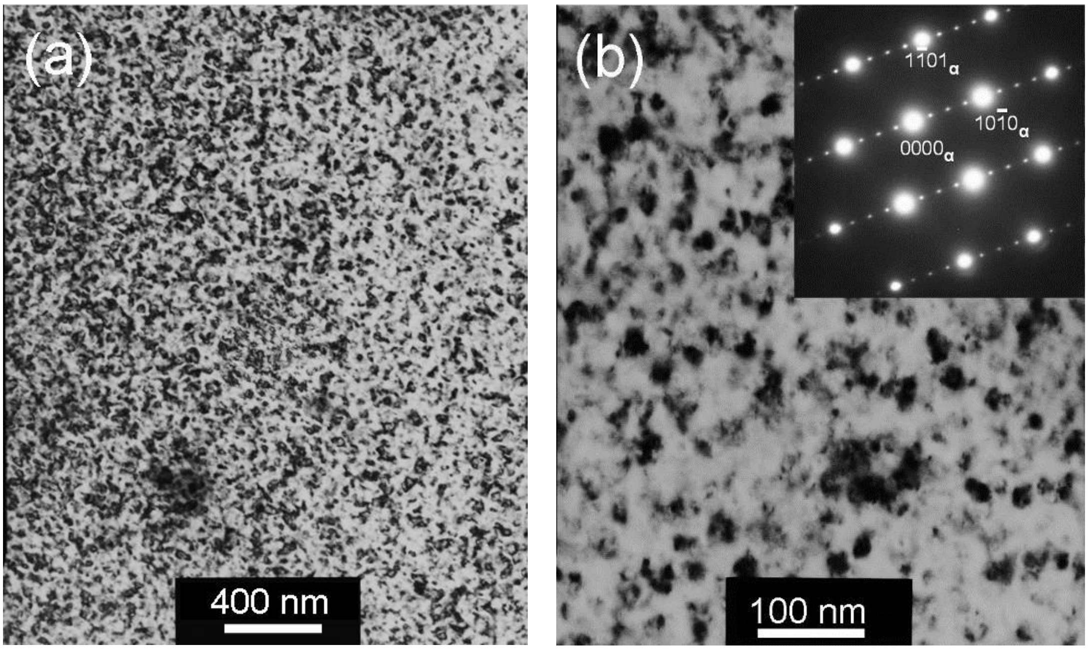

Fig. 68: TEM pictures and selected area diffraction pattern of DG28K alloy aged at 200°C for 72 h: (a) low magnification (b) high magnification and corresponding diffraction pattern along the zone axis $[\bar{1}2\bar{1}3]_\alpha$.

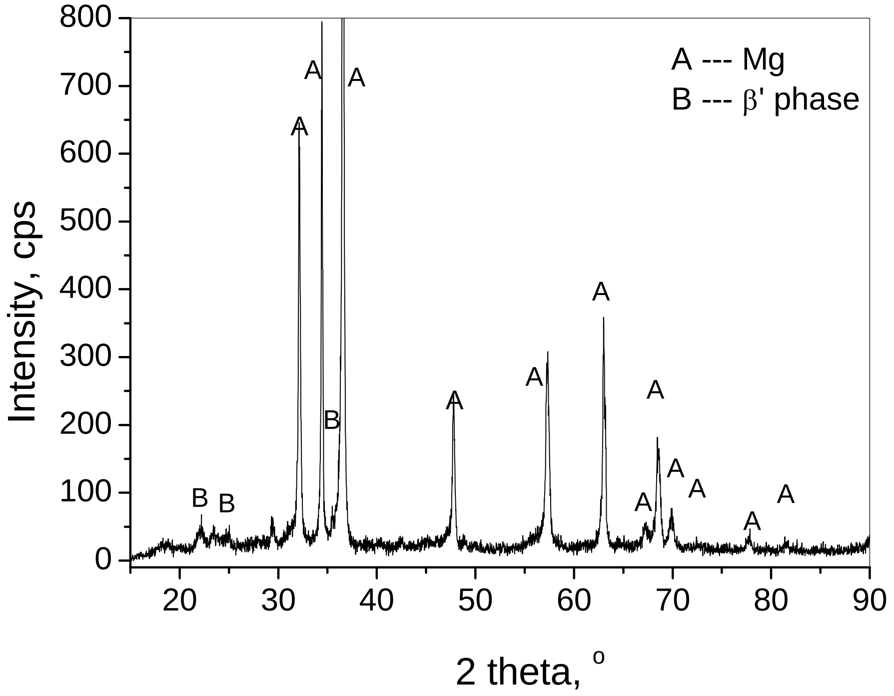

Fig. 69: XRD pattern of DG28K alloy aged at 200°C for 216 h.

5.2.3 Mechanical properties

5.2.3.1 Hardness

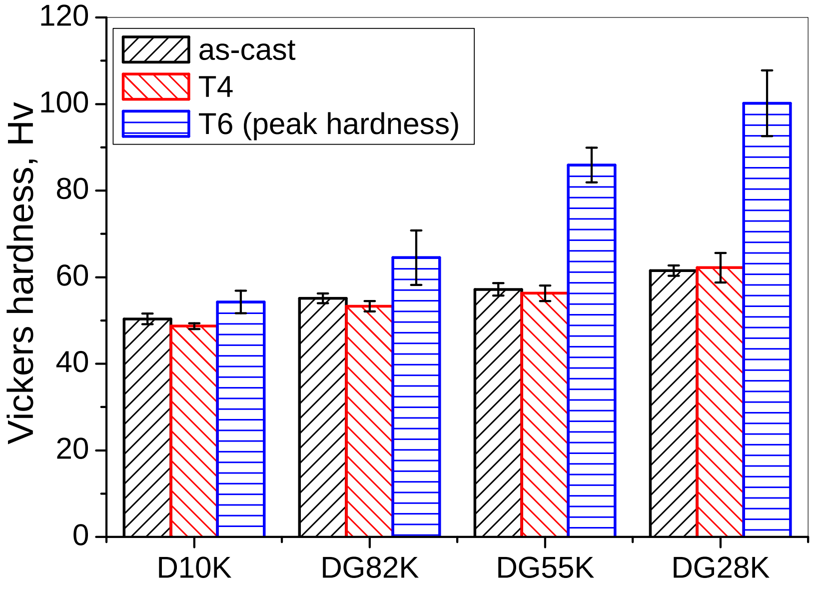

Fig. 70: Vickers hardness of alloys in different conditions.

Fig. 70 shows the Vickers hardness of alloys after processing under different conditions. In the as-cast alloys, the Vickers hardness is around 50 for D10K alloy and it increases with the increase in Gd content, reaching to around 60 for DG28K alloy. After T4 heat treatment, the Vickers hardness decreases marginally for all alloys. After the T6 heat treatment, the Vickers hardness increases for all alloys and the improvement is higher for the alloys with a higher Gd content. For example, it increased from 48 to 54 for D10K alloy, and from 60 to 100 for DG28K alloy.

5.2.3.2 Tensile properties

Fig. 71 (a) shows the TYS of alloys following different processing conditions. In the as-cast alloys, the TYS increased slightly with the increase in Gd content, TYS increases from 103MPa to 120 MPa when Gd content increased from 0 (D10K) to 8wt.% (DG28K). After the T4 treatment, the TYS does not show any significant change for all alloys similar to the hardness values. After T6 treatment, the TYS remains unchanged for D10K and DG82K alloys, while TYS increases significantly for DG55K and DG28K alloys. It is increased from 120 MPa to 220 MPa for DG28K alloy while the increase is from 120 MPa to 190 MPa for the DG55K alloy.

Fig. 71 (b) shows the UTS of alloys processed under different conditions. In the as-cast alloys, the UTS increases slightly with the increase in Gd content, from 188 MPa to 220 MPa when Gd content is increased from 0 (D10K) to 8wt.% (DG28K). T4 heat treatment has little effect on the UTS. After the T6 treatment, UTS increases marginally for D10K and DG82K alloys, while the increment is significant for the for DG55K and DG28K alloys. It increases from 200 MPa to 360 MPa for DG28K alloy and 200 MPa to 300 MPa for the DG55K alloy following the T6 treatment.

Fig. 71 c shows the tensile elongation of alloys after different processing stages. In the as-cast alloys, the tensile elongation reduces gradually with the increase in Gd content, from 21% to 17.6% when Gd content is increased from 0 (D10K) to 8wt.% (DG28K). After the T4 treatment, the tensile elongation increases marginally for all alloys. After T6 treatment the elongation decreases slightly for D10K and DG82K alloys, while it decreases obviously for DG55K and DG28K alloys. Elongation is reduced from 18.3% to 7.5% for DG28K alloy and 17.5% to 12.5% for the DG55K alloy.

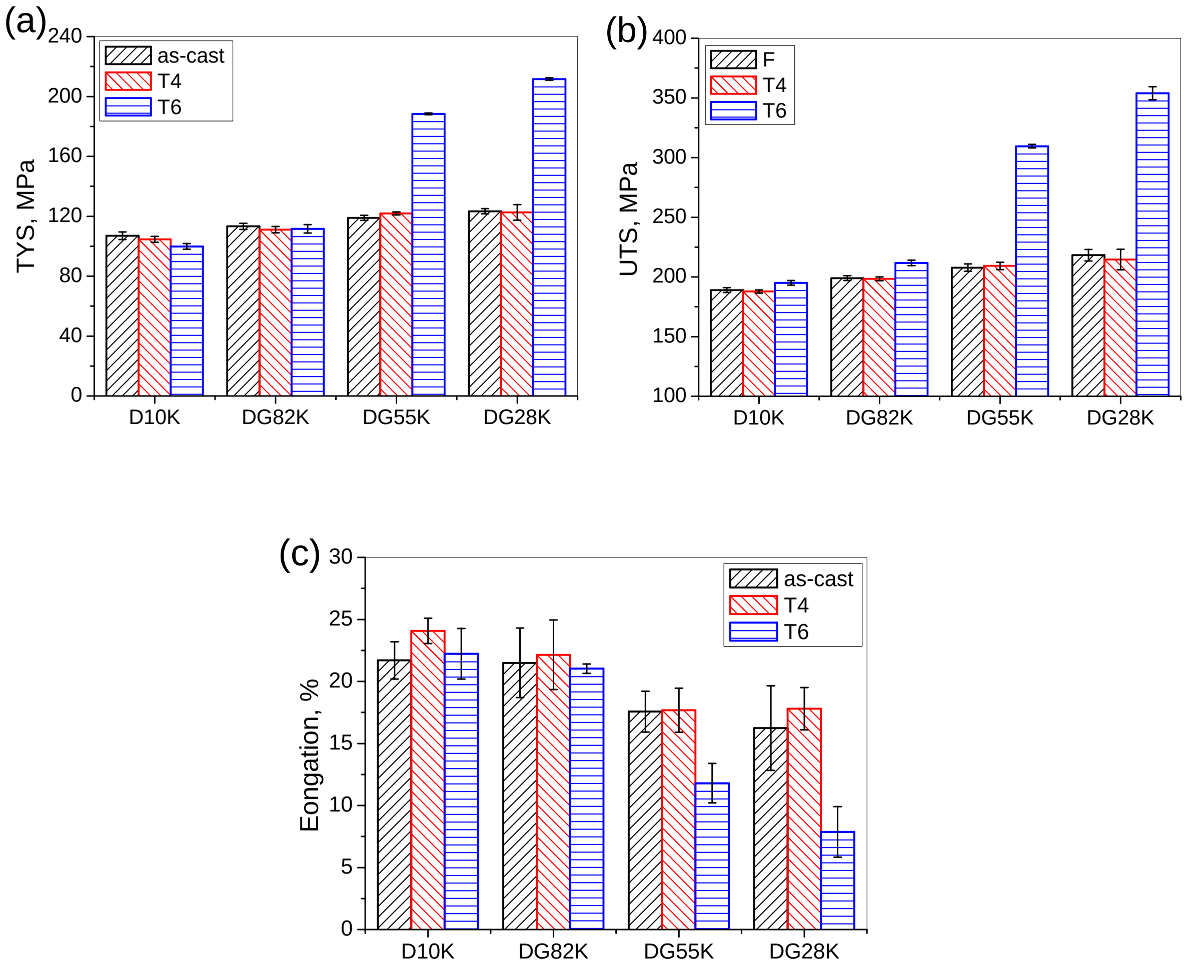

Fig. 71: Tensile properties of Mg-Dy-Gd-Zr alloys in different conditions: (a) tensile yield strength; (b) ultimate tensile strength; (c) elongation.

5.2.3.3 Compressive properties

A similar trend to that observed for tensile properties is measured for the compressive properties of Mg-Dy-Gd-Zr alloys (Fig. 72). In the as-cast alloys the increase in Gd lead to a slight increase in both the CYS and the UCS, and a decrease in the compression to failure. T4 heat treatment did not change the CYS and compressibility (Fig. 72 (a, c)), while it reduces the UCS for all alloys investigated. The UCS reduced from 350 MPa to 290 MPa for DG28K alloy following the T4 heat treatment (Fig. 72 b). After the T6 treatment, the CYS, UTS and compression to failure do not change significantly for the D10K and DG82K alloys (Fig. 72 c). The CYS increases for DG5K and DG28K alloys while a large reduction in the compression to failure is observed (Fig. 72 (a, c)). The UCS increases only for the DG82K alloy following the T6 heat treatment (Fig. 72 b).

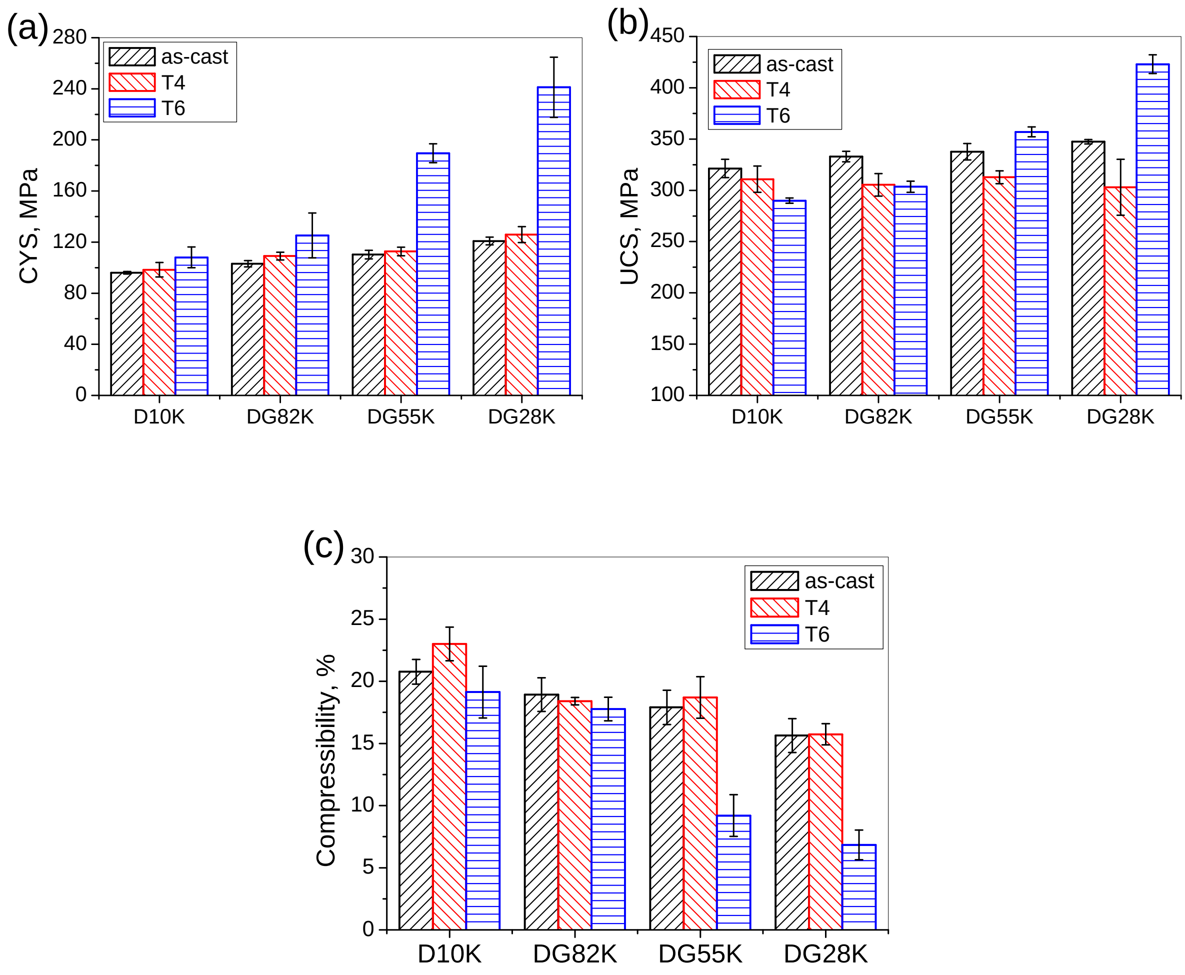

Fig. 72: Compressive properties of Mg-Dy-Gd-Zr alloys in different conditions: (a) compressive yield strength; (b) ultimate compressive strength; (c) Compressibility (strain at maximum stress point).

5.2.4 Corrosion in CCM

Fig. 73 shows the corrosion rates of alloys after immersion in CCM for 14 days under cell culture conditions. The corrosion rate for the as-cast D10K and DG82K alloys are ~0.55 mm/y, and it increases to 0.7 and 0.85 mm/y when Gd increases to 5 and 8 wt.% in DG55K and DG28K alloys, respectively. After the T4 heat treatment, the corrosion rate does not change for the D10K and DG82K alloys, while the corrosion rate reduces to ~ 0.5mm/y for DG55K and DG28K alloys. As a result, all the alloys investigated have a similar corrosion rate following T4 heat treatment. Aging treatment at 200°C (T6) shows no adverse influence on the corrosion rate but reduces the average corrosion rate.

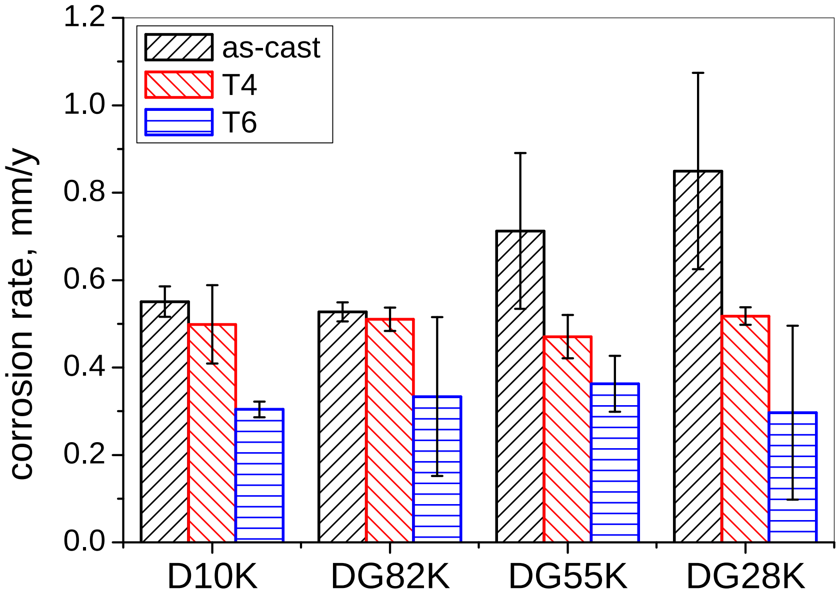

Fig. 73: Corrosion rate of alloys after immersion in CCM for 14 days under cell culture conditions.

The macro corrosion morphology of alloys after 14 days immersion in CCM after the removal of corrosion products is shown in Fig. 74. In the as-cast alloys, localized corrosion occurs on the surface of all alloys as indicated by arrows. In the T4 and T6 treated alloys, no localized corrosion is observed and the corrosion is very uniform.

Fig. 75 shows the corrosion morphology and EDX analysis of corrosion film for T4 heat treated alloys following 14 days immersion in CCM. The corrosion film is uniform despite the large number of cracks observed due to dehydration associated with SEM investigations. There is Dy and Gd enrichment in the corrosion film and content of these elements in the corrosion layer is dependent on the Dy and Gd content of the alloy. This is illustrated by comparing the Dy and Gd contents in DG82K and DG28K alloys where the content of Dy and Gd was 40.6 wt.% and 10.2 wt.% in the corrosion layer of DG82K alloy, respectively and 12.4 wt.% and 45.0 wt.%, respectively for the corrosion layer of DG28K alloy.

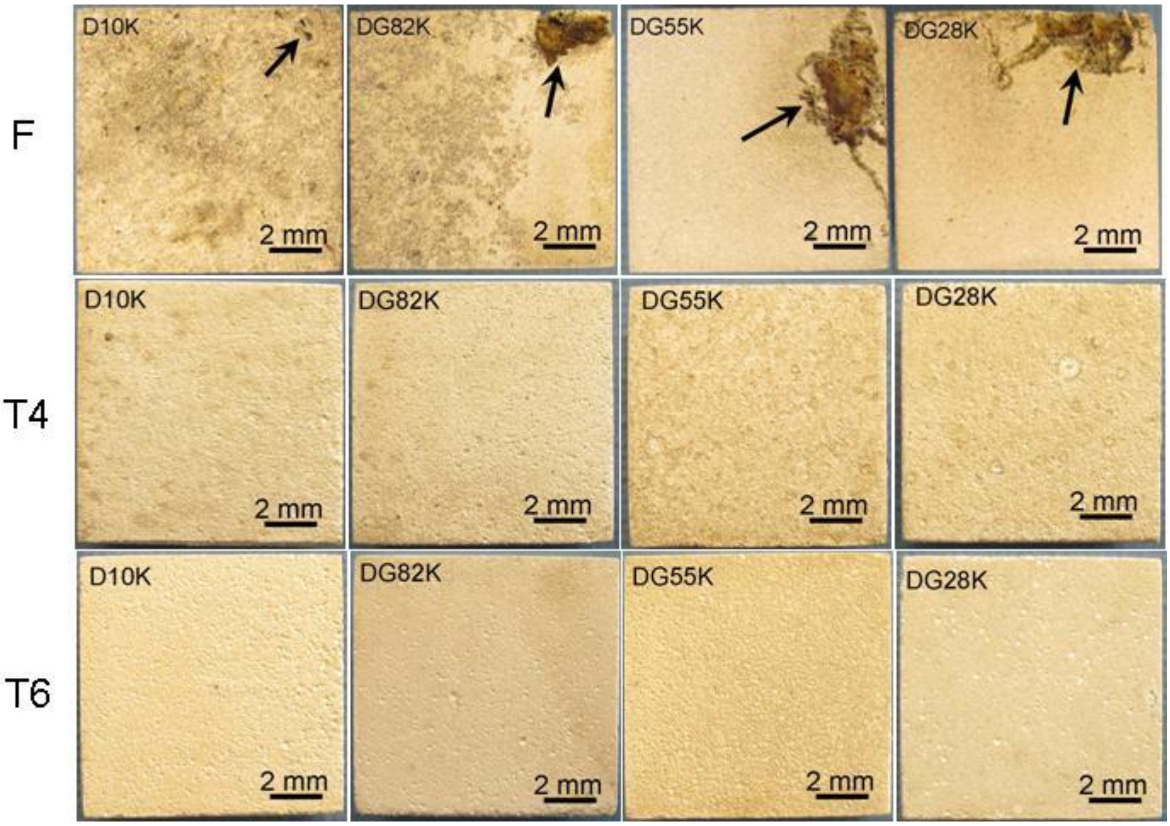

Fig. 74: Macro corrosion morphology of alloys after 14 days immersion in CCM under cell culture conditions (after removal of corrosion products).

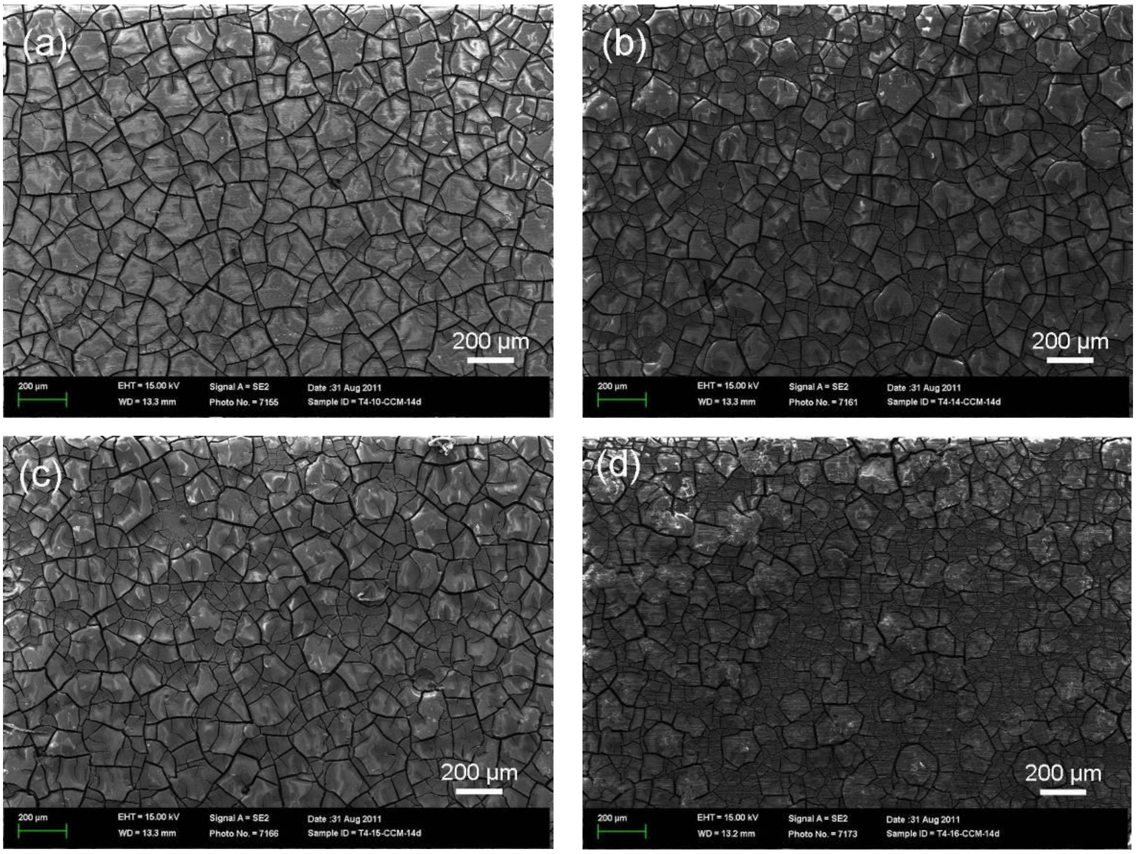

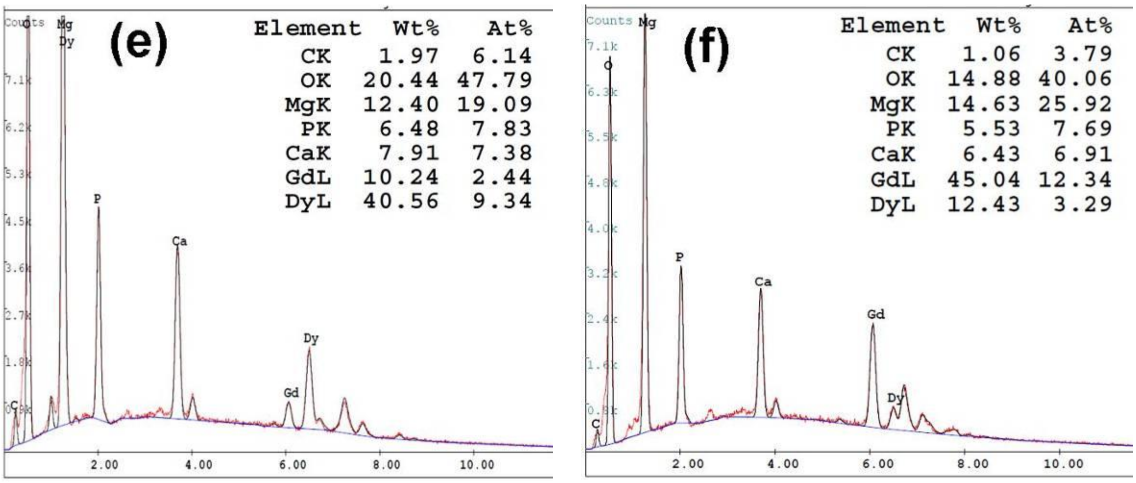

(e)

Element	Wt%	At%
CK	1.97	6.14
OK	20.44	47.79
MgK	12.40	19.09
PK	6.48	7.83
CaK	7.91	7.38
GdL	10.24	2.44
DyL	40.56	9.34

(f)

Element	Wt%	At%
CK	1.06	3.79
OK	14.88	40.06
MgK	14.63	25.92
PK	5.53	7.69
CaK	6.43	6.91
GdL	45.04	12.34
DyL	12.43	3.29

Fig. 75: Corrosion morphology of alloys (T4) after immersion for 14 days in CCM: (a) D10K; (b) DG82K; (c) DG55K; (d) DG28K; (e) EDS analysis of corrosion layer on (b); (f) EDS analysis of corrosion layer on (d).

DG28K showed the largest age hardening response at 200°C and was selected to investigate the effect of T6 heat treatment on bio-corrosion morphology. Fig. 76 shows the corrosion morphology and composition of the corroded surface of DG28K alloy with T6 treatment after immersed in CCM for 14 days. The corrosion layer is very uniform and the enrichment of Dy and Gd is observed in the corrosion layer. The content of enriched Dy and Gd in the corrosion layer is similar to those in T4 condition. T6 treatment shows no effect on the corrosion layer of DGK alloys in the CCM.

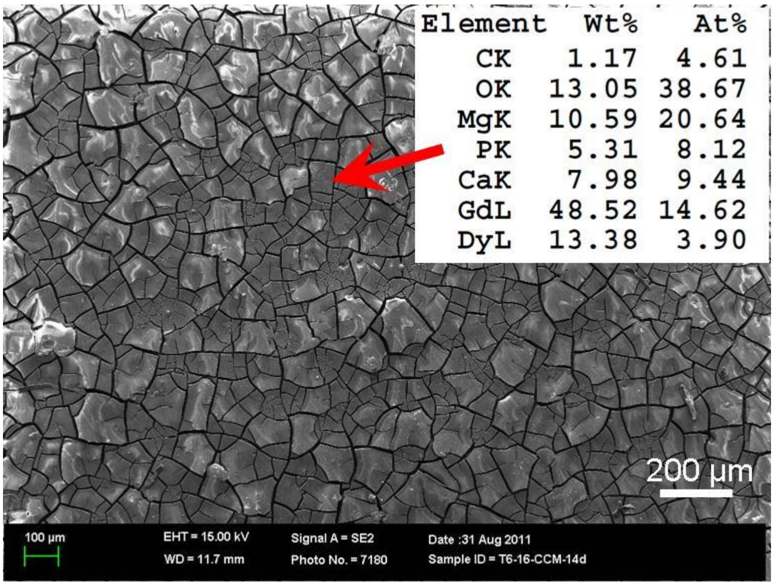

Element	Wt%	At%
CK	1.17	4.61
OK	13.05	38.67
MgK	10.59	20.64
PK	5.31	8.12
CaK	7.98	9.44
GdL	48.52	14.62
DyL	13.38	3.90

Fig. 76: Corrosion morphology and composition (analyzed by EDX) of the corroded surface of DG28K alloy with T6 treatment after immersion for 14 days in CCM

5.2.5 Cytotoxicity evaluation

Fig. 77 and Fig. 78 show the live and dead cells on surfaces of pure Mg and DG55K alloy after exposure to osteoblast cultures for 3 and 7 days, respectively. After exposure for 3 days, a large number of live cells were found on both the pure Mg and DG55K alloy (Fig. 77 (a, c)). These cells were well-spread and adhered to the corrosion layer. Very few dead cells are observed after 3 days (Fig. 77 (b, d)). After 7 days, the live cells are spread even further and the numbers of dead cells are very few in comparison with the number of live cells (Fig. 78).The quantification of cell viability on the pure Mg and DG55K alloy is presented in Fig. 79. After 3 days, the cell viability is ~ 89% on pure Mg and ~92% on DG55K alloy. After 7 days, the cell viability remains above 90% for both pure Mg and DG55K alloy. The enrichment of RE (Dy and Gd) in the corrosion layer shows no adverse effect on the adhered cells.

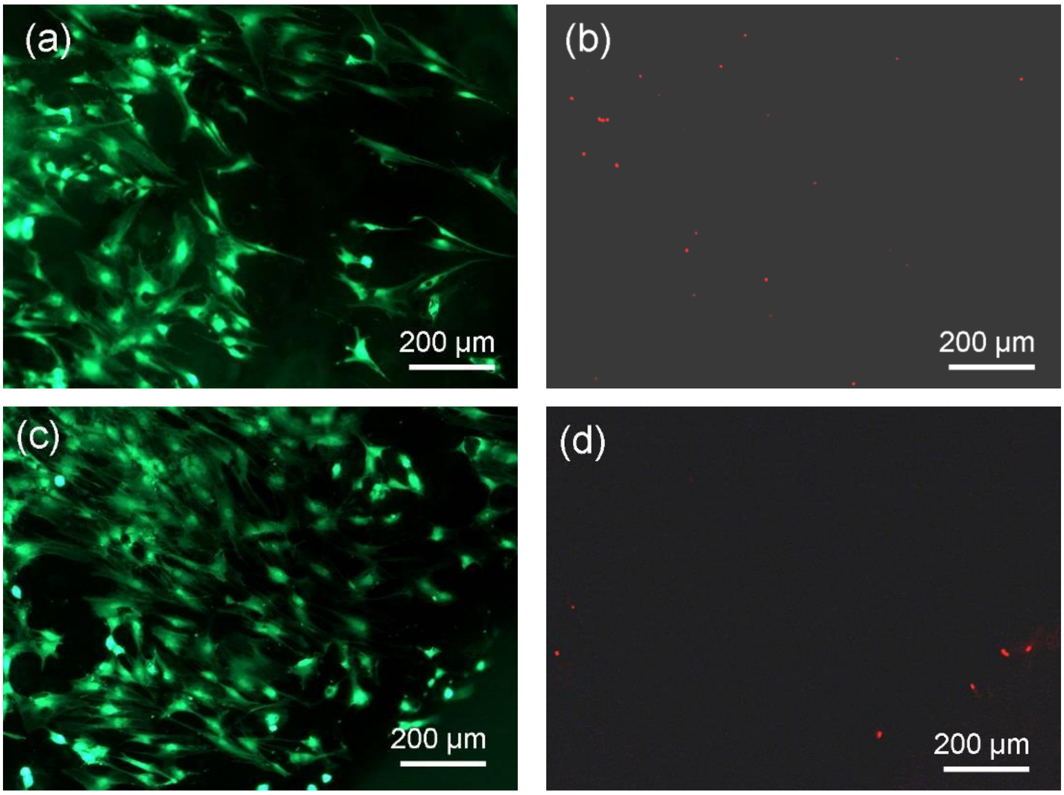

Fig. 77: Live (green) and dead (red) cells on pure Mg (a, b) and DG55K alloy (c, d) after culture for 3 days. Prior to the test, specimens were pre-incubated in CCM for 3 days. Images for live and dead cells were taken from the same position.

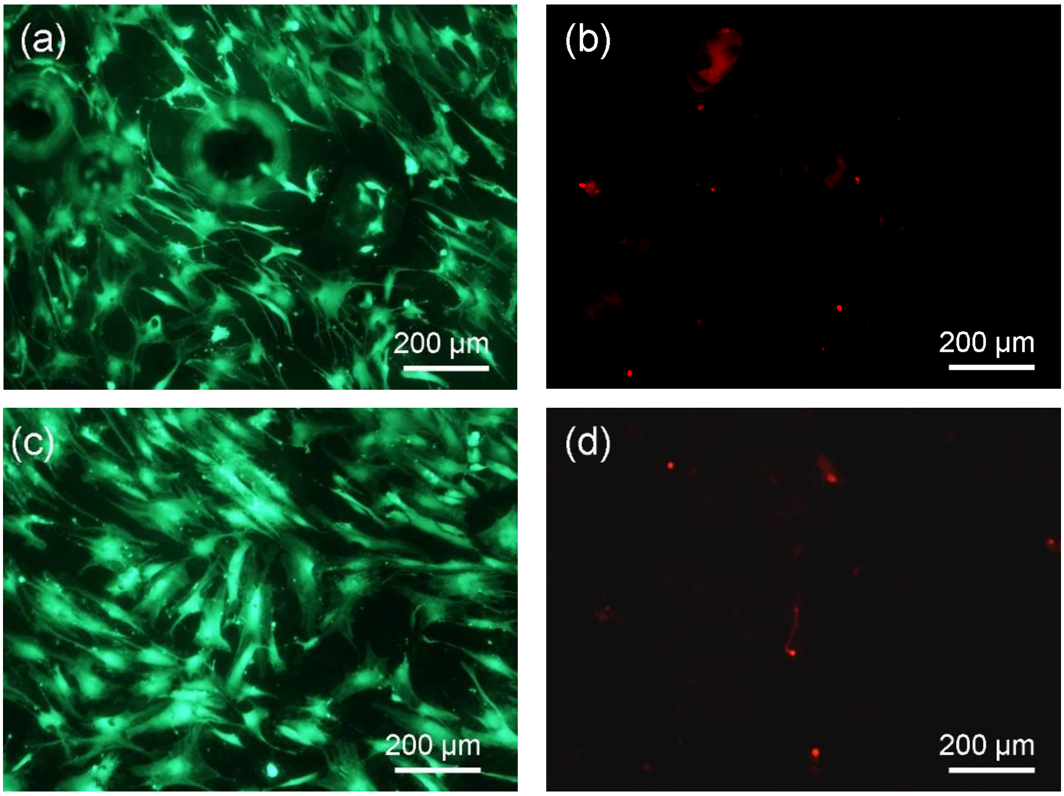

Fig. 78: Live (green) and dead (red) cells on pure Mg (a, b) and DG55K alloy (c, d) after culture for 7 days. Prior to the test, specimens were pre-incubated in CCM for 3 days. Images for live and dead cells were taken from the same position.

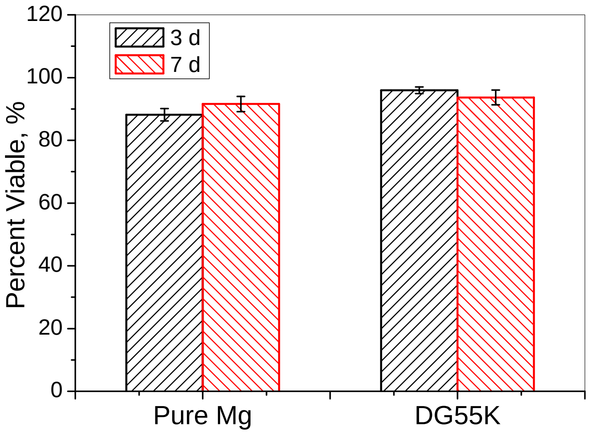

Fig. 79: Quantification of cell viability on pure Mg and DG55K alloy.

6 Discussion

6.1 Mg-Dy alloys

6.1.1 Microstructure and age hardening behaviour

Due to the high cooling rate associated with direct chill casting, the solidification process proceeds under a non-equilibrium condition. After solidification, the distribution of Dy is not homogeneous. A large amount of Dy distributes in the Mg matrix and in regions of Dy segregation, and only a small amount of Mg-Dy phases form in all alloys. According to the Mg-Dy binary phase diagram [111] (Fig. 9), only $Mg_{24}Dy_5$ can form close to the magnesium rich end of the phase diagram. The $Mg_{24}Dy_5$ phase is also confirmed as the only phase found in the alloys investigated by the SEM-EDX, XRD and TEM investigations.

T4 heat treatment was performed at 520 °C for 24 h to homogenise the Dy distribution and to dissolve any second phase particles. The diffusion of Dy occurs from the regions near grain boundaries to the centre of the grains during the heat treatment. At 520°C, the second phase particles of $Mg_{24}Dy_5$ are unstable in the investigated alloys and dissolve during the solution treatment. The time to dissolution is dependent on the size and the distribution of particles. Based on the Mg-Dy binary phase diagram, the solubility of Dy in α-Mg matrix reaches to 22 wt.% at 520 °C suggesting complete dissolution of Dy into α-Mg matrix. However, there are few particles of $Mg_{24}Dy_5$ phase left in the α-Mg matrix in Mg-15Dy and Mg-20Dy alloys following T4 heat treatment. This is due to the slower diffusion rate of Dy in solid Mg [119].

To optimize the ageing temperature, ageing behaviour at 200 °C and 250 °C were investigated. At 200°C, the solid solubility of Dy is about 10 wt.% (Fig. 9). A significant age hardening response was observed for Mg-20Dy alloy when aged at 200°C. After ageing at 200^{o}C for 168 h, a large number density of fine precipitates distributes uniformly within Mg-matrix. For Mg-10Dy and Mg-15Dy alloys with a relative low content of Dy, the increase in the Vickers hardness is still limited after ageing due to the high solid solubility of Dy in Mg at lower temperatures. At 250°C, the solubility of Dy in magnesium is 14 wt.% (Fig. 9). Thus, age hardening behaviour was expected for Mg-20Dy alloy. However, Mg-20Dy alloy only showed marginal increase in the Vickers hardness as a function of ageing time. The previously published Mg-Dy phase diagram may not therefore explain the observed experimental phenomena completely and clearly as it is still not complete and contains lines of uncertainty (Fig. 9). The less noticeable age hardening behaviour of Mg-20Dy alloys at 250 °C may hint that the solubility of Dy in the α-Mg matrix could be higher than 14 wt.% at 250 °C. The driving force for the precipitation is low and there are only few precipitates forming during ageing.

In Mg-RE alloys such as Mg-Y or Mg-Gd based alloys, due to the lower diffusivity of RE in Mg at ageing temperatures, metastable phases precipitate prior to formation of equilibrium phases during ageing. The precipitation sequence is normally given as follows [120, 121]:

SSSS (supersaturated solid solution)-β''- β' - β_1 - β

In this work, after ageing at 200 °C for 168 h, β' precipitates are identified by both XRD and TEM. The β' precipitates were also observed in Mg-Gd [115], Mg-Dy-Nd [112], Mg-Gd-Y [116] and Mg-Y-Nd [118] systems. At 250°C, the metastable β'' phases are observed when aged for short times (less than 1 h) [120, 121]. Upon further ageing β'' precipitates transforms into to β' particles [120, 121] and then β' phase transform to β_1 phase after several hours of ageing at 250 °C [120, 121]. The formation of β equilibrium phase takes more than 2000 h (over ageing) when aged at 250 °C [120, 121]. Since the ageing time at 250°C is short in the present investigation, it is not expected that equilibrium β phase forms during the time investigated. Based on the morphology and size of the precipitates in Fig. 25 (c, d), it is deduced that the precipitates in Mg-20Dy alloy with T6-2 treatment are also mainly β' phases.

Based on the binary Mg-Dy phase diagram (Fig. 9), the solubility of Dy in the Mg matrix reduces with the decrease in temperature. Less Dy is kept in the matrix and more Dy is consumed to form β' phase in alloys when aged at 200 °C in comparison with 250 °C. The growth rate of the β' precipitate at 200 °C is slower than at 250 ^{o}C and there is time for the nucleation of higher density of precipitates at 200 °C. Therefore, the precipitates in the T6-1 condition are denser and smaller than those in the T6-2 condition as illustrated in Fig. 25.

6.1.2 Mechanical properties

In the as-cast alloys, with the increase in Dy, the amount of Dy in both the α-matrix and the segregated areas increases. Since the amount of second phases in these four Mg-Dy alloys is very small, the particle strengthening is negligible. The atomic diameter of elemental Dy (178 pm) is 11% larger than that of Mg (160 pm). The large difference in the atomic radius results in lattice distortion, and consequently the alloy is strengthened due to the solid solution strengthening. The Dy in the α-Mg matrix and segregation area deteriorates the ductility. Although the slight improvement in elongation is found when Dy increases from 5 wt.% to 10 wt.%, this is mainly attributed to grain refinement. The further addition of Dy only results in the increase of intermetallic phases and Dy amount in Mg matrix as well as segregation area, but little grain refinement was observed. The elongation decreases dramatically when Dy increases from 10 wt.% to 15 wt.%. The 10 wt.% Dy is the critical point for the change of elongation as a function of the content of Dy in the as cast Mg-Dy alloys. The investigation on Mg-Gd alloys indicates that the critical point for the change of elongation in Mg-Gd alloys is at about 5 wt.% [34].

After the T4 heat treatment, the loss of strength is mainly attributed to the grain coarsening. For the Mg-5Dy, Mg-10Dy and Mg-15Dy alloys, the grain size increased. As a result, the yield strength reduces. However, the Mg-20Dy alloy does not show any changes in grain size after T4 treatment and its yield strength is unchanged.

During the T6 treatment the supersaturated α-Mg solid solution decomposes to precipitate β′ phase (Fig. 25) which provide a barrier to dislocation movement. Dy then strengthens through both solid solution and precipitate strengthening. The precipitates in T6-1 condition are denser and smaller than those in T6-2 condition, and also contain a larger number density as shown in Fig. 25. A high density of intrinsically strong, plate-shaped precipitates with prismatic habit planes and large aspect ratios could contribute to significant strengthening [122]. This is demonstrated by the significant increment in hardness and the YS following T6-1 treatment compared with the marginal improvement after T6-2 treatment.

6.1.3 Corrosion rate and morphology

There is no information on the electrochemical potential of Mg–Dy intermetallics.

Typically most Mg intermetallic causes galvanic corrosion, leading to the acceleration of corrosion [26]. The electrochemical potential of Dy is -2.35 V, similar to that of Mg (-2.37 V). This indicates that elemental Dy would not cause micro-galvanic corrosion of the α-Mg matrix while Dy is in solid solution with α-Mg matrix. Additionally RE elements are able to improve the protective nature of the surface film by the formation of $RE(OH)_3$ and / or RE_2O_3 [123, 124]. As a consequence, there are two important influences of Dy on the corrosion of Mg–Dy alloys. Firstly, precipitation of the Dy-containing intermetallic can lead to micro-galvanic corrosion and accelerate the corrosion rate. Secondly, Dy, in the oxidized state, can incorporate in the surface film, increase its protectiveness and thereby decrease the corrosion rate.

6.1.3.1 NaCl solution

As NaCl solution is different from human body fluid, the use of NaCl solution as corrosion medium is to have a primary understanding of the corrosion behaviour of Mg-Dy alloys. Furthermore, it is to compare the corrosion behaviour in NaCl solution and CCM. If the corrosion behaviour is similar, the simple NaCl solution can be used as a primary evaluation method on Mg alloys for medical applications.

Based on the corrosion morphology as shown in Fig. 31 and Fig. 34, it can be concluded that the different contents of Dy and its state could result in the different corrosion mechanisms, namely filiform and/or pitting corrosion.

Pitting corrosion is very common in Mg alloys, which is generally caused by galvanic corrosion between Mg matrix and second phase particles [26]. In AZ91 a large amount of $Mg_{17}Al_{12}$ phases forming with a continuous network structure act as a corrosion barrier to retard the corrosion. However, a small amount of $Mg_{17}Al_{12}$ phases act as a cathode and form galvanic couples with the Mg matrix, accelerating the corrosion rate [26, 125]. For the Mg-Dy alloys, the quantity of the second phase particles is too low to form a continuous network structure and pitting corrosion starts from the interfacial regions (at the side of Mg matrix) between $Mg_{24}Dy_5$ phase and Mg. With the increase in Dy content, more second phase particles form in the as-cast alloys. As a result, more pitting corrosion occurs during corrosion process. After T4 treatment, only few precipitates remain in the Mg-Dy alloys with less than 15 wt.% Dy. Therefore, the pitting corrosion is reduced. However, for the Mg-20Dy alloy, the pitting corrosion still occurs as precipitates still remains.

Filiform corrosion was observed in several investigations for Mg alloys in NaCl solutions [126-129]. The detailed mechanism of filiform corrosion is not well understood. For Mg-Dy binary alloys, the filiform corrosion is affected by the content of Dy. The increase in Dy content decreases the filiform corrosion (Fig. 31). After T4 treatment, the content of Dy in Mg matrix increases and the distribution of Dy become more homogenous. Consequently the filiform corrosion is reduced (Fig. 34). In addition, Dy oxidizes and incorporates into the corrosion films and this Dy-containing corrosion film can improve the corrosion resistance [123, 124]. The dissolution of alloying elements influences the occurrence of filiform corrosion was reported for Mg-Zn-Y alloy [128]. In the as-solidified Mg-Zn-Y alloys, increase in the cooling rate delays filiform corrosion. This is attributed to the grain refinement and formation of a supersaturated single Mg solid solution [128].

The T4 heat treatment is an effective approach to improve the corrosion resistance of binary Mg-Dy alloys. The reduction in the amount of second phase particles results in improving the corrosion resistance after T4 treatment. Additionally the influence from the redistribution of Dy in Mg matrix cannot be neglected. Before the T4 treatment the distribution of Dy is inhomogeneous. The distribution of Dy near the dendritic boundaries and the inside of the grain can cause difference in chemical potential between these regions deteriorating the corrosion resistance. After T4 treatment, the distribution of Dy becomes homogeneous, and then the corrosion resistance is enhanced.

Generally, the precipitates formed during the aging treatment increase the corrosion rate of Mg-RE alloys in NaCl solution due to the increase of galvanic corrosion [109, 110, 130]. In this work, large amount of precipitates forms through the Mg matrix in T6-1 condition for Mg-20Dy (Fig. 30). Consequently, the corrosion rate of Mg-20Dy (T6-1) increases significantly. In contrast, only a small amount of precipitates is formed in T6-2 condition for Mg-20Dy alloy and the corrosion rate increases slightly after T6-2 treatment, in comparison with T4 condition (Fig. 30).

6.1.3.2 CCM

The composition of CCM is very close to that of human body fluid. The cell culture condition used in the tests is also very similar to human body environment. Therefore, the *in vitro* corrosion behaviour of Mg-Dy alloys in CCM under cell culture conditions is considered to be close to that *in vivo*.

There are two different roles of Dy in influencing corrosion behaviour of Mg-Dy alloys. Similar to that in NaCl solution, in CCM the galvanic corrosion between the Mg-Dy second phases and the Mg matrix plays an important role in influencing the corrosion morphology and rate. In the as-cast condition, uniform corrosion occurs on Mg-5Dy alloy as little second phase is present. Localized corrosion occurs on all the other alloys due to the galvanic corrosion set up between the second phase and the Mg matrix (Fig. 38). The localized corrosion is increasingly severe with the increase of Dy in alloys, due to the increase in the amount of the second phases. As a result, the corrosion rate is increased with the increase in Dy for Mg-10Dy, Mg-15Dy and Mg-20Dy alloys.

After the T4 treatment, the remaining second phase particles in Mg-20Dy alloy still results in a high corrosion rate (Fig. 41, Fig. 37). However, for the other alloys, Dy is dissolved into the matrix and there is little galvanic corrosion and Dy is incorporated into the corrosion layer, which improves the corrosion resistance of Mg-Dy alloys. Moreover, the amount of Dy in the corrosion layer increases with Dy increase in alloys. Consequently, the corrosion rate reduces with the increase in Dy when Dy amount is less than 15wt.%, despite of the occurrence of the slight localized corrosion on Mg-15Dy alloy.

In T6 condition, although the formation of nano-scale precipitates in Mg-Dy alloys increases the tendency of galvanic corrosion and increases the corrosion rate in 0.9 wt.% NaCl solution, it does not have an adverse influence on the corrosion rate in CCM (Fig. 37). Zhang et al. [131] investigated the influence of ageing treatment on the corrosion rate of extruded Mg-Nd-Zn-Zr alloy in SBF solution. The results also show that ageing treatment does not increase the corrosion rate and even reduces it slightly.

6.1.3.3 Comparison of corrosion in NaCl solution and CCM

Table 19 summarizes the corrosion rate of the Mg-Dy alloys in the NaCl solution and the CCM. For the as-cast alloys in the NaCl solution, the Mg-5Dy alloy shows the highest corrosion rate (7.44 mm/y). However, in the CCM solution, the corrosion rate of Mg-5Dy (F) alloy (0.94 mm/y) is much lower than that in NaCl solution. And the highest corrosion rate (around 2.13) is observed for the Mg-20Dy alloy not the Mg-5Dy alloy. For the T4 treated alloys in the NaCl solution, the corrosion rate is similar for Mg-5Dy, Mg-10Dy and Mg-15Dy. However, in the CCM solution, the corrosion rate is reduced from 1.08 to 0.41 mm/y when Dy increases from 5 to 10 wt.%. After T6-1 treatment, the corrosion behaviour between two solutions are very dissimilar, especially in Mg-20Dy alloy where a large amount of β′ precipitates were observed. After T6-1 treatment, the corrosion rate of the Mg-20Dy alloy increased significantly from 3.12 to 21.52 mm/y in the NaCl solution, while it remains the same in CCM. The tendency of galvanic corrosion between these nano-scale precipitates and Mg matrix is not sensitive in CCM. This could be mainly attributed to the formation of a more protective film in the CCM.

Table 19: Comparison of the corrosion rate of Mg-Dy alloys in NaCl solution and CCM (mm/y).

alloy	Electrolyte	F	T4	T6-1	T6-2
Mg-5Dy	0.9 wt.% NaCl	7.44±0.19	0.96±0.13		--
	CCM	0.94±0.29	1.08±0.09		--
Mg-10Dy	0.9 wt.% NaCl	3.10±1.39	1.33±0.34	1.59±0.14	0.97±0.18
	CCM	0.79±0.08	0.55±0.12	0.44±0.05	0.74±0.09
Mg-15Dy	0.9 wt.% NaCl	4.15±0.48	1.36±0.51	4.03±0.53	1.02±0.11
	CCM	1.09±0.39	0.41±0.07	0.35±0.08	0.46±0.06
Mg-20Dy	0.9 wt.% NaCl	4.12±0.45	3.12±0.75	21.52±6.7	4.15±0.05
	CCM	2.13±1.10	2.36±1.31	2.70±1.44	3.22±0.27

Fig. 80 shows the microstructures of corrosion layer of Mg-20Dy alloy (T6-1 condition) in the 0.9 wt.% NaCl solution and the CCM. In NaCl solution the corrosion film on Mg-20Dy alloy is non-uniform (Fig. 80 (a)) and has a porous structure (Fig. 80 (b)). The EDX analysis indicates that the layer contains 43.85 wt.% O, 54.48 wt.% Mg and 1.67 wt.% Dy, which is mainly consisted of a mixture of MgO and $Mg(OH)_2$ [26]. This film can be easily penetrated by Cl^- ions and is not effective [26]. Consequently, the galvanic corrosion occurs under the corrosion film. In the CCM, a uniform corrosion layer forms on the surface of samples, the cracks observed forms due to dehydration during drying (Fig. 80 (c)). Even at a high magnification, the corrosion layer appeared to be dense and not porous. The EDX analysis reveals that this dense corrosion film contains P, Ca, O and Dy (Fig. 80 (c)). The Dy content is very high, which could be existing as a mixture of $Dy(OH)_3$ and Dy_2O_3.

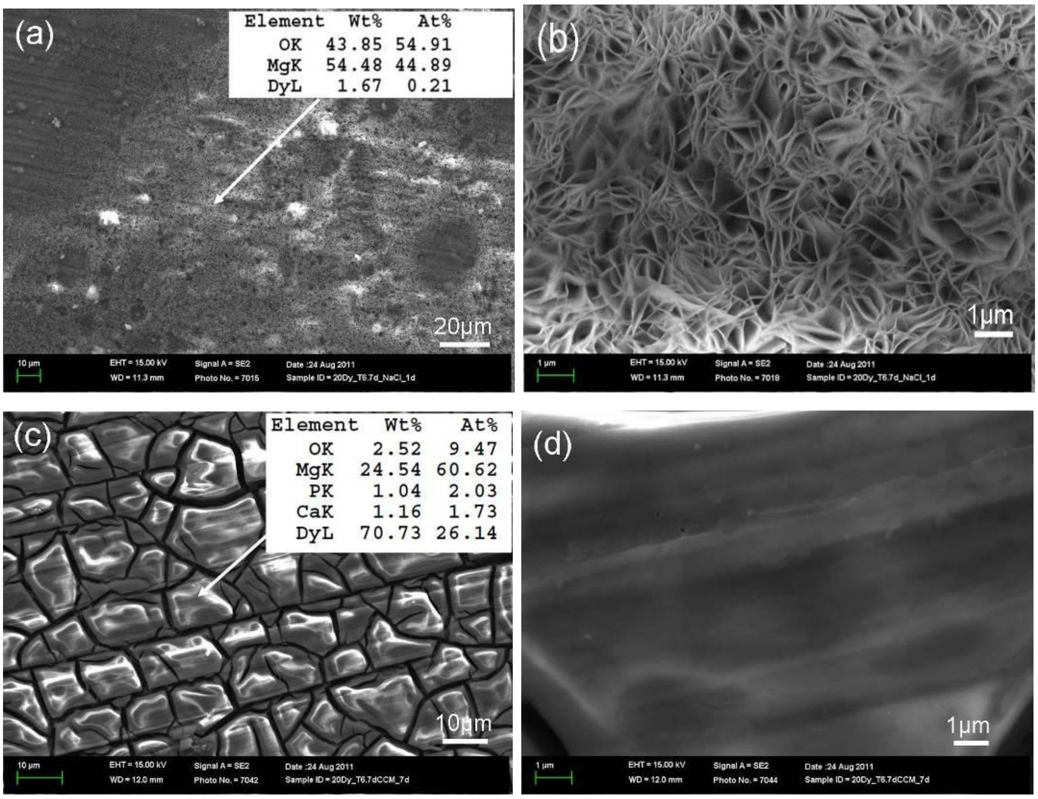

Element	Wt%	At%
OK	43.85	54.91
MgK	54.48	44.89
DyL	1.67	0.21

Element	Wt%	At%
OK	2.52	9.47
MgK	24.54	60.62
PK	1.04	2.03
CaK	1.16	1.73
DyL	70.73	26.14

Fig. 80: Microstructure and composition of corrosion layer of Mg-20Dy alloy in T6-1 condition: (a) low magnification, after immersion in 0.9 wt.% NaCl solution for 1 day; (b) high magnification, after immersion in 0.9 wt.% NaCl solution for 1 day; (c) low magnification, after immersion in CCM for 7 days; (d) high magnification, after immersion in CCM for 7 days. The table shown in the pictures is the EDX composition analysis of the corrosion layer.

In the CCM, this film is more protective than that formed in the NaCl solution, and it hinders the penetration of Cl^- ions. Organic materials such as proteins would adsorb on the surface of the corrosion layer, which significantly reduce the penetration of Cl^- [41, 132]. The corrosion rate in Hank's solution was weakly influenced by the microstructures of high purity Mg and alloys with second phase particles such as AZ91, ZE41, Mg2Zn0.2Mn alloys [133]. The corrosion rates of Pure Mg and Mg alloys in 3% NaCl solution are significantly different, caused by the different micro-galvanic corrosion set ups due to number of phases present [133]. It is concluded that nano-scale precipitates form during ageing has no negative effect on the bio-corrosion rate of the Mg-Dy alloys.

The corrosion rates of the Mg-Dy alloys in the NaCl solution and CCM show that there is no link between corrosion in only Cl^- environment and bio corrosion environment. Moreover, It was reported that the corrosion rate of Mg alloys in NaCl solution is different from that of *in vivo* corrosion [2]. Thus, corrosion behaviour in a NaCl solution should not be used to predict the corrosion rate of Mg alloys in biological environments. Based on this work, the trend between corrosion in NaCl and in biological corrosion do not show any parallels.

The choice of corrosion environment is crucial for the experimental results. Physiological corrosion is still an obstacle and lacking a systematic approach requiring a multidisciplinary investigation. As a first approach, the application of CCM under cell culture conditions seems to be appropriate towards a more predictive *in vitro* environment.

6.1.4 Bio-Corrosion layer

During the *in vivo* degradation of Mg alloys, the corrosion layer forms an interface between Mg alloy and body fluids as well as body tissues. It plays a very important role in determining both the corrosion behaviour and the biocompatibility of Mg alloys. On one hand, the corrosion layer can act as a protective layer to reduce the degradation rate of Mg alloys, depending mainly on its composition and microstructure. On the other hand, the surface of corrosion layer is in direct contact with tissues, cells, body fluid and bone, thus the biocompatibility is determined also by the morphological and compositional characteristics of the corrosion.

In Cl^- ion containing aqueous solution, the corrosion of magnesium occurs through following reactions [26]:

$Mg \rightarrow Mg^{2+} + 2e^-$ Equation 5

$2H_2O + 2e^- \rightarrow H_2 + 2OH^-$ Equation 6

$Mg^{2+} + 2(OH)^- \rightarrow Mg(OH)_2$ Equation 7

Based on the above reactions, $Mg(OH)_2$ forms in the corrosion layer initially and then transforms into more soluble $MgCl_2$ in the presence of aggressive chloride ions through following reaction:

$Mg(OH)_2 + 2Cl^- \rightarrow MgCl_2 + 2OH^-$ Equation 8

During the corrosion of Mg alloys large amount of $Mg(OH)_2$ transforms into Mg ions and is released into the electrolyte, and only a part of $Mg(OH)_2$ remains in the corrosion layer.

Dy metal is quite electropositive, and has a similar standard potential (-2.35 V) to Mg (-2.37 V). The main corrosion product for Dy is Dy_2O_3 and a small amount of $Dy(OH)_3$ as detected by XPS (Fig. 52). The following reaction may be deduced.

$2Dy + 3H_2O \rightarrow Dy_2O_3 + 3H_2$ Equation 9

$2Dy + 6H_2O \rightarrow 2\ Dy(OH)_3 + 3H_2$ Equation 10

Dy_2O_3 is insoluble in water. The solubility product constant (Ksp) for $Dy(OH)_3$ is 1.4×10^{-22}, which is much smaller than that of $Mg(OH)_2$ (5.61×10^{-12}) [134]. Based on the solubility above, Dy_2O_3 and $Dy(OH)_3$ are more likely to remain in the corrosion layer than $Mg(OH)_2$ due to the lower solubility. This results in the enrichment of Dy in the corrosion layer as indicated in Fig. 48 and Fig. 49. The enhancement of corrosion resistance in Mg alloys by addition of RE has been observed previously [135, 136]. The main reason for this is that RE converts into stable RE oxide and/or RE hydroxide layer during the corrosion. The RE-containing layer plays better role than $Mg(OH)_2$ layer in reducing corrosion of Mg alloys [126, 135, 136]. Therefore, the enrichment of Dy_2O_3 and $Dy(OH)_3$ in the corrosion layer could be beneficial in improving the corrosion resistance of the corrosion layer.

Previous studies show the following reaction occurs when Mg is exposed to a solution containing Ca^{2+}, $H_2PO_4^{-}$ and HPO_4^{2-} ions [32, 137].

$xMg^{2+} + yCa^{2+} + zPO_4^{3-} \rightarrow Ca_xMg_y(PO_4)_z$ Equation 11

At the beginning of the corrosion process, equation 11 is dynamically balanced. The formation and dissolution of $Ca_xMg_y(PO_4)_z$ precipitates happens at the same rate in the electrolyte. As the immersion time increases, the amount of released Mg^{2+} increases, which provides driving force for the formation of $Ca_xMg_y(PO_4)_z$. For Mg-10Dy alloy, a dense and homogeneous corrosion layer containing Dy_2O_3/ $Dy(OH)_3$ forms during corrosion. This corrosion layer could reduce permeability of Ca^{2+} and PO_4^{3-} ions to the corrosion interface. Ca^{2+} and PO_4^{3-} ions are mainly in the corrosion medium and corrosion surface. As a result, $Ca_xMg_y(PO_4)_z$ precipitates form mainly on the surface of samples where a high concentration of Mg^{2+} is prevalent and sufficient Ca^{2+} and PO_4^{3-} ions are present. Higher P and Ca content were found in the surface of corrosion layer (Fig. 48 and Fig. 49), which agrees with the above analysis. Pitting corrosion causes the Mg^{2+} concentration to increase dramatically in the pitting region.

This strongly drives the equation 11 toward the formation of $Ca_xMg_y(PO_4)_z$. Large amount of $Ca_xMg_y(PO_4)_z$ precipitates form and pile on the pitting corrosion areas as shown in Fig. 44 (a). Phosphate is effective at reducing pitting corrosion for Mg alloys due to the formation of phosphate layer [36]. Therefore, pitting corrosion is inhibited with the formation of piled corrosion products and uniform corrosion continues after immersion for 3 days (Fig. 44 (b)).

Under cell culture conditions, carbon dioxide causes the formation of H_2CO_3 which inhibits the increase of pH value through the following reactions [38].

$H_2O + CO_2 \rightarrow H_2CO_3$ Equation 12

$Mg + H_2CO_3 \rightarrow MgCO_3 + H_2$ Equation 13

This results in the formation of $MgCO_3$ on the specimens. The solubility of $MgCO_3$ (220 mg/l) is about 19-fold higher than that of $Mg(OH)_2$ (12 mg/l). Therefore the precipitation and incorporation of $MgCO_3$ into the corrosion layer will only take place after the aqueous solution is saturated with $MgCO_3$. After 1 day and 3 days immersion, almost all the formed $MgCO_3$ dissolves into the electrolyte. As a result, C is found only at the surface of the corrosion layer (Fig. 51 and Fig. 48). With the increase of immersion time, more and more $MgCO_3$ forms and the electrolyte becomes saturated. After 28 d immersion, $MgCO_3$ is identified to be the main corrosion product (Fig. 53). Similar result is also obtained in a previous study [38], which reports a large amount of $MgCO_3$ forms in the corrosion layer with a thickness of ~ 80 µm.

There are 2 stages on the growth rate of the thickness of corrosion layer (Fig. 45). In stage I, the corrosion resistance of corrosion layer increases with the increase of corrosion layer thickness. Hence, then growth rate of corrosion layer reduces gradually. At stage II, the corrosion product $MgCO_3$ becomes saturated in the electrolyte and accumulates on the sample constantly. As a result, the thickness of corrosion layer increases rapidly and $MgCO_3$ is identified to be the main corrosion product after 28 d immersion (Fig. 53). Many studies have shown that large amount of C and O is observed in the corrosion layer of Mg-based implants after long term *in vivo* tests in animal bones [100, 102, 138, 139]. This could be due to the buffering effect of CO_2 and formation of $MgCO_3$ in the environment with limited body fluid.

6.1.5 Biocompatibility

The biocompatibility of the corrosion products is one of the key points for successful developing alloys. An accumulation of Dy in the corrosion layer in contrast to the bulk material is observed (Fig. 46). This accumulation did not induce cytotoxic effects *in vitro*, which is shown by the direct cell adhesion tests. Actually, a number of works have already shown that Dy has a good biocompatibility. LD50 (half-lethal dose) of $DyCl_3$ in mice was determined at 585 mg/kg by intraperitoneal injection [90]. Dy complexes are also used as contrast medium for MRI. Dy applied *in vivo* exhibited an increase in its concentration in spleen and lungs with increasing doses, while its concentration in kidneys and blood decreased, and hepatotoxicity was not observed [77]. *In vitro* cytotoxicity studies in BEAS-2B (human bronchial epithelial cells) and L929 cells indicate that Dy_2O_3 have no appreciable toxicity at a concentration of up to 1000 µg/mL [140]. Feyerabend et al. [3] also showed that Dy is the best tolerated RE element based on *in vitro* study. Also in a study with primary human smooth muscle cells exposed to RE-chlorides, Dy was tolerated in a broad concentration range [141]. Furthermore, dysprosium (165) hydroxide macroaggregates are developed to utilize the advantages of dysprosium 165 in radiation synovectomy of certain forms of arthritis [142, 143]. Therefore, based on the above discussion the effect of a small amount of Dy in Mg alloys should be tolerable.

However, there is a naturally occurring accumulation of Dy in human bones [144], and it was observed that dysprosium can replace calcium in hydroxyapatite [145]. Before applying rare-earth based alloys therefore more insight in their influence on bone structure and metabolism should be obtained.

6.2 Mg-Dy-Gd-Zr alloys

6.2.1 Microstructure and age hardening behaviour

Dy and Gd do not react with each other and they have similar chemical properties [134]. Hence, they play the similar role in the experimental alloys. Based on the Mg–Dy and Mg-Gd binary phase diagram as shown in Fig. 9 and Fig. 10, the maximum solid solubility of Dy (25.3 wt.%) and Gd (23.5 wt.%) in Mg matrix is similar at eutectic temperature. However, their solubility decreases at different rates with the decrease in temperature. The solid solubility of Dy reduces gradually with the decrease in temperature, to about 10 wt.% at 200 °C (Fig. 9). In contrast, the solid solubility of Gd in Mg reduces dramatically with the decrease in temperature, to about 3wt.% at 200 °C (Fig. 10). As a result, Gd is more inclined to form precipitates than Dy during solidification. This could be the reason that the amount of second phase increases with the increase in Gd amount in as-cast alloys, despite the total amount of alloying elements remain constant (Fig. 63). To confirm this, it is necessary to develop the ternary phase diagram of Mg-Dy-Gd system which is not available so far.

EDX analysis showed that these second phases are composed of Mg, Dy and Gd. The content of Mg is constant (~86%) in the second phases of all alloys. The Dy and Gd content in the second phases depends on their content in the different alloys, but the total amount of RE (Dy+Gd) remains the same in the second phases of all alloys. The size of the second phase is not big enough to obtain an accurate result from EDX analysis. As a result, Mg content is higher than its true value as some of the Mg signals are from the α-Mg matrix and not second phase. Based on the binary Mg-Dy and Mg-Gd phase diagrams, the only expected phases are $Mg_{24}Dy_5$ and Mg_5Gd for binary Mg-Dy and Mg-Gd alloys. Therefore, the second phases in Mg-Dy-Gd alloys are identified approximately as $Mg_5(Dy+Gd)$. Generally, Mg_5RE phase forms in many Mg-RE alloys, where RE represents a mixture of the rare earth alloying elements. The ratio of the rare earth elements in the second phase varies in different alloys. It is reported that in Mg-7Gd-2Nd alloy the Nd : Gd ratio is close to 1:1 in second phases, suggesting a stoichiometry of $Mg_5(Nd_{0.5}Gd_{0.5})$ [146]. In Mg-7Dy-2Nd alloy the Nd concentration is significantly higher than that of Dy, suggesting a stoichiometry near $Mg_5(Nd_{0.7}Dy_{0.3})$ [146]. In Mg-4Y-2Nd alloy the Nd : Y ratio is close to 1:2, suggesting a stoichiometry near $Mg_5(Nd_{0.33}Y_{0.67})$ [146].

Little age hardening was observed for D10K alloy. This is due to the high solubility (~ 10wt.%) of Dy at 200 °C in Mg matrix, causing all the Dy to remain in the α-Mg matrix rather than form precipitates. Gd has a lower solubility (~ 3wt.%) than Dy at 200 °C. Thus, it is easier for Gd to form precipitates than Dy in Mg-Dy-Gd-Zr alloys during ageing. With the increase in Gd content in Mg-Dy-Gd-Zr alloys, the amount of β′ precipitates increases and in return the age hardening behaviour becomes more significant. Better age hardening response is obtained with increasing addition of Gd. To further understand the interaction between Dy and Gd, the ternary phase diagram needs to be developed as mentioned before. Apps et al. [112] investigated the age hardening behaviour of Mg-7Dy-2Nd and Mg-7Gd-2Nd alloys, and they also found that Gd is more effective in strengthening than Dy. The peak Vickers hardness of 104 Hv was achieved for the Mg-7Gd-2Nd alloy, while it only reached 86 Hv for Mg-7Dy-2Nd alloy.

6.2.2 Mechanical properties

Table 20 summarizes the mechanical properties of Mg-Dy-Gd-Zr alloys. In the as-cast alloys, grain boundary strengthening, solid solution strengthening as well as precipitate strengthening contributes to the total strength. Since all alloys have a similar grain size, grain boundary strengthening contribution is similar. With the increase of Gd, the amount of precipitates increases and amount of alloying elements decreases in the α-Mg matrix and segregation area. Therefore, the substitution of Dy with Gd increases the precipitates strengthening while reducing the solid strengthening.

After T4 treatment, precipitate strengthening is negligible as only very few particles remain in the α-Mg matrix. The effect of grain boundary strengthening is similar in all alloys due to the similar grain sizes. As a result, solid solution strengthening is the only factor which contributes to the different values of hardness and yield strength observed. The total amount of alloying element in the alloys is similar, but with the increase in Gd the hardness and yield strength increase. This indicates Gd has a better solution strengthening effect than Dy. The atomistic simulation has shown that Gd is more effective than Dy in improving bulk modulus of Mg alloys [147]. Furthermore, the Vickers hardness of Mg-7Gd-2Nd alloy is 20% higher than that of Mg-7Dy-2Nd alloy in T4 condition [112].

During T6 treatment, the decomposition of the supersaturated α-Mg solid solution occurs and β′ precipitates form (Fig. 68). These precipitates are resistant to dislocation movement and contribute to precipitates strengthening. The high density of intrinsically strong, plate-shaped precipitates with prismatic habit planes and large aspect ratios contributes to significant precipitate strengthening effects [122]. Different degree of improvement in TYS and CYS are obtained after T6 as listed in Table 20, but these precipitates deteriorate the ductility of the alloys. Thus, both of the elongation and compressibility are reduced after T6 treatment, especially for DG28K alloy in which large amount of β′ precipitates are observed.

Table 20: Comparison of mechanical properties in different conditions. (T6-T4) is the value change of mechanical properties from T4 condition T6 condition.

condition	alloy	TYS	UTS	Elong.	CYS	UCS	Comp. Duct.
As-cast	D10K	107±2.5	189±2.0	21.7±1.5	96.0±0.9	321.3±8.9	20.7±1.0
	DG82K	113.3±2.0	199.0±2.1	21.5±2.8	103.0±2.5	332.9±5.2	18.9±1.3
	DG55K	118.9±1.7	207.8±3.1	17.6±1.6	110.2±3.3	337.6±7.9	17.9±1.4
	DG28K	123.3±1.7	218.3±4.8	16.2±3.4	120.8±3.0	347.4±2.1	15.6±1.4
T4	D10K	104.6±1.9	187.8±1.3	24.1±1.0	98.3±5.7	310.8±12.8	23.0±1.4
	DG82K	111.1±2.1	198.4±1.5	22.1±2.8	109.1±3.0	305.3±10.9	18.4±0.3
	DG55K	121.8±1.1	209.2±3.1	17.6±1.8	112.7±3.4	312.7±6.3	18.7±1.7
	DG28K	122.5±5.2	214.6±8.6	17.8±1.7	125.8±6.3	302.9±27.2	15.7±0.9
T6	D10K	99.8±1.9	195.1±1.9	22.2±2.0	108.1±8.1	289.9±2.5	19.1±2.1
	DG82K	111.6±2.8	211.7±2.3	21.0±0.4	125.2±17.6	303.5±5.5	17.7±1.0
	DG55K	188.3±0.6	309.5±1.5	11.8±1.6	189.6±7.4	357.1±4.9	9.2±1.7
	DG28K	211.6±0.7	353.9±5.4	7.8±2.1	241.2±23.6	423.0±9.2	6.8±1.2
(T6-T4)	D10K	-4.8	7.3	-1.9	9.8	-20.9	-3.9
	DG82K	0.5	13.3	-1.1	16.1	-1.8	-0.7
	DG55K	66.5	100.3	-5.8	76.9	44.4	-9.5
	DG28K	89.1	139.3	-10	115.4	120.1	-8.9

In summary, mechanical properties are tailored in a wide range by adjusting the alloy composition and using heat treatment, Table 20. The TYS varies between 99.8 and 211.6 MPa, and the CYS varies between 96 and 241.2 MPa. The highest UTS is 353.9 MPa and the highest UCS even reaches 423 MPa. The elongation to fracture is at a minimum value of around 7.8%, while it reaches a maximum value at 24.1%. Therefore, for different applications different compositions and heat treatments could be adopted, depending on the mechanical properties required. For example, cardiovascular stents need good ductility but need not high yield strength. Thus, the D10K alloy, with the TYS of 104.6 MPa and elongation of 24.1% in T4 condition, may be used. Load bearing bone plates and screws need high yield strength but need not very good ductility of materials. Thus, the DG55K alloy, with the TYS of 188.3 MPa and elongation of 11.8% in T6 condition, may be used.

6.2.3 Corrosion

Based on the corrosion behaviour of Mg-Dy alloys in 0.9 wt.% NaCl and CCM solution, the corrosion rate and trend is different between the two solutions. As discussed before, CCM is more closely resembles physiological conditions and the corrosion behaviour in CCM and NaCl solution is completely unparallel. Therefore CCM was used solely for the corrosion tests.

The electrochemical potential of Mg–Dy-Gd intermetallics has not been reported so far, even for binary Mg-Gd intermetallics. It is reported that corrosion is accelerated by Mg_5Gd intermetallics in binary Mg-Gd alloys [34]. Moreover, in Mg-Gd-Y alloys $Mg_5(Gd+Y)$ intermetallics act as cathodes and form galvanic corrosion couples with α-Mg matrix, accelerating corrosion [109, 110]. Elements Dy, Gd and Y have similar electrochemical potential and chemical properties. Thus, it may be deduced that the “$Mg_5(Gd+Dy)$” phase is also cathodic compared to α-Mg matrix and leads to galvanic corrosion.

Similar to Dy the negative electrochemical potential of Gd (-2.4 V) is close to that of Mg (-2.37 V). This indicates that Gd would not cause micro-galvanic corrosion with the Mg matrix when it exists in solid solution rather than second phases. In Gd-containing alloys, Gd transforms to $Gd(OH)_3$ and is incorporated into corrosion layer during corrosion [148]. This improves the corrosion resistance and the protective nature of the corrosion layer. Kiryuu et al. [149] also indicated that Gd could stabilize the corrosion layer of Mg-10Gd-3Nd alloy.

In this work, the amount of intermetallic phases increase with the increase in Gd content in the as-cast alloys (Fig. 63). As a result, with increased Gd content the corrosion rate increases slightly (Fig. 73), and pitting corrosion was increasingly apparent (Fig. 74). This could be attributed to the galvanic corrosion between the intermetallic phases and α-Mg matrix.

After T4 treatment, only very few and small precipitates remain in the α-Mg matrix (Fig. 65). Thus the galvanic corrosion is largely reduced, which eliminates the pitting and localized corrosion. No apparent pitting corrosion is observed for any alloy in the macro corrosion morphology (Fig. 74). The Dy and Gd amounts in the α-Mg matrix increase due to the dissolution of the second phases and the segregation area. The distribution of alloying elements becomes more homogeneous in the alloys. During the corrosion, Dy and Gd are oxidized to RE_2O_3 and / or $RE(OH)_3$, and the homogeneous distribution of Dy and Gd makes it easy to form a uniform Dy/Gd-containing layer. This improves the protective nature and the corrosion resistance of the corrosion layer as discussed. Both the decrease in galvanic corrosion and the improvement of the corrosion resistance result in the reduction of the corrosion rate after T4 treatment.

After T6 treatment, nano-scale β′ precipitates forms. In DG28K alloy, large number density of β′ precipitates distribute all over the matrix. However, these β′ precipitates show no adverse effect on the corrosion rate in CCM.

6.2.4 Biocompatibility

Compared to the corrosion layer composition of the Mg-10Dy alloy, the enrichment of Gd was found in the corrosion layer of Mg-Dy-Gd-Zr alloys. Gd has similar chemical properties to Dy [134]. After corrosion, Gd transforms into Gd_2O_3 and $Gd(OH)_3$ and accumulates in the corrosion layer. However, this corrosion layer shows no cytotoxicity on the human osteoblast cells (Fig. 79). Based on the previous studies, the acute toxicity of Gd is only moderate. The intraperitoneal LD50 dose of $GdCl_3$ is 550 mg/kg in mice, and $GdNO_3$ induces acute toxicity at a concentration of 300 mg/kg in mice and 230 mg/kg in rats, respectively [85, 150]. The cytotoxicity tests of $GdCl_3$ in osteoblast like cells showed that Gd would be a suitable alloying element for the designation of Mg-based implant [3].

Gd-based contrast agents are widely used as the contrast medium in magnetic resonance imaging [114, 151, 152], especially Gd_2O_3 nano particles [153, 154]. $Gd(OH)_3$ was investigated for its possible use in imaging and tracking of cells and tissues [155]. No significant cytotoxic effect is observed for $Gd(OH)_3$ in *in vitro* study using human colon adenocarcinoma and human lung epithelial cells [155]. However, Gd ions released by transmetallation induces nephrogenic systemic fibrosis in patients with renal failure, though not in healthy patients [156]. Gd has also been observed to have a certain retention rate in bone prior to redistribution to spleen and liver [157]. Although it is found that the Gd content in bone increases with age growing due to the accumulation [144], no negative effect of Gd on bone is reported so far. Based on above discussion, a small amount of Gd used as alloying element would not evoke systemic effects and can be tolerable by human body. However, the influence of Gd accumulation on bone structure and metabolism needs further investigation before its application.

6.2.5 Effects of Zr on Mg-10Dy alloy

Due to the good biocompatibility of Zr [71-74], it is added as a grain refinement agent. The influence of Zr on the mechanical and corrosion properties will be discussed by comparing the properties of Mg-10Dy and Mg-10Dy-0.2Zr alloys.

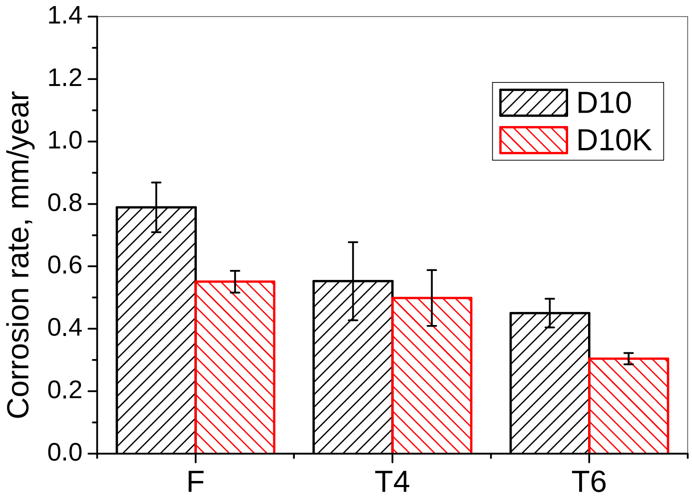

Fig. 81: Comparison of the corrosion rate of Mg-10Dy and Mg-10Dy-0.2Zr alloy

The effects of Zr on the corrosion rate of Mg-10Dy alloys are shown in Fig. 81. The corrosion rate of Mg-10Dy-0.2Zr alloy is around 10~30% lower than that of Mg-10Dy alloy in different conditions. It is reported that the addition of Zr reduces the corrosion rate of other Mg alloys [158, 159]. The beneficial effect of Zr on corrosion of Mg-10Dy alloy is likely caused by the following two mechanisms. Firstly, Zr can reduce the amount of Fe impurity by forming insoluble precipitates and settling down to the bottom of ingots. This is reconfirmed in this work. The Fe content in Mg-10Dy-0.2Zr alloy (0.002 wt.%) is less than that in Mg-10Dy alloy (0.005 wt.%). In addition, grain refinement can also reduce the corrosion rate of Mg alloys slightly [160, 161].

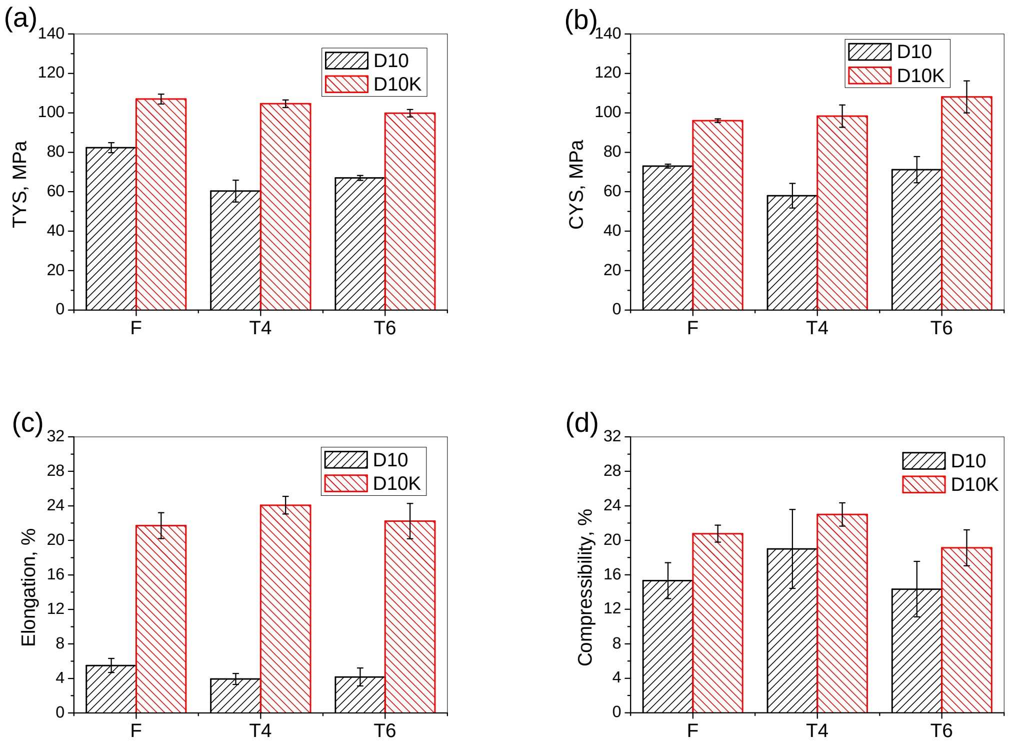

Fig. 82: Comparison of mechanical properties of Mg-10Dy and Mg10Dy-0.2Zr alloy

The comparison of mechanical properties between Mg-10Dy and Mg-10Dy-0.2Zr alloys is shown in Fig. 82. In all the conditions, the TYS and CYS of Mg-10Dy-0.2Zr alloy are about 20-50% higher than those of Mg-10Dy alloy. The elongation increases apparently from around 5% to around 22% and the compressibility also improves slightly. The enhancement of mechanical properties is attributed to the grain refinement effects of Zr. With the addition of Zr, the grain size of Mg-10Dy alloy reduces from 610 to 60 µm, contributing to the increase of yield strength according to Hall-Petch law [162]. When grain size is larger than 10 µm, grain refinement improves ductility by increasing basal slip systems and twins [163].

7 Summary

Based on the good biocompatibility of Dy and Gd elements and promising Mg-Dy and Mg-Gd phase diagrams, Mg-Dy alloys and 10(Dy+Gd)-0.2Zr alloys were designed and investigated in this work. The microstructure, mechanical and corrosion properties of these alloys can be tailored by adjusting the alloy composition and using heat treatment. In binary Mg-Dy alloys, the Mg-10Dy alloy shows the best corrosion properties (low corrosion rate and uniform corrosion morphology). Considering both the mechanical and the corrosion properties, the Dy amount is optimized at 10 wt.%. The mechanical and corrosion properties for the Mg-10Dy alloy are further enhanced by combining Dy with Gd and adding Zr as grain refinement agent. Finally, novel Mg-10(Dy+Gd)-0.2Zr alloys with flexible mechanical properties, low corrosion rate and acceptable cytocompatibility are developed. The influence of Dy and Gd on the microstructure, mechanical properties, corrosion behaviour and cytotoxicity is summarized as following.

- **Microstructure**

  In the as-cast condition, the microstructure consists of α-Mg matrix, segregation area of alloying elements and second phases ($Mg_{24}Dy_5$ in Mg-Dy alloys and approximately Mg_5RE in Mg-10(Dy+Gd)-0.2Zr alloys). After T4 treatment, alloying elements segregation is eliminated completely, and very few second phases are left. β′ ($Mg_{13}RE_3$) precipitates are the main phase at peak aged condition at 200 °C and they distribute homogeneously in the matrix.

- **Mechanical properties**

  Mechanical properties are tailored in a wide range by adjusting the alloy composition and by heat treatment. The TYS varies between 99.8 and 211.6 MPa, and the CYS varies between 96-241.2 MPa. The highest UTS is 353.9 MPa and the highest UCS reaches 423 MPa. The elongation to fraction is at a minimum value of around 7.8%, while it reaches a maximum value at 24.1%.

- **Corrosion properties**

  The second phases in Mg-Dy and Mg-10(Dy+Gd)-0.2Zr alloys cause galvanic corrosion between these phases and α-Mg matrix. This leads to severe pitting and localized corrosion. T4 treatment improves the corrosion resistance of alloys due to the elimination of second phases as well as the homogenization of microstructure. Nano-scale precipitates formed during ageing treatment have no negative effects on bio-corrosion rate in CCM.

- **Composition of bio-corrosion layer**

  In the bio-corrosion layer, the elemental distribution varies from the surface of corrosion layer to the corrosion interface between matrix and corrosion layer. Enrichment of Dy and Gd was observed in the corrosion layer. Much more Ca and P elements distribute in the surface of corrosion layer than those inside the corrosion layer. C and N (protein) are also mainly observed on the surface of corrosion layer.

- **Cytotoxicity**

  The accumulation of Dy and Gd in the corrosion layer does not induce cytotoxic effects on human osteoblasts which show high viability and good adhesion behaviour after 3 and 7 days culture on tested alloys.

8 Outlook

- Extrusion processing is an effective way in adjusting mechanical and corrosion properties of Mg alloys. Hence, it is necessary to investigate the different extrusion parameters and following heat treatment process on the mechanical and corrosion behaviour of the developed alloys.

- For different medical applications, more comprehensive *in vitro* cytocompatibility tests are recommended such as tests with different cell types and further gene expression experiments. Moreover, the *in vitro* stress corrosion behaviour should also be investigated.

- The results of *in vivo* study are always the most reliable one before the tests in human body. Future work should include the *in vivo* study of the degradation behaviour of the developed alloys in small and big animals.

9 References

[1] Witte F, Kaese V, Haferkamp H, Switzer E, Meyer-Lindenberg A, Wirth CJ, Windhagen H. In vivo corrosion of four magnesium alloys and the associated bone response. Biomaterials 2005;26:3557.

[2] Witte F, Fischer J, Nellesen J, Crostack HA, Kaese V, Pisch A, Beckmann F, Windhagen H. In vitro and in vivo corrosion measurements of magnesium alloys. Biomaterials 2006;27:1013.

[3] Feyerabend F, Fischer J, Holtz J, Witte F, Willumeit R, Drückere H, Vogt C, Hort N. Evaluation of short-term effects of rare earth and other elements used in magnesium alloys on primary cells and cell lines. Acta Biomater. 2010;6:1834.

[4] Zeng RC, Dietzel W, Witte F, Hort N, Blawert C. Progress and challenge for magnesium alloys as biomaterials. Adv. Eng. Mater. 2008;10:B3.

[5] Kirkland NT, Lespagnol J, Birbilis N, Staiger MP. A survey of bio-corrosion rates of magnesium alloys. Corros. Sci. 2010;52:287.

[6] Staiger MP, Pietak AM, Huadmai J, Dias G. Magnesium and its alloys as orthopedic biomaterials: A review. Biomaterials 2006;27:1728.

[7] Jacobs JJ, Gilbert JL, Urban RM. Corrosion of metal orthopaedic implants. J. Bone Joint Surg.-Am. Vol. 1998;80A:268.

[8] Jacobs JJ, Skipor AK, Patteson LM, Hallab NJ, Paprosky WG, Black J, Galante JO. Metal release in patients who have has a primary total hip arthroplasty - A prospective, controlled, longitudinal study. J. Bone Joint Surg.-Am. Vol. 1998;80A:1447.

[9] Jacobs JJ, Hallab NJ, Skipor AK, Urban RM. Metal degradation products - A cause for concern in metal-metal bearings? Clin. Orthop. Rel. Res. 2003:139.

[10] Lhotka C, Szekeres T, Steffan I, Zhuber K, Zweymuller K. Four-year study of cobalt and chromium blood levels in patients managed with two different metal-on-metal total hip replacements. Journal of Orthopaedic Research 2003;21:189.

[11] Upadhyay D, Panchal MA, Dubey RS, Srivastava VK. Corrosion of alloys used in dentistry: A review. Mater. Sci. Eng. A-Struct. Mater. Prop. Microstruct. Process. 2006;432:1.

[12] Dearnley PA. A brief review of test methodologies for surface-engineered biomedical implant alloys. Surf. Coat. Technol. 2005;198:483.

[13] Hermawan H, Dubé D, Mantovani D. Developments in metallic biodegradable stents. Acta Biomater. 2010;6:1693.

[14] Witte F, Hort N, Vogt C, Cohen S, Kainer KU, Willumeit R, Feyerabend F. Degradable biomaterials based on magnesium corrosion. Curr. Opin. Solid State Mater. Sci. 2008;12:63.

[15] Witte F. The history of biodegradable magnesium implants: A review. Acta Biomater. 2010;6:1680.

[16] Erbel R, Di Mario C, Bartunek J, Bonnier J, de Bruyne B, Eberli FR, Erne P, Haude M, Heublein B, Horrigan M, Ilsley C, Bose D, Koolen J, Luscher TF, Weissman N, Waksman R, Investigators P-A. Temporary scaffolding of coronary arteries with bioabsorbable magnesium stents: a prospective, non-randomised multicentre trial. Lancet 2007;369:1869.

[17] Saris NEL, Mervaala E, Karppanen H, Khawaja JA, Lewenstam A. Magnesium - An update on physiological, clinical and analytical aspects. Clin. Chim. Acta 2000;294:1.

[18] Rude RK, Gruber HE, Wei LY, Frausto A, Mills BG. Magnesium deficiency: Effect on bone and mineral metabolism in the mouse. Calcif. Tissue Int. 2003;72:32.

[19] Hartwig A. Role of magnesium in genomic stability. Mutat. Res.-Fundam. Mol. Mech. Mutagen. 2001;475:113.

[20] Vormann J. Magnesium: nutrition and metabolism. Molecular aspects of medicine 2003;24:27.

[21] Revell PA, Damien E, Zhang XS, Evans P, Howlett CR. The effect of magnesium ions on bone bonding to hydroxyapatite coating on titanium alloy implants. In: Barbosa MA, Monteiro FJ, Correia R, Leon B, editors. Bioceramics, Vol 16, vol. 254-2. Zurich-Uetikon: Trans Tech Publications Ltd, 2004. p.447.

[22] Zreiqat H, Howlett CR, Zannettino A, Evans P, Schulze-Tanzil G, Knabe C, Shakibaei M. Mechanisms of magnesium-stimulated adhesion of osteoblastic cells to commonly used orthopaedic implants. Journal of Biomedical Materials Research 2002;62:175.

[23] Yamasaki Y, Yoshida Y, Okazaki M, Shimazu A, Kubo T, Akagawa Y, Uchida T. Action of FGMgCO(3)Ap-collagen composite in promoting bone formation. Biomaterials 2003;24:4913.

[24] Yamasaki Y, Yoshida Y, Okazaki M, Shimazu A, Uchida T, Kubo T, Akagawa Y, Hamada Y, Takahashi J, Matsuura N. Synthesis of functionally graded $MgCO_3$ apatite accelerating osteoblast adhesion. Journal of Biomedical Materials Research 2002;62:99.

[25] Nagels J, Stokdijk M, Rozing PM. Stress shielding and bone resorption in shoulder arthroplasty. J. Shoulder Elbow Surg. 2003;12:35.

[26] Song G, Atrens A. Understanding Magnesium Corrosion: a Framework for Improved Alloy Performance. Adv. Eng. Mater. 2003;5:837.

[27] Makar GL, Kruger J. Corrosion of Magnesium. Int. Mater. Rev. 1993;38:138.

[28] Shaw B. Corrosion resistance of magnesium alloys. ASM Handbook 2003;13 A Corrosion: Fundamentals, testing and protection (#06494G).

[29] Liu M, Uggowitzer PJ, Nagasekhar AV, Schmutz P, Easton M, Song GL, Atrens A. Calculated phase diagrams and the corrosion of die-cast Mg-Al alloys. Corros. Sci. 2009;51:602.

[30] Atrens A, Liu M, Zainal Abidin NI. Corrosion mechanism applicable to biodegradable magnesium implants. Materials Science and Engineering: B.

[31] Mueller WD, Nascimento ML, de Mele MFL. Critical discussion of the results from different corrosion studies of Mg and Mg alloys for biomaterial applications. Acta Biomater. 2010;6:1749.

[32] Yang L, Zhang E. Biocorrosion behavior of magnesium alloy in different simulated fluids for biomedical application. Mater. Sci. Eng. C 2009;29:1691.

[33] Xin YC, Hu T, Chu PK. Influence of Test Solutions on In Vitro Studies of Biomedical Magnesium Alloys. Journal of the Electrochemical Society 2010;157:C238.

[34] Hort N, Huang Y, Fechner D, Stomer M, Blawert C, Witte F, Vogt C, Drüker H, Willumeit R, Kainer KU, Feyerabend F. Magnesium alloys as implant materials - Principles of property design for Mg-RE alloys. Acta Biomater. 2010;6:1714.

[35] Xin Y, Hu T, Chu PK. In vitro studies of biomedical magnesium alloys in a simulated physiological environment: A review. Acta Biomater. 2011;7:1452.

[36] Xin YC, Huo KF, Tao H, Tang GY, Chu PK. Influence of aggressive ions on the degradation behavior of biomedical magnesium alloy in physiological environment. Acta Biomater. 2008;4:2008.

[37] Yamamoto A, Hiromoto S. Effect of inorganic salts, amino acids and proteins on the degradation of pure magnesium in vitro. Mater. Sci. Eng. C-Biomimetic Supramol. Syst. 2009;29:1559.

[38] Willumeit R, Fischer J, Feyerabend F, Hort N, Bismayer U, Heidrich S,

Mihailova B. Chemical surface alteration of biodegradable magnesium exposed to corrosion media. Acta Biomater. 2011;7:2704.
[39] Gu XN, Zheng YF, Chen LJ. Influence of artificial biological fluid composition on the biocorrosion of potential orthopedic Mg-Ca, AZ31, AZ91 alloys. Biomedical Materials 2009;4.
[40] Liu C, Xin Y, Tian X, Chu PK. Degradation susceptibility of surgical magnesium alloy in artificial biological fluid containing albumin. J. Mater. Res. 2007;22:1806.
[41] Liu CL, Wang YJ, Zeng RC, Zhang XM, Huang WJ, Chu PK. In vitro corrosion degradation behaviour of Mg–Ca alloy in the presence of albumin. Corros. Sci. 2010;52:3341.
[42] Levesque J, Hermawan H, Dube D, Mantovani D. Design of a pseudo-physiological test bench specific to the development of biodegradable metallic biomaterials. Acta Biomater. 2008;4:284.
[43] Lango T, Morland T, Brubakk AO. Diffusion coefficients and solubility coefficients for gases in biological fluids and tissues: A review. Undersea Hyperb. Med. 1996;23:247.
[44] Vaupel P. Effect of percentual water-conent in tissues and liquids on diffusion-coefficients of O_2 CO_2, N_2, and H_2. Pflugers Arch. 1976;361:201.
[45] Li ZJ, Gu XN, Lou SQ, Zheng YF. The development of binary Mg-Ca alloys for use as biodegradable materials within bone. Biomaterials 2008;29:1329.
[46] Xu LP, Yu GN, Zhang E, Pan F, Yang K. In vivo corrosion behavior of Mg-Mn-Zn alloy for bone implant application. J. Biomed. Mater. Res. 2007;83A:703.
[47] Xin YC, Huo KF, Hu T, Tang GY, Chu PK. Corrosion products on biomedical magnesium alloy soaked in simulated body fluids. J. Mater. Res. 2009;24:2711.
[48] Rettig R, Virtanen S. Composition of corrosion layers on a magnesium rare-earth alloy in simulated body fluids. J. Biomed. Mater. Res. 2009;88A:359.
[49] Xu LP, Zhang EL, Yin DS, Zeng SY, Yang K. In vitro corrosion behaviour of Mg alloys in a phosphate buffered solution for bone implant application. J. Mater. Sci.-Mater. Med. 2008;19:1017.
[50] Lorenz C, Brunner JG, Kollmannsberger P, Jaafar L, Fabry B, Virtanen S. Effect of surface pre-treatments on biocompatibility of magnesium. Acta Biomater. 2009;5:2783.
[51] ISO 10993-5 (2009), Biological evaluation of medical devices - Part 5: Tests for in vitro cytotoxicity, International Organization for Standardization.
[52] Christoph K, Beck F-X, Neuhofer W. Osmoadaptation of Mammalian cells - an orchestrated network of protective genes. Current genomics 2007;8:209.
[53] Fischer J, Prosenc MH, Wolff M, Hort N, Willumeit R, Feyerabend F. Interference of magnesium corrosion with tetrazolium-based cytotoxicity assays. Acta Biomater. 2010;6:1813.
[54] Zhang SX, Zhang XN, Zhao CL, Li JA, Song Y, Xie CY, Tao HR, Zhang Y, He YH, Jiang Y, Bian YJ. Research on an Mg-Zn alloy as a degradable biomaterial. Acta Biomaterialia 2010;6:626.
[55] Zhang SX, Li JA, Song Y, Zhao CL, Zhang XN, Xie CY, Zhang Y, Tao HR, He YH, Jiang Y, Bian YJ. In vitro degradation, hemolysis and MC3T3-E1 cell adhesion of biodegradable Mg-Zn alloy. Materials Science & Engineering C-Materials for Biological Applications 2009;29:1907.
[56] Zhang E, Yin D, Xu L, Yang L, Yang K. Microstructure, mechanical and corrosion properties and biocompatibility of Mg-Zn-Mn alloys for biomedical application. Mater. Sci. Eng. C 2009;29:987.
[57] Zhang E, Yang L, Xu J, Chen H. Microstructure, mechanical properties and bio-corrosion properties of Mg-Si(-Ca, Zn) alloy for biomedical application. Acta

Biomater. 2010;6:1756.
[58] Zhang E, Yang L. Microstructure, mechanical properties and bio-corrosion properties of Mg-Zn-Mn-Ca alloy for biomedical application. Mater. Sci. Eng. A 2008;497:111.
[59] Xu L, Pan F, Yu G, Yang L, Zhang E, Yang K. In vitro and in vivo evaluation of the surface bioactivity of a calcium phosphate coated magnesium alloy. Biomaterials 2009;30:1512.
[60] Witte F, Fischer J, Nellesen J, Vogt C, Vogt J, Donath T, Beckmann F. In vivo corrosion and corrosion protection of magnesium alloy LAE442. Acta Biomater. 2010;6:1792.
[61] Tahan JE, Granadillo VA, Romero RA.
Electrothermal atomic absorption spectrometric determination of Al, Cu, Fe, Pb, V and Zn in clinical samples and in certified environmental reference materials. Anal. Chim. Acta 1994;295:187.
[62] Ferreira PC, Piai KD, Takayanagui AMM, Segura-Munoz SI. Aluminum asa risk factor for Alzheimer's disease. Rev. Latino-Am. Enfermagem 2008;16:151.
[63] Shingde M, Hughes J, Boadle R, Wills EJ, Pamphlett R. Macrophagic myofasciitis associated with vaccine-derived aluminium. Med. J. Aust. 2005;183:145.
[64] Rousselle AV, Heymann D, Demais V, Charrier C, Passuti N, Basle MF. Influence of metal ion solutions on rabbit osteoclast activities in vitro. Histol. Histopath. 2002;17:1025.
[65] Witte F, Ulrich H, Rudert M, Willbold E. Biodegradable magnesium scaffolds: Part I: Appropriate inflammatory response. J. Biomed. Mater. Res. 2007;81A:748.
[66] Loos A, Rohde R, Haveich A, Barlach S. In vitro and in vivo biocompatibility testing of absorbable metal stents. Macromol. Symp. 2007;253:103.
[67] Boehlert CJ, Knittel K. The microstructure, tensile properties, and creep behavior of Mg-Zn alloys containing 0-4.4 wt.% Zn. Mater. Sci. Eng. A-Struct. Mater. Prop. Microstruct. Process. 2006;417:315.
[68] Yin DS, Zhang EL, Zeng SY. Effect of Zn content on microstructure, mechanical properties and fracture behavior of Mg-Mn alloy. China Foundry 2009;6:43.
[69] Lee YC, Dahle AK, StJohn DH. The role of solute in grain refinement of magnesium. Metall. Mater. Trans. A-Phys. Metall. Mater. Sci. 2000;31:2895.
[70] Renkema KY, Alexander RT, Bindels RJ, Hoenderop JG. Calcium and phosphate homeostasis: Concerted interplay of new regulators. Ann. Med. 2008;40:82.
[71] Yamamoto A, Honma R, Sumita M. Cytotoxicity evaluation of 43 metal salts using murine fibroblasts and osteoblastic cells. Journal of Biomedical Materials Research 1998;39:331.
[72] Eisenbarth E, Velten D, Muller M, Thull R, Breme J. Biocompatibility of β-stabilizing elements of titanium alloys. Biomaterials 2004;25:5705.
[73] Matsuno H, Yokoyama A, Watari F, Uo M, Kawasaki T. Biocompatibility and osteogenesis of refractory metal implants, titanium, hafnium, niobium, tantalum and rhenium. Biomaterials 2001;22:1253.
[74] Geurtsen W. Biocompatibility of dental casting alloys. Critical Reviews in Oral Biology & Medicine 2002;13:71.
[75] Connelly N, Damhus T, Hartshorn R, Hutton A, editors. Nomenclature of Inorganic Chemistry: IUPAC Recommendations 2005.: Cambridge: RSC Publ., 2005.
[76] Peng Q, Huang Y, Zhou L, Hort N, Kainer KU. Preparation and properties of high purity Mg-Y biomaterials. Biomaterials 2010;31:398.
[77] Nakamura Y, Tsumura Y, Tonogai Y, Shibata T, Ito Y. Differences in behavior

among the chlorides of seven rare earth elements administered intravenously to rats. Fundam. Appl. Toxicol. 1997;37:106.
[78] Oberdisse E, Arvela P, Gross U. Lanthanon-induced hepatotoxicity and its prevention by pretreatment with the same lanthanon Arch. Toxicol. 1979;43:105.
[79] Jha AM, Singh AC. Clastogenicity of lanthanides: induction of chromosomal aberration in bone marrow cells of mice in vivo. Mutat. Res.-Genet. Toxicol. 1995;341:193.
[80] Palmer RJ, Butenhoff JL, Stevens JB. Cytotoxicity of the rare earth metals cerium, lanthanum, and neodymium in vitro: Comparisons with cadmium in a pulmonary macrophage primary culture system. Environ. Res. 1987;43:142.
[81] Haley TJ, Komesu N, Colvin G, Koste L, Upham HC. Pharmacology and toxicology of europium cloride J. Pharm. Sci. 1965;54:643.
[82] Poole RA, Bobba G, Cann MJ, Frias JC, Parker D, Peacock RD. Synthesis and characterisation of highly emissive and kinetically stable lanthanide complexes suitable for usage 'in cellulo'. Org. Biomol. Chem. 2005;3:1013.
[83] Doat A, Fanjul M, Pelle F, Hollande E, Lebugle A. Europium-doped bioapatite: a new photostable biological probe, internalizable by human cells. Biomaterials 2003;24:3365.
[84] Alpturk O, Rusin O, Fakayode SO, Wang WH, Escobedo JO, Warner IM, Crowe WE, Kral V, Pruet JM, Strongin RM. Lanthanide complexes as fluorescent indicators for neutral sugars and cancer biomarkers. Proc. Natl. Acad. Sci. U. S. A. 2006;103:9756.
[85] Haley TJ, Upham HC, Raymond K, Komesu N. Toxicological and pharmacological effects of gadolinium and samarium chlorides. British Journal of Pharmacology and Chemotherapy 1961;17:526.
[86] Feyerabend F, Siemers C, Willumeit R, Rosler J. Cytocompatibility of a free machining titanium alloy containing lanthanum. J. Biomed. Mater. Res. 2009;90A:931.
[87] Mooren FC, Golf SW, Lechtermann A, Volker K. Alterations of ionized Mg2+ in human blood after exercise. Life Sci. 2005;77:1211.
[88] Hirano S, Suzuki KT. Exposure, metabolism, and toxicity of rare earths and related compounds. Environ. Health Perspect. 1996;104:85.
[89] Yang WD, Zhang P, Liu JS, Xue YF. Effect of long-term intake of Y3+ in drinking water on gene expression in brains of rats. J. Rare Earths 2006;24:369.
[90] Haley TJ, Koste L, Komesu N, Efros M, Upham HC. Pharmacology and toxicology of dysprosium, holmium, and erbium chlorides. Toxicol. Appl. Pharmacol. 1966;8:37.
[91] Fuma S, Takeda H, Takaku Y, Hisamatsu S, Kawabata Z. Effects of dysprosium on the species-defined microbial microcosm. Bull. Environ. Contam. Toxicol. 2005;74:263.
[92] Bottrill M, Nicholas LK, Long NJ. Lanthanides in magnetic resonance imaging. Chem. Soc. Rev. 2006;35:557.
[93] Pourbaix M. Atlas of Electrochemical Equilibria in Aqueous Solutions. 1st English ed. (Oxford, New York: Pergamon Press, 1966).
[94] Beyersmann D. Effects of carcinogenic metals on gene expression. Toxicol. Lett. 2002;127:63.
[95] Bozym RA, Chimienti F, Giblin LJ, Gross GW, Korichneva I, Li YA, Libert S, Maret W, Parviz M, Frederickson CJ, Thompson RB. Free zinc ions outside a narrow concentration range are toxic to a variety of cells in vitro. Exp. Biol. Med. 2010;235:741.
[96] Kumar V, Gill KD. Aluminium neurotoxicity: neurobehavioural and oxidative aspects. Arch. Toxicol. 2009;83:965.

[97] Thyssen JP, Menne T. Metal Allergy-A Review on Exposures, Penetration, Genetics, Prevalence, and Clinical Implications. Chem. Res. Toxicol. 2010;23:309.

[98] Wen ZH, Wu CJ, Dai CS, Yang FX. Corrosion behaviors of Mg and its alloys with different Al contents in a modified simulated body fluid. Journal of Alloys and Compounds 2009;488:392.

[99] Erdmann N, Angrisani N, Reifenrath J, Lucas A, Thorey F, Bormann D, Meyer-Lindenberg A. Biomechanical testing and degradation analysis of MgCa0.8 alloy screws: A comparative in vivo study in rabbits. Acta Biomater.;7:1421.

[100] Krause A, von der Hoh N, Bormann D, Krause C, Bach FW, Windhagen H, Meyer-Lindenberg A. Degradation behaviour and mechanical properties of magnesium implants in rabbit tibiae. J. Mater. Sci. 2010;45:624.

[101] Zhang S, Zhang X, Zhao C, Li J, Song Y, Xie C, Tao H, Zhang Y, He Y, Jiang Y, Bian Y. Research on an Mg-Zn alloy as a degradable biomaterial. Acta Biomater. 2010;6:626.

[102] Zhang E, Xu L, Yu G, Pan F, Yang K. In vivo evaluation of biodegradable magnesium alloy bone implant in the first 6 months implantation. J. Biomed. Mater. Res. 2009;90A:882.

[103] Heublein B, Rohde R, Kaese V, Niemeyer M, Hartung W, Haverich A. Biocorrosion of magnesium alloys: a new principle in cardiovascular implant technology? Heart 2003;89:651.

[104] Peeters P, Bosiers M, Verbist J, Deloose K, Heublein B. Preliminary results after application of absorbable metal stents in patients with critical limb ischemia. Journal of Endovascular Therapy 2005;12:1.

[105] Rokhlin LL. Magnesium Alloys Containing Rare Earth Metals. Moscow: Taylor & Francis, 2003.

[106] Peng Q, Hou X, Wang L, Wu Y, Cao Z, Wang L. Microstructure and mechanical properties of high performance Mg–Gd based alloys. Mater. Des. 2009;30:292.

[107] Wang J, Meng J, Zhang D, Tang D. Effect of Y for enhanced age hardening response and mechanical properties of Mg–Gd–Y–Zr alloys. Mater. Sci. Eng. A 2007;456:78.

[108] He SM, Zeng XQ, Peng LM, Gao X, Nie JF, Ding WJ. Microstructure and strengthening mechanism of high strength Mg–10Gd–2Y–0.5Zr alloy. Journal of Alloys and Compounds 2007;427:316.

[109] Peng LM, Chang JW, Guo XW, Atrens A, Ding WJ, Peng YH. Influence of heat treatment and microstructure on the corrosion of magnesium alloy Mg-10Gd-3Y-0.4Zr. Journal of Applied Electrochemistry 2009;39:913.

[110] Liang S, Guan D, Tan X. The relation between heat treatment and corrosion behavior of Mg-Gd-Y-Zr alloy. Mater. Des. 2011;32:1194.

[111] Nayeb-Hashemi AA, Clark JB. Phase Diagram of Binary Magnesium Alloys. Metal Park, OH, USA: ASM International, 1988.

[112] Apps PJ, Karimzadeh H, King JF, Lorimer GW. Precipitation reactions in magnesium-rare earth alloys containing Yttrium, Gadolinium or Dysprosium. Scripta Materialia 2003;48:1023.

[113] Xin YC, Liu CL, Zhang XM, Tang GY, Tian XB, Chu PK. Corrosion behavior of biomedical AZ91 magnesium alloy in simulated body fluids. J. Mater. Res. 2007;22:2004.

[114] Heinrich MC, Kuhlmann MK, Kohlbacher S, Scheer M, Grgic A, Heckmann MB, Uder M. Cytotoxicity of iodinated and gadolinium-based contrast agents in renal tubular cells at angiographic concentrations: In vitro study. Radiology 2007;242:425.

[115] Vostry P, Smola B, Stulikova I, von Buch F, Mordike BL. Microstructure

evolution in isochronally heat treated Mg-Gd alloys. Physica Status Solidi a-Applied Research 1999;175:491.

[116] Honma T, Ohkubo T, Hono K, Kamado S. Chemistry of nanoscale precipitates in Mg-2.1Gd-0.6Y-0.2Zr (at.%) alloy investigated by the atom probe technique. Mater. Sci. Eng. A 2005;395:301.

[117] Gallagher JA. Human osteoblast culture. Methods in molecular medicine 2003;80:3.

[118] Nie JF, Muddle BC. Characterisation of strengthening precipitate phases in a Mg-Y-Nd alloy. Acta Materialia 2000;48:1691.

[119] Xu Y, Chumbley LS, Weigelt GA, Laabs FC. Analysis of interdiffusion of Dy, Nd, and Pr in Mg. J. Mater. Res. 2001;16:3287.

[120] Gao X, He SM, Zeng XQ, Peng LM, Ding WJ, Nie JF. Microstructure evolution in a Mg-15Gd-0.5Zr (wt.%) alloy during isothermal aging at 250°C. Mater. Sci. Eng. A 2006;431:322.

[121] He SM, Zeng XQ, Peng LM, Gao X, Nie JF, Ding WJ. Precipitation in a Mg-10Gd-3Y-0.4Zr (wt.%) alloy during isothermal ageing at 250°C. Journal of Alloys and Compounds 2006;421:309.

[122] Nie JF. Effects of precipitate shape and orientation on dispersion strengthening in magnesium alloys. Scripta Materialia 2003;48:1009.

[123] Rosalbino F, Angelini E, De Negri S, Saccone A, Delfino S. Electrochemical behaviour assessment of novel Mg-rich Mg-Al-RE alloys (RE=Ce, Er). Intermetallics 2006;14:1487.

[124] Song YL, Liu YH, Wang SH, Yu SR, Zhu XY. Effect of cerium addition on microstructure and corrosion resistance of die cast AZ91 magnesium alloy. Materials and Corrosion 2007;58:189.

[125] Song G, Atrens A, Dargusch M. Influence of microstructure on the corrosion of diecast AZ91D. Corros. Sci. 1998;41:249.

[126] Liu M, Schmutz P, Uggowitzer PJ, Song G, Atrens A. The influence of yttrium (Y) on the corrosion of Mg-Y binary alloys. Corros. Sci. 2010;52:3687.

[127] Song Y, Shan D, Chen R, Han E-H. Corrosion characterization of Mg-8Li alloy in NaCl solution. Corros. Sci. 2009;51:1087.

[128] Izumi S, Yamasaki M, Kawamura Y. Relation between corrosion behavior and microstructure of Mg-Zn-Y alloys prepared by rapid solidification at various cooling rates. Corros. Sci. 2009;51:395.

[129] Hara N, Kobayashi Y, Kagaya D, Akao N. Formation and breakdown of surface films on magnesium and its alloys in aqueous solutions. Corros. Sci. 2007;49:166.

[130] Chang J-W, Guo X-W, Fu P-H, Peng L-M, Ding W-J. Effect of heat treatment on corrosion and electrochemical behaviour of Mg-3Nd-0.2Zn-0.4Zr (wt.%) alloy. Electrochimica Acta 2007;52:3160.

[131] Zhang X, Yuan G, Mao L, Niu J, Fu P, Ding W. Effects of extrusion and heat treatment on the mechanical properties and biocorrosion behaviors of a Mg–Nd–Zn–Zr alloy. Journal of the Mechanical Behavior of Biomedical Materials 2012;7:77.

[132] Mueller W-D, Fernandez Lorenzo de Mele M, Nascimento ML, Zeddies M. Degradation of magnesium and its alloys: Dependence on the composition of the synthetic biological media. J. Biomed. Mater. Res. 2009;90A:487.

[133] Zainal Abidin NI, Martin D, Atrens A. Corrosion of high purity Mg, AZ91, ZE41 and Mg2Zn0.2Mn in Hank's solution at room temperature. Corros. Sci. 2011;53:862.

[134] Dean JA, editor Lange's Handbook of Chemistry: GcGraw-Hill, 1999.

[135] Song Y, Liu Y, Yu S, Zhu X, Wang S. Effect of neodymium on microstructure and corrosion resistance of AZ91 magnesium alloy. J. Mater. Sci. 2007;42:4435.

[136] Ardelean H, Marcus P, Fiaud C. Enhanced corrosion resistance of magnesium

and its alloys through the formation of cerium (and aluminium) oxide surface films. Materials and Corrosion 2001;52:889.

[137] Kuwahara H, Al-Abdullat Y, Mazaki N, Tsutsumi S, Aizawa T. Precipitation of magnesium apatite on pure magnesium surface during immersing in Hank's solution. Materials Transactions 2001;42:1317.

[138] Gu XN, Xie XH, Li N, Zheng YF, Qin L. In vitro and in vivo studies on a Mg-Sr binary alloy system developed as a new kind of biodegradable metal. Acta Biomater. 2012;8:2360.

[139] Huehnerschulte TA, Angrisani N, Rittershaus D, Bormann D, Windhagen H, Meyer-Lindenberg A. In Vivo Corrosion of Two Novel Magnesium Alloys ZEK100 and AX30 and Their Mechanical Suitability as Biodegradable Implants. Materials 2011;4:1144.

[140] Das GK, Zhang Y, D'Silva L, Padmanabhan P, Heng BC, Loo JSC, Selvan ST, Bhakoo KK, Tan TTY. Single-Phase Dy2O3:Tb3+ Nanocrystals as Dual-Modal Contrast Agent for High Field Magnetic Resonance and Optical Imaging. Chemistry of Materials;23:2439.

[141] Drynda A, Deinet N, Braun N, Peuster M. Rare earth metals used in biodegradable magnesium-based stents do not interfere with proliferation of smooth muscle cells but do induce the upregulation of inflammatory genes. J. Biomed. Mater. Res. 2009;91A:360.

[142] McLaren A, Hetherington E, Maddalena D, Snowdon G. Dysprosium (Dy-165) Hydroxide Macroaggregates for Radiation Synovectomy - Animal Studies. European Journal of Nuclear Medicine 1990;16:627.

[143] Edmonds J, Smart R, Laurent R, Butler P, Brooks P, Hoschl R, Wiseman J, George S, Lovegrove F, Warwick A. A comparative study of the safety and efficacy of dysprosium-165 hydroxide macro-aggregate and yttrium-90 silicate colloid in radiation synovectomy--a multicentre double blind clinical trial. Australian Dysprosium Trial Group. Brit. J. Rheumatol. 1994;33:947.

[144] Zaichick S, Zaichick V, Karandashev V, Nosenko S. Accumulation of rare earth elements in human bone within the lifespan. Metallomics 2011;3:186.

[145] Getman EI, Loboda SN, Tkachenko TV, Ignatov AV, Zabirko TF. Substitution of calcium with neodymium and dysprosium in hydroxyapatite structure. Functional Materials 2005;12:6.

[146] Apps PJ, Karimzadeh H, King JF, Lorimer GW. Phase compositions in magnesium-rare earth alloys containing yttrium, gadolinium or dysprosium. Scripta Materialia 2003;48:475.

[147] Wu Y, Hu W. Comparison of the Solid Solution Properties of Mg-RE (Gd, Dy, Y) Alloys with Atomistic Simulation
10.1155/2008/476812. Research Letters in Physics 2008;2008.

[148] Guo X-W, Chang J-W, He S-M, Ding W-J, Wang X. Investigation of corrosion behaviors of Mg–6Gd–3Y–0.4Zr alloy in NaCl aqueous solutions. Electrochimica Acta 2007;52:2570.

[149] Kiryuu M, Okumura H, Kamado S, Kojima Y, Nnomiya R, Nakatsugawa I. corrosion restance of heat resistant magnesium alloys containing heavy rare earth elements. Japan Institute of Light Metal 1996;46:39.

[150] Bruce DW, Hietbrink BE, Dubois KP. ACUTE MAMMALIAN TOXICITY OF RARE EARTH NITRATES AND OXIDES. Toxicol. Appl. Pharmacol. 1963;5:750.

[151] Thomsen HS. Gadolinium-based contrast media may be nephrotoxic even at approved doses. Eur. Radiol. 2004;14:1654.

[152] Maiseyeu A, Mihai G, Kampfrath T, Simonetti OP, Sen CK, Roy S, Rajagopalan S, Parthasarathy S. Gadolinium-containing phosphatidylserine liposomes for

molecular imaging of atherosclerosis. Journal of Lipid Research 2009;50:2157.

[153] Petoral RM, Soderlind F, Klasson A, Suska A, Fortin MA, Abrikossova N, Selegard L, Kall PO, Engstrom M, Uvdal K. Synthesis and Characterization of Tb(3+)-Doped Gd(2)O(3) Nanocrystals: A Bifunctional Material with Combined Fluorescent Labeling and MRI Contrast Agent Properties. Journal of Physical Chemistry C 2009;113:6913.

[154] Na HB, Song IC, Hyeon T. Inorganic Nanoparticles for MRI Contrast Agents. Advanced Materials 2009;21:2133.

[155] Hemmer E, Kohl Y, Colquhoun V, Thielecke H, Soga K, Mathur S. Probing Cytotoxicity of Gadolinium Hydroxide Nanostructures. Journal of Physical Chemistry B 2010;114:4358.

[156] ten Dam M, Wetzels JFM. Toxicity of contrast media: an update. Netherlands Journal of Medicine 2008;66:416.

[157] Wedeking P, Kumar K, Tweedle MF. Dose-dependent biodistribution of [^{153}Gd]Gd(acetate)n in mice. Nuclear Medicine and Biology 1993;20:679.

[158] Song G, StJohn D. The effect of zirconium grain refinement on the corrosion behaviour of magnesium-rare earth alloy MEZ. Journal of Light Metals 2002;2:1.

[159] Sun M, Wu G, Wang W, Ding W. Effect of Zr on the microstructure, mechanical properties and corrosion resistance of Mg-10Gd-3Y magnesium alloy. Mater. Sci. Eng. A 2009;523:145.

[160] Aung NN, Zhou W. Effect of grain size and twins on corrosion behaviour of AZ31B magnesium alloy. Corros. Sci. 2010;52:589.

[161] Alvarez-Lopez M, Pereda MD, del Valle JA, Fernandez-Lorenzo M, Garcia-Alonso MC, Ruano OA, Escudero ML. Corrosion behaviour of AZ31 magnesium alloy with different grain sizes in simulated biological fluids. Acta BiomaterialiaThe THERMEC 2009 Biodegradable Metals 2010;6:1763.

[162] Hosford WF. Mechanical Behavior of Materials. New York: Cambridge University Press, 2005.

[163] Lukae P, Trojanova Z. Influence of Grain Size on Ductility of Magnesium Alloys. Materials Engineering 2011;18:110.

10 Appendix

Table 21: Detailed composition of DMEM.

	Component	**mg/L**
Inorganic salts	Calcium Chloride (CaCl2 · 2H2O)	264
	Ferric Nitrate (Fe(NO3)3 · 9H2O)	0.1
	Magnesium Sulfate (MgSO4 · 7H2O)	200
	Potassium Chloride (KCl)	400
	Sodium Bicarbonate (NaHCO3)	3700
	Sodium Chloride (NaCl)	6400
	Sodium Phosphate monobasic(NaH2PO4 · 2H2O)	141
vitamins	Choline chloride	4
	Thiamine hydrochloride	4
	Riboflavin	0.4
	Pyridoxine hydrochloride	4
	Niacinamide	4
	i-Inositol	7.2
	Folic acid	4
	D-Calcium pantothenate	4
Amino acids	Glycine	30
	L-Alanyl-L-glutamine	862
	L-Arginine hydrochloride	84
	L-Cystine 2HCl	63
	L-Histidine hydrochloride-H2O	42
	L-Isoleucine	105
	L-Leucine	105
	L-Lysine hydrochloride	146
	L-Methionine	30
	L-Phenylalanine	66
	L-Serine	42
	L-Threonine	95
	L-Tryptophan	16
	L-Tyrosine	72
	L-Valine	94
Other components	D-Glucose (Dextrose)	4500
	Phenol Red	15
	Sodium Pyruvate	110

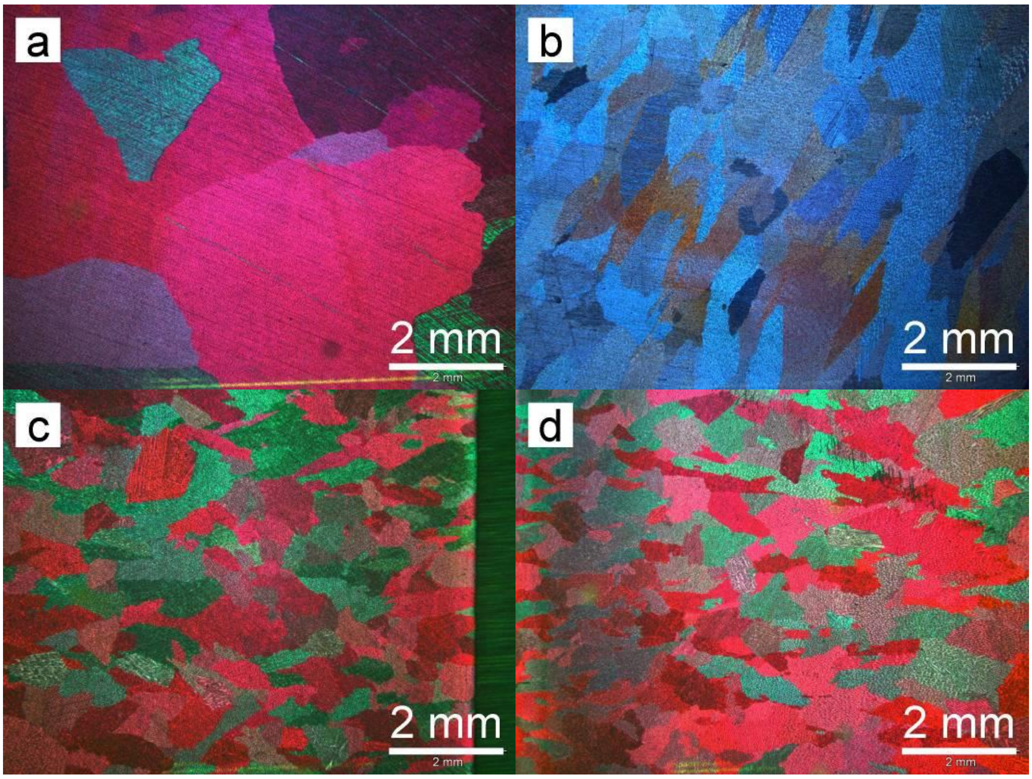

Fig. 83: Optical microstructure of as-cast Mg-Dy alloys at low magnification: (a) Mg-5Dy; (b) Mg-10Dy; (c) Mg-15Dy; (d) Mg-20Dy.

Fig. 84: Macro corrosion morphology of as-cast Mg-Dy alloys after immersion in CCM under cell culture conditions for 3 days and 14 days.

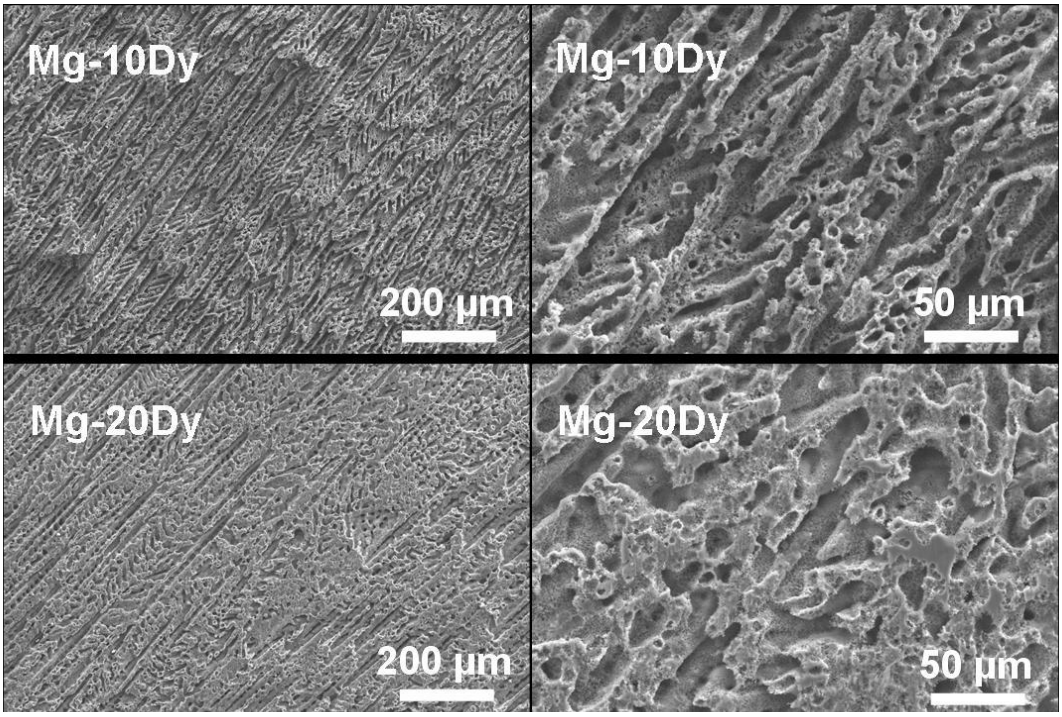

Fig. 85: Corrosion morphology of as-cast Mg-Dy alloys after immersion in CCM under cell culture conditions for 14 days and removal of corrosion products.

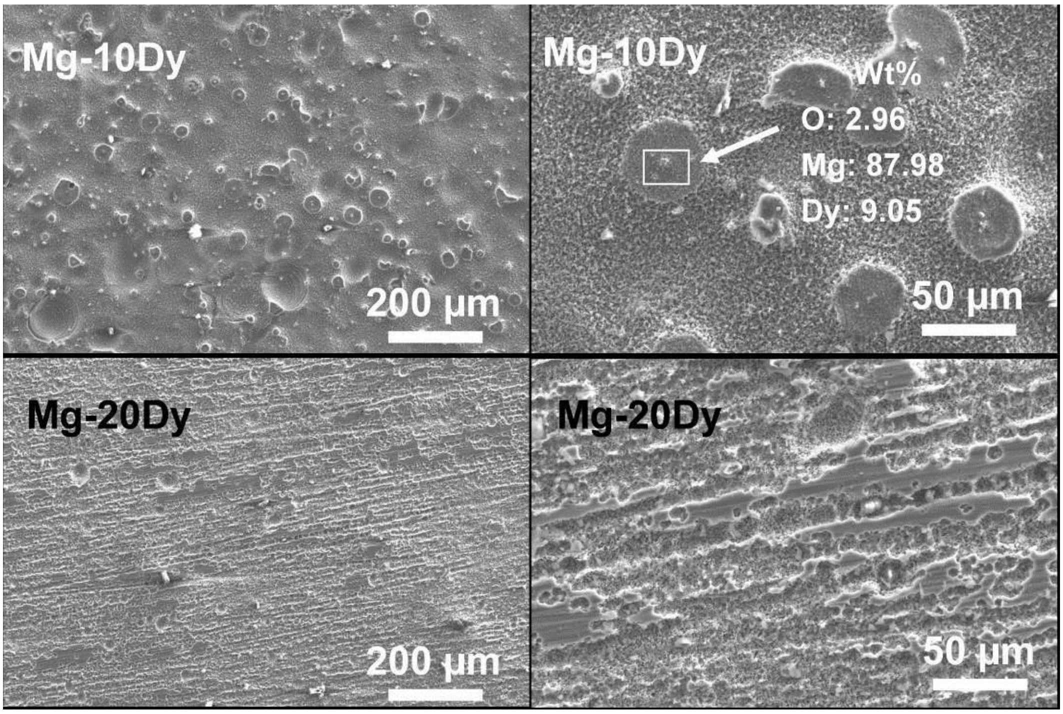

Fig. 86: Corrosion morphology of solution heat treated Mg-Dy alloys after immersion in CCM under cell culture conditions for 14 days and removal of corrosion products.

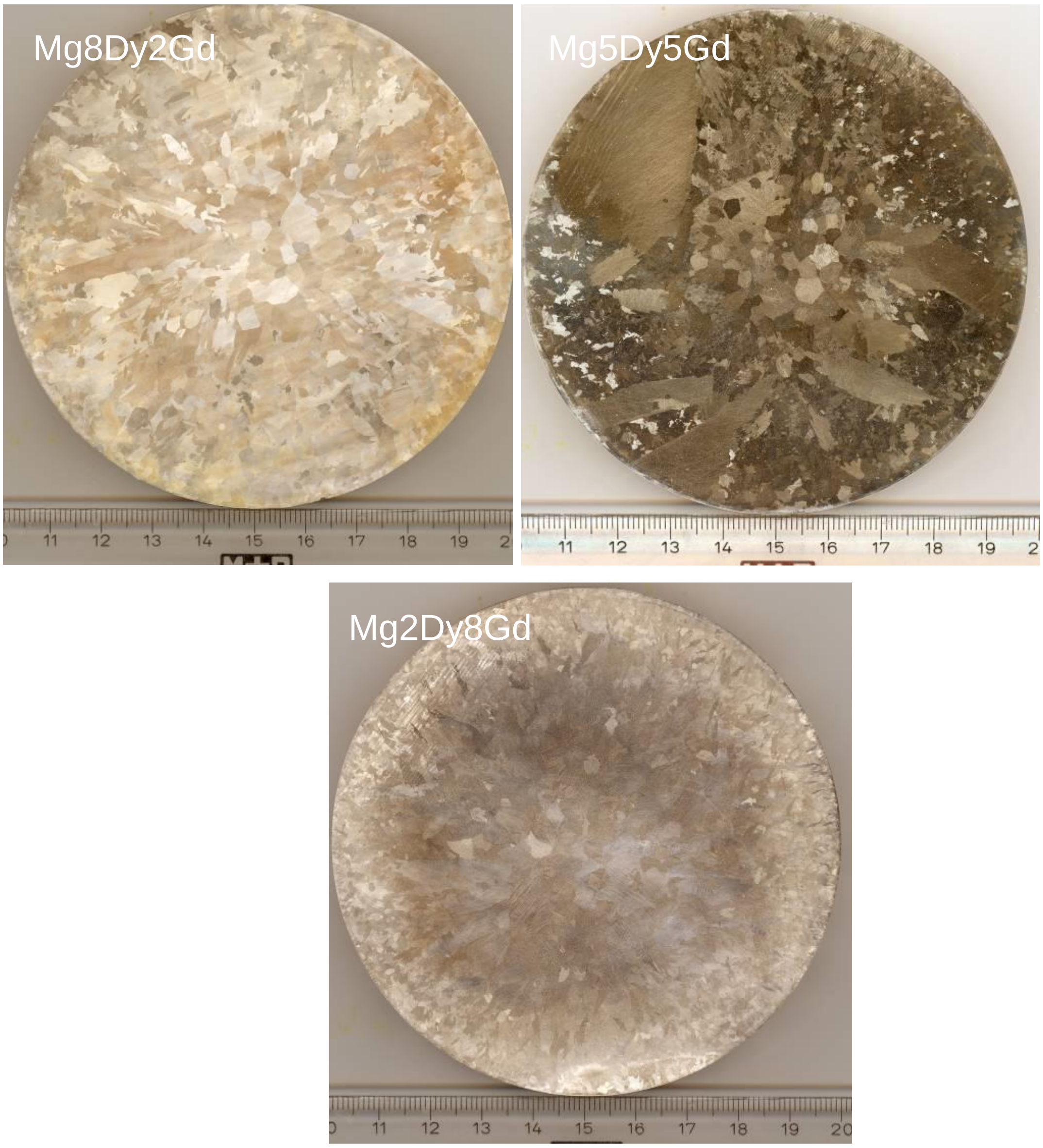

Fig. 87: Macrostructure of Mg-Dy-Gd alloys without the addition of Zr (horizontal direction).

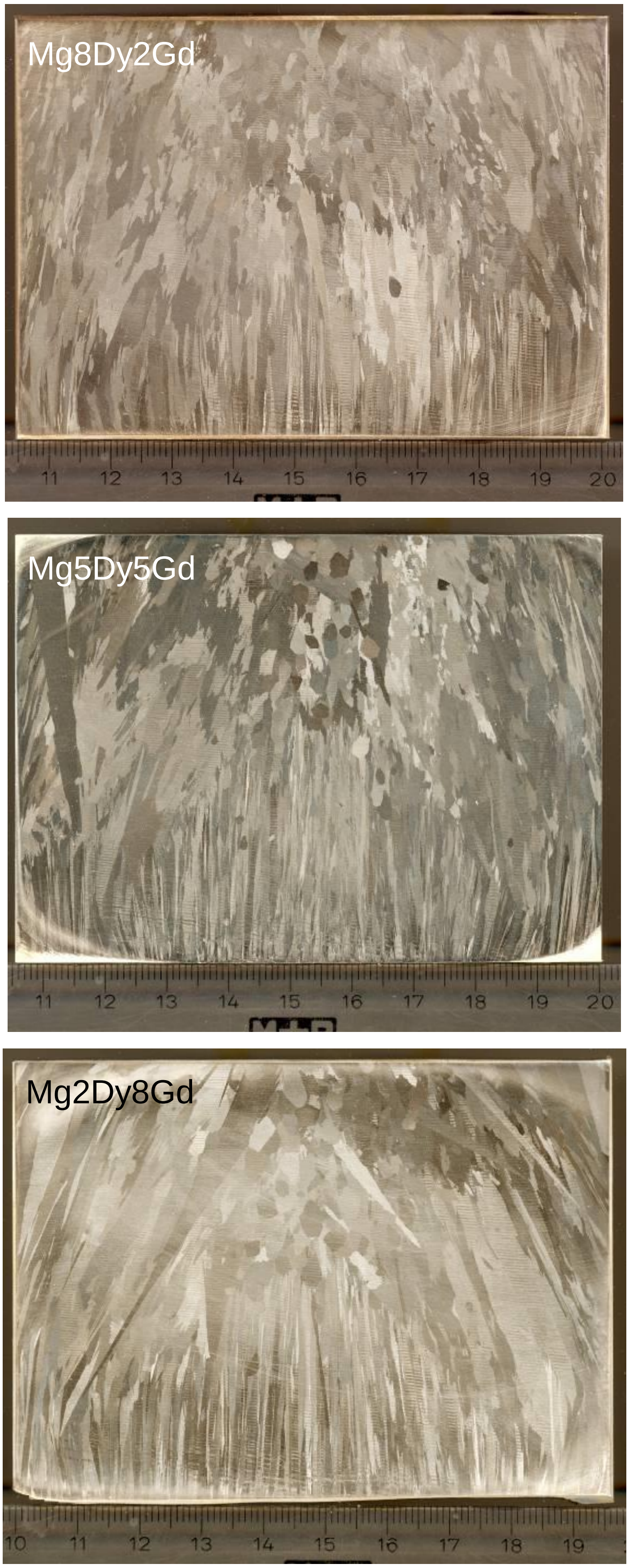

Fig. 88: Macrostructure of Mg-Dy-Gd alloys without the addition of Zr (vertical direction).

11 Publication list

Journal papers

1. ***Yang L***, Huang Y, Peng Q, Feyerabend F, Kainer KU, Willumeit R, Hort N. Mechanical and corrosion properties of binary Mg–Dy alloys for medical applications. Materials Science and Engineering: B 2011;176:1827-34.
2. Gan W, Huang Y, ***Yang L***, Kainer KU, Jiang M, Brokmeier H, Hort N. Identification of unexpected hydrides in Mg-20 wt% Dy alloy by high-brilliance synchrotron radiation. Journal of Applied Crystallography 2011; 1: 17-21.
3. ***Yang L***, Huang Y, Feyerabend F, Willumeit R, Kainer KU, Hort N, Influence of Ageing Treatment on Microstructure, Mechanical and Bio-corrosion Properties of Mg-Dy alloys, Journal of the Mechanical Behavior of Biomedical Materials, 2012; 3; 36-44.
4. ***Yang L***, Hort N, Willumeit R, Feyerabend F, Effects of corrosion environment and proteins on magnesium corrosion, Corrosion Engineering, Science and Technology, 2012; 5; 335-39.
5. ***Yang L***, Hort N, Laipple D, Höche D, Huang Y, Kainer KU, Willumeit R,Feyerabend F. Microstructrue and Cytotoxicity of Corrosion Layer on the Surface of Mg-10Dy Alloy. Acta. Biomater. doi: http://dx.doi.org/10.1016/j.bbr.2011.03.031

Conference contributions

1. ***Yang L***, Feyerabend F, Willumeit R, Kainer KU, Hort N, Corrosion behavior of As-cast Binary Mg-Dy Alloys, Light Metal Technology 2011_Poster

2. ***Yang L***, Huang Y, Feyerabend F, Willumeit R, Kainer KU, Hort N, Development of Mg-Dy-Gd-Zr alloys for medical applications, Junior Euromat. 2012_Oral poster

3. ***Yang L***, Feyerabend F, Blawert C, Regine Willumeit, Huang Y, Kainer KU, Hort N, Influences of Dy on the bio-corrosion behavior of binary Mg-Dy alloys in cell culture medium, 4th Symposium on Biodegradable Metals 2012_Oral presentation

Curriculum vitae

Personal information

First name: Lei

Last name: Yang

Gender: male

Date of birth: 22. 05. 1984

Email: lyang0522@gmail.com

Education

2009 - 2013	Doctoral Candidate at Institute of Metallurgy, Clausthal University of Technology, Germany
2006 - 2009	Master Degree at Institute of Metal Research Chinese Academy of Science (IMR, CAS)
2002 - 2006	Bachelor Degree at College of Material Science and Engineering, Harbin Engineering University

Professional experience

2009-2013	Research assistant at Magnesium Innovation Centre, Helmholtz-Zentrum Geesthacht (HZG), Germany

Signature:

Date: